INTER-RELATIONSHIP BETWEEN LITHOLOGY AND STRUCTURE AND ITS CONTROL ON GOLD MINERALIZATION IN BUHWEJU AREA, SW OF UGANDA

ENGDAWORK ADMASSU BAHIRU
FEB21, 2011

SUPERVISORS:
Dr. T. Woldai
Drs. B. J. de Smeth

Inter-Relationship between Lithology and Structure and its Control on Gold Mineralization in Buhweju area, SW OF UGANDA

ENGDAWORK ADMASSU BAHIRU
Enschede, The Netherlands, February 21, 2011

Thesis submitted to the Faculty of Geo-Information Science and Earth Observation of the University of Twente in partial fulfilment of the requirements for the degree of Master of Science in Geo-information Science and Earth Observation.
Specialization: Applied Earth Sciences

SUPERVISORS:
Dr. T. Woldai
Drs. B.J.de Smeth

THESIS ASSESSMENT BOARD:
Prof. Dr. F. D. van der Meer
Dr. D.G. Rossiter

ABSTRACT

Poor accessibility, dense vegetation and lack of outcrops are detrimental to conventional field geological mapping. The Buhweju area is poorly explored area with high vegetation density and known to host alluvial gold. The challenge is to look the interrelationship between lithology and structure in Buhweju and to assess the control on gold mineralization in the area. A new geological map as well as the inter-relationship between lithology and structure of Buhweju was presented through individual and integrated interpretations of geophysical data, multispectral data and published geological map. Previous studies of both regional and local scales including the result of this study have generally revealed the complexity of structural and lithological evolution of the area.

Applied image processing and enhancement techniques substantially improved the various data sets of the Buhweju area for better visual interpretation. The amount of geological information that could be obtained from multispectral data analysis was greatly hindered by various factors including complex topographic setting, vegetation cover and less variability in reflectance of the different lithological units. The geophysical data has also proved to be a valuable tool to understand the geology of Buhweju. The gamma ray data has found to be an invaluable aid, which together with modern enhancement and integration techniques have assisted in the visualization and discrimination of lithological units of the area. The interpretations made on the aeromagnetic data have depicted worthful information regarding lithomagnetic domains and tectonics of Buhweju.

The structural orientation analysis has revealed three dominant lineament orientations which determine the tectonic grain of the area, NNW-SSE, ESE-WNW and NNE-SSW. These orientations were found consistent with the regional tectonics. Non-orientation density analysis applied on the individual surface and subsurface lineaments has indicated that the Buhweju group rocks and undifferentiated between schist and amphibolites were affected by high lineament concentration.

The control of Buhweju gold field was assessed in terms of the improved geological units and interpreted lineaments of the area. Accordingly, no spatial association was observed between most of the gold occurrences and Buhweju sediments of pelitic and psammitic bands. On the other hand, most of the gold occurrences were found variably in Lubare quartzite, schist and gneissic units. The prominent NNE trending fault, identified from the aeromagnetic data has apparently controlled the distribution of gold occurrence of the area. Furthermore, most of the gold occurrences of Buhweju have showed an intimate association with interpreted high magnetic zones and quartz veins of the area. It was also evident that lithological units affected by high lineament density have hosted some of the gold occurrences in Buhweju.

ACKNOWLEDGEMENTS

I would like to thank my advisors Dr. T. Woldai and Drs. B. J. De Smeth for constructive advises and effort they have made for fulfilment of this research. Special thanks go to Dr. Frank van Ruitenbeek, Dr. John Carranza and Mr. Chris Hecker for their help to make me familiar with new techniques of mineral exploration. I would like to thank Dr. Nigel Stack and Dr. Sally Barritt for they gave me permission to use high resolution geophysical imagery for this research. Warmest thanks to local people around Buhweju for their undesirable help during field work.

TABLE OF CONTENTS

LIST OF FIGURES

LIST OF TABLES

1. INTRODUCTION

1.1. Research background

Geological maps with their subsequent derivative are considered to be the most reliable geosciences information having immense economic and societal value. A geological map provides information not only about the distribution and thickness of individual rock units but also reveals relationship among strata and structures which provide insight to many aspect example mineral potential. Acquiring geological information has nowadays greatly assisted by remote sensing technology as lots of works have already been documented.

Analysis and integration of multi disciplinary geoscientific information is becoming an advanced technique to ameliorate the geosciences knowledge. The problems in traditional geological mapping like limited exposed outcrop, extensive regolith and vegetation cover and subtle changes in geological features caused mapping largely based on geological inference. In integrated approach however, the information in each data set is analyzed separately and finally integrated to resolve the uncertainties and geological inferences. In integrated geological mapping the individual data layer is brought with different spectral and spatial resolutions that enable to extract more information and even to map subtle variations in geological feature, when integrated they are particularly useful.

The deeply dissected mountainous ridges in the east and the western rift valley are typical topographic features characterizing the study area, Buhweju. The geology of the area is presumed to be complex which undergone through different sequences of geological events accompanied by folding, refolding, recrystalization and metasomatism. The area is covered by various lithological units ranging from Precambrian metamorphic complex which have been extensively weathered and eroded to Pleistocene rift filling unconsolidated sediments and volcanics.

Buhweju is one of the gold and base metal producing areas in the country. Various compilation works on the mineral resources of Uganda showed wide spread alluvial gold in Buhweju and its surroundings. Three sulphide veins have also been identified at Kitaka, Kampono and Kanyambogo lead-zinc mines emplaced in shcists and gneiss. In these mines coarse crystalline gold also occur in vughs lined by quartz crystals. The aim of this research is therefore to see the relationship between lithology and structure of the area and to assess control on mineralization

Analyzing, interpreting and compiling the information contained in various data sets can result in producing necessary information related to lithological map, structural map and various thematic information before and after ground truthing. The geographic information system (GIS) has played major role in integrating and overlaying the various geosciences data and then producing maps which could be taken to the field to assist field mapping and ground truthing. Reliable geoscientific information in the form of geological map, structural map and mineral potential map could then be produced which are very vital for exploration and development of mineral resources.

1.2. Research problem

The study area, Buhweju, in the south west of Uganda is one of the prospective regions for gold and other base metal mineralization where presently gold is being extracted by artesian from alluvial deposit. The nature of gold and base metal mineralization and mineralized host rock in the area are unknown. The geotectonic, structural setting and ore mineralogy is compatible with an orogenic gold –type mineralization (Buchwaldt et al., 2008; Gabert, 1990; Groves et al., 1998; Link et al., 2010; Pohl, 1994; Rumvegeri, 1991; Tsige, 2006). The traditional geological map of the area was published in 1961 and recently the geological survey of Uganda has acquired various remote sensing data sets and has already started mapping the whole of Uganda including Buhweju. However, surface geological mapping could not be sufficient to explain the control and nature of mineralization of the area. Therefore, an account should be taken to further establish the relationship between lithology and structure of the low grade metamorphic terrain to assess the control on mineralization. The final goal is to characterize the relationship between structure and lithology which could decipher localization and control of mineralization of the area. These problems were addressed by applying different techniques including integration analysis of all the acquired remote sensing data, field mapping and known mineralization occurrence data.

1.3. Research Objective

The primary objective of the proposed research is to use various remotely sensed data and apply GIS techniques to establish the inter-relationship between lithology and structure and to assess its controls on known mineralized areas of Buhweju. Some of the specific objectives that will be addressed include:

- To produce improved geological and structural map of the Buhweju area
- To assess the inter-relationship between lithology and tectonic structure of the area
- To assess the control of lithology and structure on gold mineralization

1.4. Research Questions

The following research questions are addressed in this study:

- Can structural and lithological relationships assist in the identification of potential mineralization sites in low grade metamorphic terrains of Buhweju?
- Which remote sensing data discriminate more lithological units exposed in the area?
- What are the dominant structural settings of Buhweju?
- Does relationship exist between surface and subsurface structures/lineaments?

1.5. Research Hypothesis

- ➢ Association between lithology, structure and metamorphism will assist for identification of potential mineralization sites.
- ➢ Remote sensing data sets are important for geological mapping with varying ability in discriminating subtle differences of geologic features.
- ➢ Mineralization of an area can be controlled by lithology and structure

1.6. Overall research methodology

In order to reach objectives of the research and to answer the research questions several steps were carried out. The research was carried in three major phases:

1.6.1. Pre-field work

In the first instance literature review was carried out to extract the regional geology and mineralization of the study area. Other geological regions in Uganda were broadly explored since there is no much literature on only the Buhweju area. Projection of all the data sets used in the study to the same projection system was done during this phases of the research. During this time data preparation, preliminary pre-processing and interpretations of optical and airborne data were conducted to be taken to the field.

1.6.2. Field work

Field work was conducted to have ground truthing for some pre-processing and interpretations made in the above phase. The study area is topographically rugged and covered with protected forests for which access to majority of the area was difficult. However, traverses were designed to access as much areas as possible. During field work lithological descriptions and structural measurements were collected at about 140 observation points (Appendix 1). In addition various abandoned and active mine areas were surveyed GPS location and geological descriptions were taken.

1.6.3. Post-field work

The major tasks of the study including detail processing, analysis and interpretation were conducted during this phase of the research. Data sets were analysed and interpreted both in separate and integrated approaches to extract lithological contacts, lineaments and other geological features. Univariate and transformations (PCA) were applied on Landsat ETM and ASTER data then appropriate band combinations were chosen for lithological and structural interpretations. The SRTM DEM data was variously integrated with other data sets to increase geological interpretations of the area. Furthermore, processing and qualitative interpretations were applied on the gamma ray data for extraction of lithological information in terms of distribution of radioelement. This data was also integrated with optical and elevation data to increase interpretation. The underlying surface information was also achieved through qualitative interpretation applied on different aeromagnetic data layers. Finally, all the acquired lithological, structural and field collected data sets were integrated and digitized to produce the revised geology and structural maps of the area. Relationship between lithologies and structures was then established qualitatively and their control towards the prevailing mineralization was assessed. The general methodology followed in this research is shown in figure 1-1.

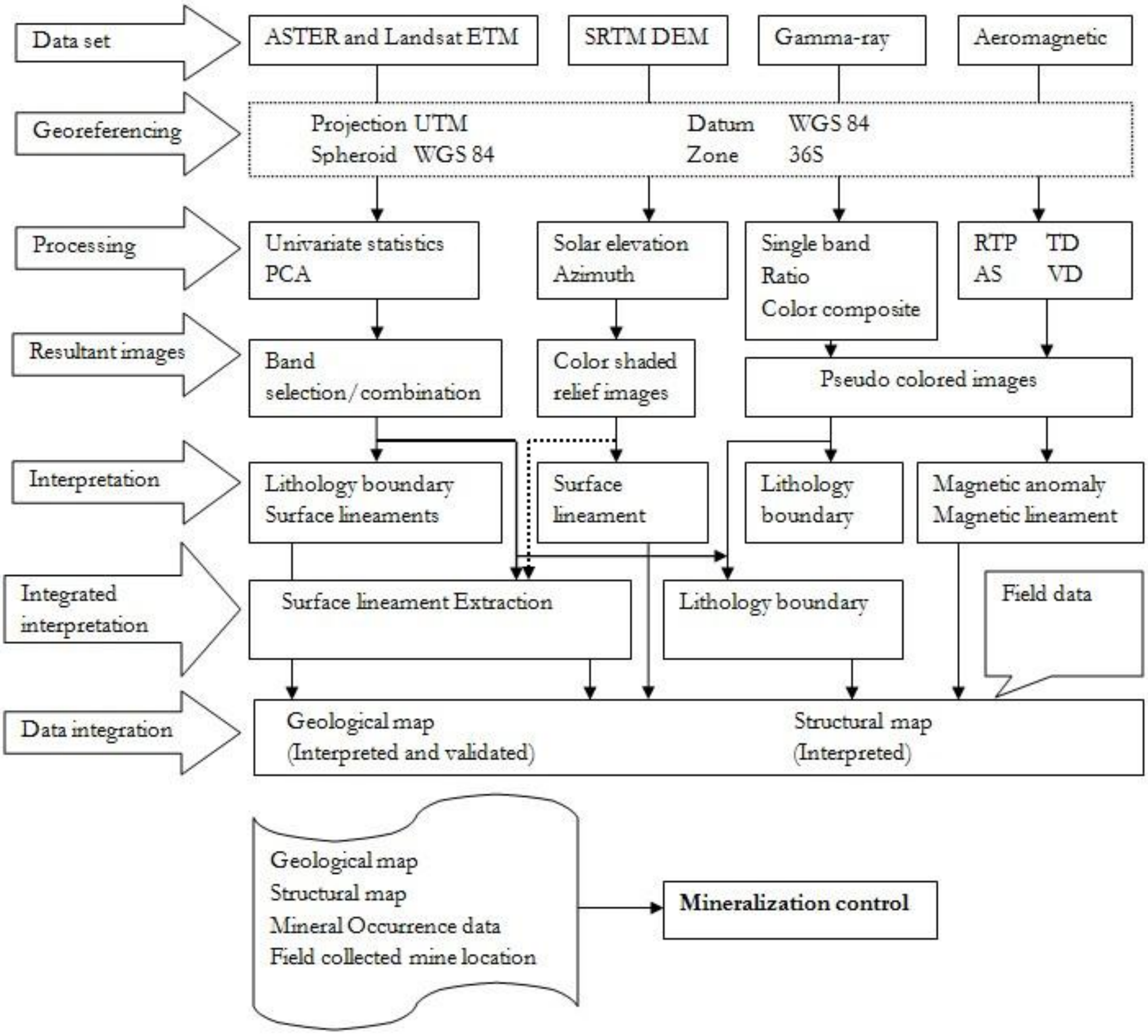

Figure 1-1: Flow chart of the research methodology

1.7. Available data sets

1.7.1. Airborne Magnetic and Radiometric data

The ministry of Energy and mineral development of the republic of Uganda has conducted airborne magnetic and radiometric surveys during survey date 07/12/06-31/05/07. The data was acquired and processed by Fugro airborne surveys. Survey flight lines with a spacing of 200m were flown in NE-SW direction and tie lines with a spacing of 2000m in NW-SE direction. The survey was conducted with mean terrain clearance of 80m and with a sample interval of 0.1s and 1s for magnetic and radiometric data respectively.

1.7.2. Multispectral data

The multispectral data sets of ASTER and Landsat ETM+ were used in this study. Radiometricaly calibrated and geometrically co-registered level 1B ASTER data with VNIR, SWIR and TIR bands was provided together with the multispectral Landsat ETM+ data having seven bands. The radiometric characteristics of ASTER and Landsat ETM data are given in (Table 1-1) below.

1.7.3. Other data sets

Elevation data of the area was provided both in gridded SRTM DEM format with a resolution of 33m and digital contour shape file format. Analog and digital geological map of the area was also provided and used in this study. In addition, field collected lithological, structural and mineral occurrence data were used in the study. All the above described data sets didn't cover the whole of the study area. The map in figure 1-2 shows the areal coverage of the data sets used in the study.

Region of Spectrum	Spatial Resolution	Spectral Range (µm)	ASTER Bands	Landsat Bands	Spectral Range (µm)	Spatial Resolution
VNIR				1	0.45-0.52	30 m
	15 m	0.52-0.60	1	2	0.52-0.60	
		0.63-0.69	2	3	0.63-0.69	
		0.76-0.86	3N (nadir looking)	4	0.76-0.90	
			3b (backward-look)	8	0.52-0.90	15 m
SWIR	30 m	1.60-1.70	4	5	1.55-1.75	30 m
		2.145-2.185	5	7	2.08-2.35	
		2.185-2.225	6			
		2.235-2.285	7			
		2.295-2.365	8			
		2.360-2.430	9			
TIR	90 m	8.125-8.475	10			
		8.475-8.825	11			
		8.925-9.275	12			
		10.25-10.95	13	6	10.40-12.50	60 m
		10.95-11.65	14			

Table 1-1: Radiometric characteristics of ASTER and Landsat ETM data

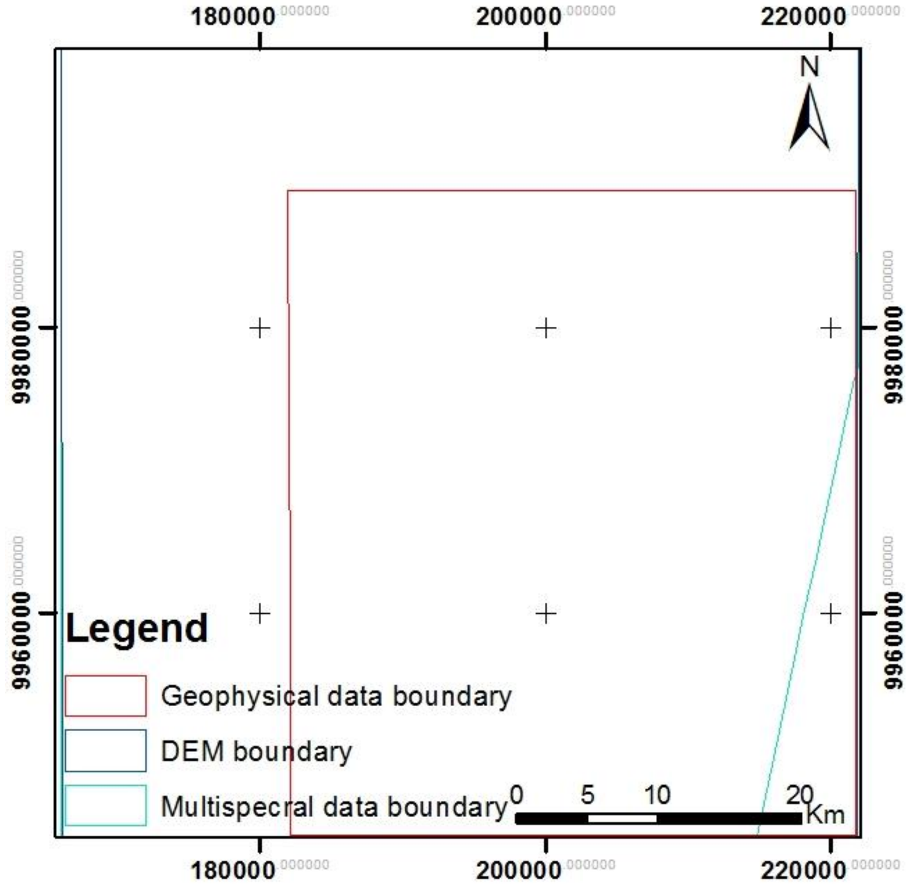

Figure 1-2: Display areas the different data sets used in this study.

1.8. Study Area

1.8.1. Location and Accessibility

The study area, Buhweju is found in the south western Uganda consisting elevated ridges and mountains of western Mbarara city, about 300km far from Kampala, capital city. The area comprises most parts of the international Uganda geological sheet 76 which is geographically bounded by (9944373-999954) N and (166162-221728) E. The eastern side of the Western rift valley cuts and bounds the north western part of the area where as the central part has occupied by complex mountains of Buhweju. Some part of the area is accessible through minor roads which are branching out from the major asphalt roads running in the west, south and east parts of Buhweju. The area consist different district counties including Bunyarunguru, Buhweju, Bushenyi, Ntsida and others which made some parts of Buhweju easy to access. The area is generally densely vegetated with two extensive forests protected by the Ugandan Forestry department. The Kasyoha forest and the Kalinzu forest have covered large areas in the northern Lubare ridge and in the southwest of the study area respectively. However, areas covering the rift valley and the eastern most parts of Buhweju are relatively less vegetated where short grass and bushes are common.

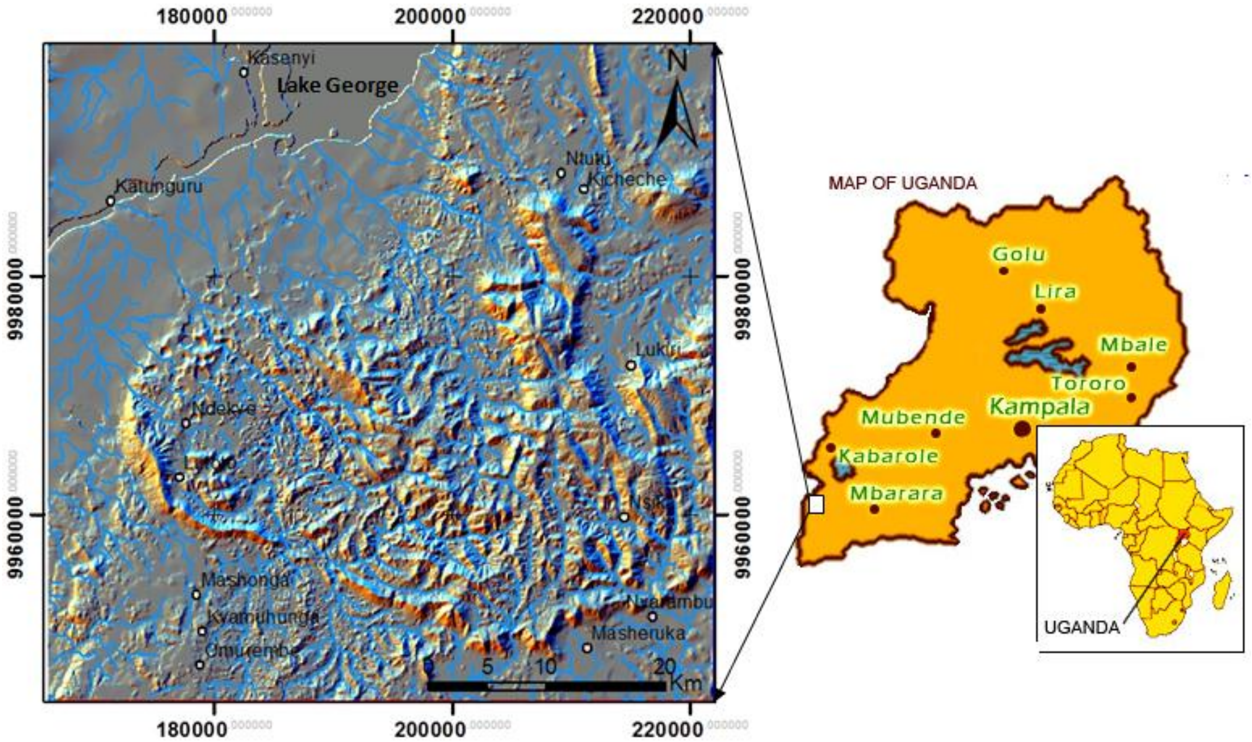

Figure 1-3: Location map of the study area

1.9. Justification for using various remote sensing data set

ASTER image data has offered advantage over Landsat data in both spatial and spectral resolutions hence, become increasingly important to geological and mineral mapping. A lot of Researches have already been conducted by utilizing ASTER data for its potential in discriminating lithologies and alteration areas especially in arid and semi arid regions. For example with the help of ASTER data, three additional lithologies namely granitic, granodioritic and a more maffic class consisting maffic gneiss, amphibole and variable mixtures of carbonates and silicates rocks have been mapped (Rowan & Mars, 2003). According to Khan & Glenn (2006) new strike slip faults and lithological units were mapped with the help of field and ASTER data that has yielded regionally significant results. Aeromagnetic and gamma ray surveys have been conducted in support of geological mapping and mineral exploration based on the fact that radioelement concentration and magnetic susceptibility change with geological units. Application and interpretation of aerial gamma ray surveys for geological, regolith, alteration mapping and applied geomorphology were well documented (Dickson & Scott, 1997; Shives et al., 2000; Wilford et al., 1997). Application and interpretation of aeromagnetic data for sub surface geological and structural mapping were summarized (Allek & Hamoudi, 2008; Jaques et al., 1997; Porwal et al., 2006) and more works have already been done by various researchers. However, the complex geological nature of an area remained fully unexplored through the analysis of single remote sensing data and hence, an integration of various data sets has required for better definition. Recently, researchers have already started the utilization of integrated data sets especially for improving available geological maps and mineral potential mapping. For example, the spectacular work by Schetselaar et al.(2008) has showed integrated interpretation of remotely sensed data to support geological mapping in Mozambique. The work has explained the appropriate methodologies employed for subsequent image enhancement, data integration and geological interpretation. The importance of remote sensing and GIS Technologies for improvements of geological structures interpretation and mapping has well documented (Saraf et al., 2002). Integration and analysis of Landsat ETM and

SRTM data was carried out by E. A. Owusu et al. (2006) which greatly improved the geological map of the Kibi area in Ghana. Integrated approach aided with field data discriminated lithological units with limited spectral contrast and covered by vegetation(Schetselaar et al., 2000). It is well established in many publications that lithology and structure play a determinate role in emplacement and localization of mineralization. Aeromagnetic and remote sensing data integration has been (Chernicoff et al., 2002) to identify crustal lineament control on magmatism and mineralization in northwestern Argentina. An integration of airborne and optical data have been utilized to map the regolith cover in Western Australia(Wilford et al., 1997).

1.10. Thesis organization

The organization of this research work is as follows:

1. Introduction
2. Previous work
3. Surface lineament interpretation
4. Processing and interpretation of gamma ray data
5. Processing and interpretation of aeromagnetic data
6. Data integration and geological map compilation
7. Conclusion and recommendations

2. PREVIOUS WORK

2.1. Regional geology, Structure and Mineralization

2.1.1. Regional Geology

Most portion of Uganda has underlain by Archean and Proterozoic basement rocks whereas the remainder covered by recent sediments and volcanic related to rift activities. According to various authors (Hepworth & Macdonald, 1966; MacDonald, 1966; Muwanga et al., 2001) these basement rocks of Gneissic granulite complex which were also referred to as Ugandan Basement complex (MacDonald, 1966) are further classified in to four tectonic belts based on their structural and metamorphic characteristics. These includes: Aruan gneiss and Watian granulites (Leggo, 1974) representing archean rocks of Toro-Ankole and western Nile regions, the Buganda-Toro belt which is sometimes called the Ruwenzori Fold belt (MacDonald, 1966; Tanner, 1970) consisting metamorphosed early proterozoic rocks, the Karagwe-Ankolean system (Elliot & Gregory, 1895) representing young proterozoic low grade rocks which are also part of Kibaran belt (Cahen et al., 1984) and the early proterozoic high grade Ubendian belt (Cahen et al., 1984) bordering the southern end of Tanzanian craton. In addition, the Mozambique Fold belt (Leggo, 1974) and its associated events have resulted relatively younger neoproterozoic basement rocks in eastern Uganda. The study by (Saggerson & Turner, 1972) also indicated that the Nyanza shield including both Nyanzian and Kavirondian systems, comprise rocks of gneissic complex of the northern Uganda and found well developed around Lake Victoria. Mesozoic and Cenozoic sediments and volcanic rocks which are related to the rift activities have covered the eastern and western borders of the country whereas; the down faulted western rift has apparently filled with tertiary and recent sediments.

The East African Rift System (EARS) is made up of three rift branches among which, the western branch runs from Tanzania craton, Tanganyika through Malawi and ends at western Uganda forming the Albertine rift system. The variable thickness of the lithosphere in western Uganda (Link et al., 2010), obtained from the geochemical signature of Virunga volcanoes of Toro-Ankolean, was explained as a cratonic root beneath the thrust belt in the Rwenzori regions. This recent study by Link et al. (2010) has therefore, concluded the existence of a continuous cratonic crust between Congo and Tanzania blocks in western Uganda covered by folded, thrusted and metamorphosed proterozoic and Archean units. According to the explanation given by Link et al. (2010) the Toro-Ankole region of the western Uganda basement is composed of locally migmatised gneisses interlayered with micaeous schists, amphibolites and quartzites of Buganda-Toro belt. The Mesoproterozoic age and NE-NNE trending Kibaran belt (Buchwaldt et al., 2008) has covered large areas of south and central Africa passing though Zambia, Tanzania, Brundi, Rwanda and terminate at SW Uganda. The kibaran belt is essentially intra-tectonic metasedimentary belt formed between 1400 and 900Ma (Pohl, 1994) consists two dominant supergroups namely the kibaran supergroup and the Brundian supergroup. Starting from its type area (Kibaran Mountains of central Congo) northwards along the strike to the corresponding Burundian supergroup and SW of Uganda, the kibaran belt is composed of schist, phyllite with some intercalated quartzite, conglomerate, and mafic-felsic volcanic rocks. The slightly metamorphosed metamorphic rocks of the Ankolean-karagwe group, covering most of the SW Uganda, has been found intercalated with gneiss and intruded by different suits of granite of the same source magma. In addition (Pohl, 1994; Rumvegeri, 1991) have overviewed and classified lithologies of the whole kibaran belt as lower, middle and upper kibaran units. Generally two geochronological studies have been conducted by Buchwaldt et al. (2008) on late Archean granitic rocks of Northern Uganda and by Ikingura et al. (1992) on granitic rocks sampled from Zaire, Burundi and SW Uganda. These have led to a conclusion that at least three distinctive tectonic events have been taken place in SW of Uganda which were consistent with granitic emplacement ages in various parts of kibaran belt.

2.1.2. Structure and Mineralization

It is concluded that structures and metamorphism in Pan-African belts including the various microcratons were orogenic (Black, I967 ; N. K. Grant, 1967 1969). It is also known that most of the east African countries are covered by oldest rocks which have been affected by orogenic structures. The Precambrian orogenic fold belts and shear zones, rift valley of Miocene times with associated volcanic centers and the Pleistocene warping form the major tectonic controls of Uganda. It has explained (Riad & El Etr, 1985) that the Precambrian orogenic belts have showed consistent trends as seen at Aruan and central Karamoja areas where the gneiss structures approximately trend North south and the Northwesterly trending folds continued to Karagwe-Ankolean of S W Uganda forming prominent topographic ridges.

Precambrian shear zones in Uganda appear in several places, particularly in the north. Among which, the Aswa shear zone (Shackleton, 1976) become extensive in several areas trending in north west direction. Other similar trending but relatively narrow and younger in age possibly related to Mozambique orogeny occur at Karomoja, Ancholi and west Nile regions (Riad & El Etr, 1985). The basins of Lake Edward, George and Albert and the Ruwenzori mountain blocks clearly represent major structural features of the western rift in Uganda. According to previous study by (Riad & El Etr, 1985) the rift movements in Uganda has began during early Miocene times and continued to mid-Pleistocene with major movements. The periods of faulting of the eastern and northern part of western rift have also believed to be contemporaneous with varied amount of movements from place to place (Baker, 1971). Two different views have been suggested regarding the interpretation of structural behaviour of north-eastern kibaran belt. According to (Klerkx et al., 1987; Pohl, 1994; Rumvegeri, 1991) extensional tectonics with sedimentary cover decollemented over the basement (D1) and granitic magmatism were considered as early structural development followed by compressional tectonic accompanied with upright folds (NE-SW) and shearing (D2). Whereas, the recent geochronological and geochemical investigations on alkaline intrusive suit led to interpretation for Kibaran evolution that crustal thickening was resulted due to mantle derived intrusions which reflected tectonic collapse (Tack et al., 1994). The general geodynamic model, tectonic movements and associated deformational events in kibaran orogeny have been presented in detail (Rumvegeri, 1991).

The lithostratgraphic and tectonic setting of gold mineralization in the Archean cratons of Tanzania and Uganda has been discussed by (Gabert, 1990) and showed the control of lithology, metamorphism and tectonic on location of gold mineralization. Accordingly three main types of primary gold mineralization of Nyanzian green stone belt have been recognized. These are strata bound syngenetic gold mineralization, epigenetic hydrothermal gold mineralization and epigenetic metasomatic gold mineralization. The study by Harris, (1961) showed that the majority of known gold-quartz vein deposit occur in conjugation with mineralized shear zones. He also noted that in supercrustal rocks eluvial gold occurs probably derived from auriferous quartz veins which may be related to the late orogenic granitic activity. Panning of alluvial materials and physical searching of mineralized outcrops were the various practices which have been used in the past to discover mineral deposits in the kibaran belt. However, recently geochemical and geophysical methods have been used which have resulted in the recognition of different mineralized belts within kibaran like in Burundi and Tanzania (Radulescu, 1982). According to the inventory of mineralized zones that has been made so far, (Pohl, 1994) has synthesized the general aspect of mineralization of kibaran belt. Thus the possible mineralization recognized in the belt include: mineralization syngentic with the kibaran sediments, Mineralization associated with mafic layered intrusions and mineralization associated with tin granites. Among which mineralization associated with tin granites represent the base of old and present mining within kibaran belt.

2.2. Local geology, strucutre and mineralization

Explanation of the geology of Buhweju (Reece, 1961) and related reports are the only existing geological information available in the area and all of which form the foundation of this work . According to the explanation, rocks of Buhweju are classified in to five groups. The Igara group represents a sedimentary sequence which has been metamorphosed and granitized units including schist, quartzite and granitic rocks. The Buhweju group consist a sequence of psammitic and pelitic rocks unconformably lying on the Igara group. They have recrystallized the basal formation granitized contemporaneously with the Igara group. Ibanda quartzite forms an isolated outcrop and its relationship with Igara and Buhweju groups is not known. Doleritic dykes and quartz veins represent intrusive rocks which are younger than the Buhweju but older than the Pleistocene rocks. The Pleistocene rocks are poorly consolidated and volcanic occupying the rift valley. The various volcanic fields consisting of fine grained and highly calcareous tuffs were well explained by (Reece, 1961). The Buhweju group is further classified in to five different lithologic units including Lukiri mudstone, Isingiro conglomerate, Lubare quartzite, Kasyoha shales and Munyoni quartzite in the order of from bottom to top in lithological succession. The geological succession and description of each geologic units of the area has shown in (Table 1-2).

The general geological history and sequence of geological events of the area have been summarized as follows: (1) deposition of the Igara group under shallow water marine condition followed by intrusion of doleritic rocks. (2) Folding of the Igara group about north trending axes, accompanied by low grade (greenschist) regional metamorphism. (3) Deposition of the Buhwehu group as deltaic sediment and later as shallow water conditions. (4) Folding of parts of the Buhweju group along WNW trends with some refolding of the Igara group accompanied by local felspathisations and metasomatism. (5) Intrusion of quartz veins. (6) Formation of rift valley and intrusion of dolerites and quartz veins. (7) Deposition of Pleistocene sediments.

Formation		*Description*	*Thickness in feet*	*Age*
Bunyaruguru and other Volcanics		Tuffs and agglomerates with occasional lavas	Up to at least 430	Pleisto-cene
Kaiso and Epi-Kaiso Beds		Gravels, sands, silts and clays . .	Greater than 400	
		Unconformity		
Munyoni Quartzites	Buhwezu Group, probably Karagwe-Ankolean	Quartzites with minor pelitic bands, dominantly psammitic	1,200 ; top not seen	Pre-Cambrian
Kasyoha Shales		Mudstones, shales and slates with minor quartzite bands, dominantly pelitic	1,000–3,000	
Lubare Quartzite		Quartzite with occasional lenses of grit, conglomerate and mudstone; upper part often mylonitised and brecciated	0–3,800	
Isingiro Conglomerate		Conglomerate and grit with minor pelitic grit and occasional quartzite lenses	0–1,200	
Lukiri Mudstones		Mudstones and occasional shales, often gritty	0–200	
		Unconformity		
Igara Group . .		Metamorphic complex of pelitic and semi-pelitic schists, quartzites, amphibolites, gneisses and granites	Unknown	Pre-Cambrian
Ibanda Quartzite . .		Thoroughly recrystallised quartzite with rare pelitic lenses	Unknown	
		INTRUSIVE ROCKS		
Doleritic dykes . . Quartz veins.		Dolerites and meta-dolerites		

Table 2-1: Stratigraphic units of the study area. After(Reece, 1961)

The structure of the area was described by (Reece, 1961) from both field data and thin section analysis especially for the Igara and Buhweju groups. The structure of Ibanda quartzite is not known but some explanations suggested that it has affected by tectonic thickening which caused its size disproportional. Rift valley and associated Pleistocene rocks didn't exhibit visible tectonic structures resulting most structural explanations were entirely of topographical.

Foliations and lineation were explained as common structures apparent on schist, quartzite and gneiss of the Igara group. Almost parallel NW foliation has been described on gneissic rocks marked by mineral banding and preferred direction of feldspar porphyroblasts. Foliations were also described on schist with weak planes marked by white mica flakes. Interpretations have showed that two foliations were affected the Igara group rocks. The first dominant foliation was associated with early folding events trending NNW and nearly isoclinals nature. The second foliation (slip cleavage), evidenced by drag folds and fracture cleavage, was found superimposed on the older folds. Beddings, cleavages and linear structures were described on various lithological units of the Buhweju group which led to an interpretation that the Buhweju group has been folded in WNW trending axes.

Generally the Igara group has folded isoclinically about steeply dipping northerly trending axial planes with a refolding about WNW trending axes in the south west. The Buhweju group has folded about horizontal in WNW trending axes with intensity of folding increase to the south.

According to the various unpublished reports, first mining operations were carried out by African smelters to extract iron ore from ferruginous brecciaed zones in the kasyoha shales. In the following years (Cobme,

1932) economic quantities of alluvial gold were found in south of Lubare ridge and a deposit was opened by a private company on the Buhweju plateau (Wayland, 1934). Various compilation works on the mineral resources of Uganda showed that Buhweju was still the main gold producer came entirely from wide spread alluvial mining where the source rock is still unknown. Alluvial of Karagwe-Ankolean rocks occur in streams, stream courses and swamps with heavily vegetated surroundings. Different observations have also indicated that the gold was mostly found on the lower parts of the gravel and couldn't be detected in the bed of the stream. However, at some areas like Kanyambogo and Kitaka gold has been mined from the veins cutting the basement Igara schists. According to Wayland (1934) reef gold has also been found in Muti area forming stockwork of quartz strigers transecting a quartzite bore of pyrite and fine gold. He has also showed the gold occurrences in the sandy transition of the quartzite and pelites. Three sulphide veins have also been identified (Reece, 1961) at Kitaka, Kampono and Kanyambogo lead-zinc mines emplaced in shcists and gneiss. In these mines coarse crystalline gold also occur in vughs lined by quartz crystals. In Kitaka mine galena, chalcopyrite and gold have been carried by undulating quartz veins emplaced in shears within metadolerite. According to the explanation by Reece (1961) gold mineralization is in general epithermal as is shown by its often coarsely crystalline occurrence in vughs. As inferred from the previous study by Pohl (1994) mineralization has been started ca 1250 Ma related to post orogenic rifting. Mineralization at ca 950 Ma however considered as dominant which has been related to post orogenic metamorphism.

3. MULTISPECTRAL IMAGE PROCESSING AND INTERPRETATION

3.1. Introduction

Multispectral remote sensing basically depends on measurement of electromagnetic energy (EM) reflected from the various surface cover in ranges of wavelength bands. The landsat ETM+ and ASTER are common multispectral remote sensors which are being used to acquire Earth's surface information. Immense works have already been conducted in geological mapping by utilizing the multispectral data sets especially in Arid and semi arid areas (Benomar & Fuling, 2005; Qari, 1992; Rowan & Mars, 2003; Wickert & Budkewitsch, 2004; Won-In & Charusiri, 2003). Depending on the presence of outcropping lithology, the various ASTER and Landsat wavelength regions have been used as a complement for lithological mapping. Lithological units which are mainly composed of transition metals like iron, carbonates and hydroxyl minerals could be easily identified on ASTER VNIR and SWIR bands entirely due to absorption feature observed on these mineral spectra. However, rock forming minerals like quartz and feldspar don't readily exhibit absorption features due to their less susceptibility to weathering and hence less identified through analysis of mineral spectra. For the areal coverage of multispectral data in Buhweju is shown in (Figure 1-2) Bothe ASTER and landsat scenes were projected to the same projection system, UTM zone 36S projection and WGS84 datum. The two ASTER scenes covering the study area were mosaiced at resolutions of 15m, 30m, and 90m using ENVI image processing software. Image resampling was carried out as required usually at resolution of 15m and 30m during various image enhancements. The radiometric characteristics of both ASTER and Landsat are generally summarized in (Table 1-1).

Standard image processing algorithms such as selected band composite, principal component analysis, decorrelation stretch and rationing techniques were applied to both Landsat ETM and ASTER data to get lithological, structural and morphological information of the area. An overview of these techniques is given by (Benomar & Fuling, 2005; S. P. Chavez et al., 1991; Gad & Kusky, 2007; Gillespie et al., 1987; Yesou et al., 1993). The aim of this chapter is therefore, to map various lithological units and hence to evaluate the importance of multispectral data for lithological mapping in Buhweju area.

3.2. Correction for Vegetation Effect

Terrains in tropical and semi tropical areas are most often covered with vegetation of various types. Reflectance of dense vegetation interferes with barren land surface, thereby obscuring the information of the underlying surface. This greatly affects geological mapping of vegetated areas. The previous work by (Crippen & Blom, 2001) has showed that, in multispectral images the accuracy of discriminating lithologic units will be lost if the vegetation cover exceeds the land surface, which is typically the case in Buhweju area. Therefore minimizing the effect of vegetation from images should be carried out prior to any interpretation. However, this becomes effective only if the image pixels contain spectra of both vegetation and land surface unlike in Buhweju where some areas are completely covered with dense protected forest. Normalized Difference Vegetation index (NDVI) images were produced for both ASTER and Landsat images (Figure 3-1) and then the densely forested areas were masked out for they consist purely of vegetation spectra. Vegetation suppression, in which most of the methods are also described by (Crippen & Blom, 2001) was then applied for the rest of areas with open canopies. Vegetation suppression helps in better interpreting geologic features by removing the vegetation spectra from red and near infrared bands of multispectral images. The algorithm models the amount of vegetation per pixel calculates the relationship of each input band with vegetation and decorrelates the vegetation component of the total signal pixel by pixel for each band. The results were then compared with the original devegetated images

(Figure 3-2) and used for further enhancements and interpretations. Most of the subsequent image enhancement and analysis were made on the eastern part of Buhweju due to its complexity covered by Precambrian Buhweju and Igara groups as compared to the western part, covered by recent volcanic and sediments.

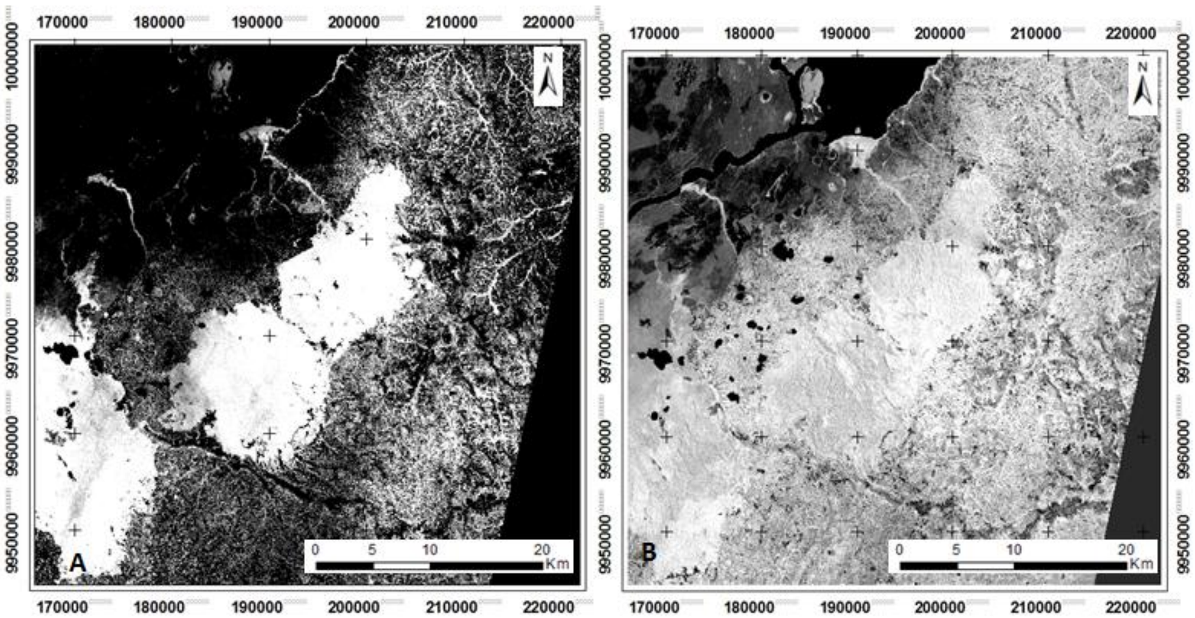

Figure 3-1: NDVI Images of the study area A) ASTER image B) Landsat ETM+

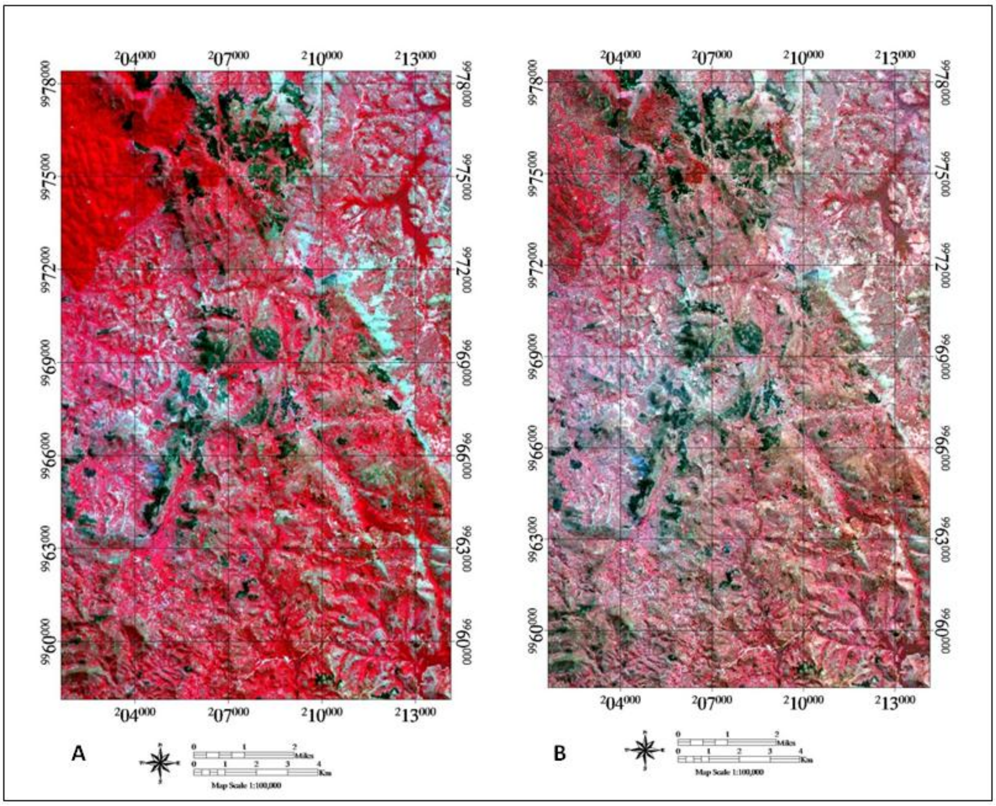

Figure 3-2: Subscenes of ASTER A) before B) after suppression

3.3. Univariate Analysis of ASTER and Landsat ETM+ data

Selection of appropriate triplet color composite images was performed in two different ways; the correlation coefficient method and the Optimum Index factor (OIF) method. The less correlated bands are good for image visualization in RGB color space (Drury, 2001).

3.3.1. Correlation coefficient method

The correlation Coefficient was calculated for the reflective bands of Landsat ETM data (Table 3-1). Band4 has showed less correlation with the other reflective bands followed by band5 and band7. Therefore the RGB images 751 and 541 (Figure 3-2) are selected for better visual interpretation of the area. Similarly univariate correlation coefficient analysis was applied to the nine reflective ASTER VNIR/SWIR bands after resampling the SWIR bands to the same resolution with VNIR bands (15m).

	Band 1	**Band 2**	**Band 3**	**Band 4**	**Band 5**	**Band 7**
Band 1	1					
Band 2	0.9	1				
Band 3	0.8	0.92	1			
Band 4	**-0.41**	**-0.17**	**-0.2**	1		
Band 5	0.12	0.42	0.6	0.48	1	
Band 7	0.35	0.56	0.77	0.06	0.87	1

Table 3-1: Correlation coefficient of Landsat ETM+ data in the study area

A positive correlation has observed between the nine ASTER VNIR-SWIR bands (Table 3-2). The first three bands especially band 1 showed very low correlation with the other bands except band 2 (0.81). Therefore an appropriate triplet bands in RGB 741, 731 and 721 (Figure 3-2) are selected which gave better color composite for visual interpretation. Generally, ASTER741, ASTER721, and ETM751 were selected for further interpretations of lithology and structures since they showed better reparability in geology.

	Band 1	Band 2	Band 3	Band 4	Band 5	Band 6	Band 7	Band 8	Band 9
Band 1	1.00								
Band 2	0.81	1.00							
Band 3	0.17	0.53	1.00						
Band 4	0.29	0.75	0.87	1.00					
Band 5	0.33	0.78	0.79	0.98	1.00				
Band 6	0.37	0.81	0.78	0.98	1.00	1.00			
Band 7	0.33	0.78	0.78	0.98	1.00	1.00	1.00		
Band 8	0.34	0.79	0.76	0.97	0.99	0.99	1.00	1.00	
Band 9	0.24	0.73	0.78	0.97	0.98	0.98	0.99	0.99	1.00

Table 3-2: Correlation coefficient of ASTER VNIR-SWIR data of the area

3.3.2. Optimum Index Factor (OIF)

Selection of better color composite for visual interpretation of images was also made by the statistical approach, Optimum Index Factor. OIF approach takes into account the total variance within bands and the correlation coefficient between bands (Benomar & Fuling, 2005). The individual bands were enhanced and stretched separately before the technique was applied and the SWIR and TIR ASTER bands were resampled to the same resolution with ASTER VNIR bands. Triplets with higher values of OIF (Table 3-

3) were used for better extraction of lithological information (Figure 3-4) since they use bands with highest variance and least redundancy (Qaid & Basavarajappa, 2008).

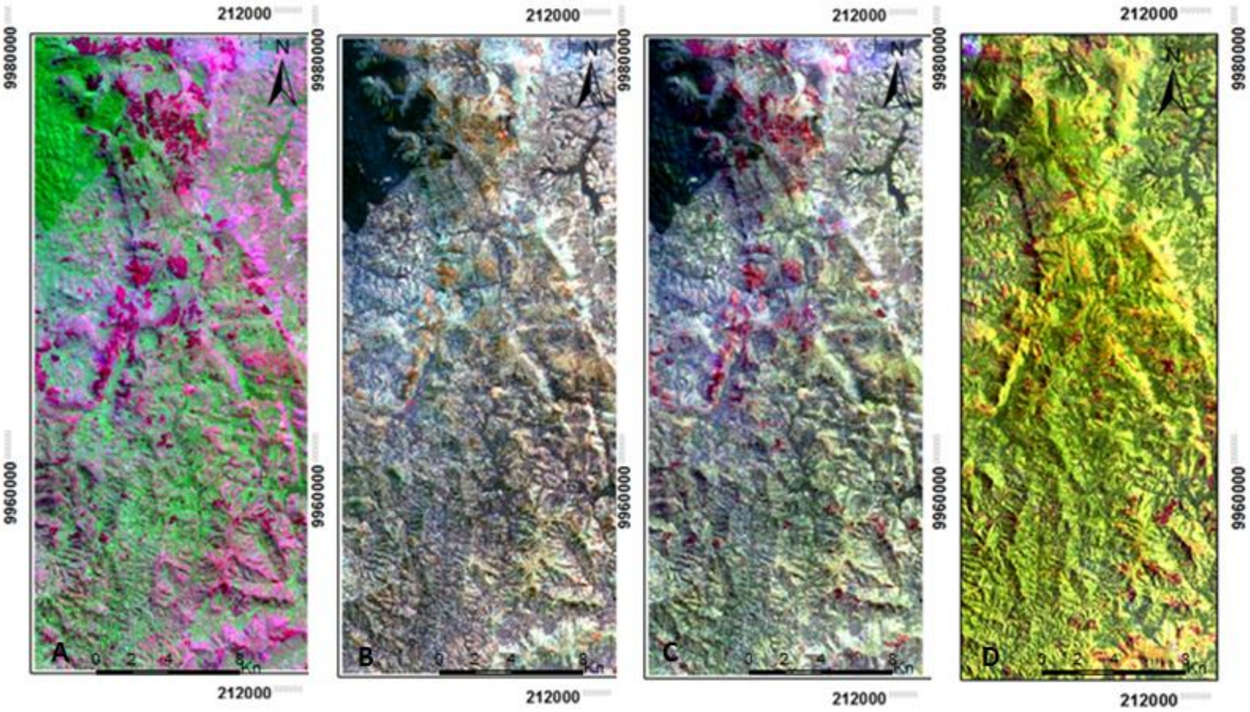

Figure 3-2: Subscence of Landsat ETM and ASTER color composite images in (RGB) A)ASTER731 B)ASTER721 C)ASTER741 D)ETM751

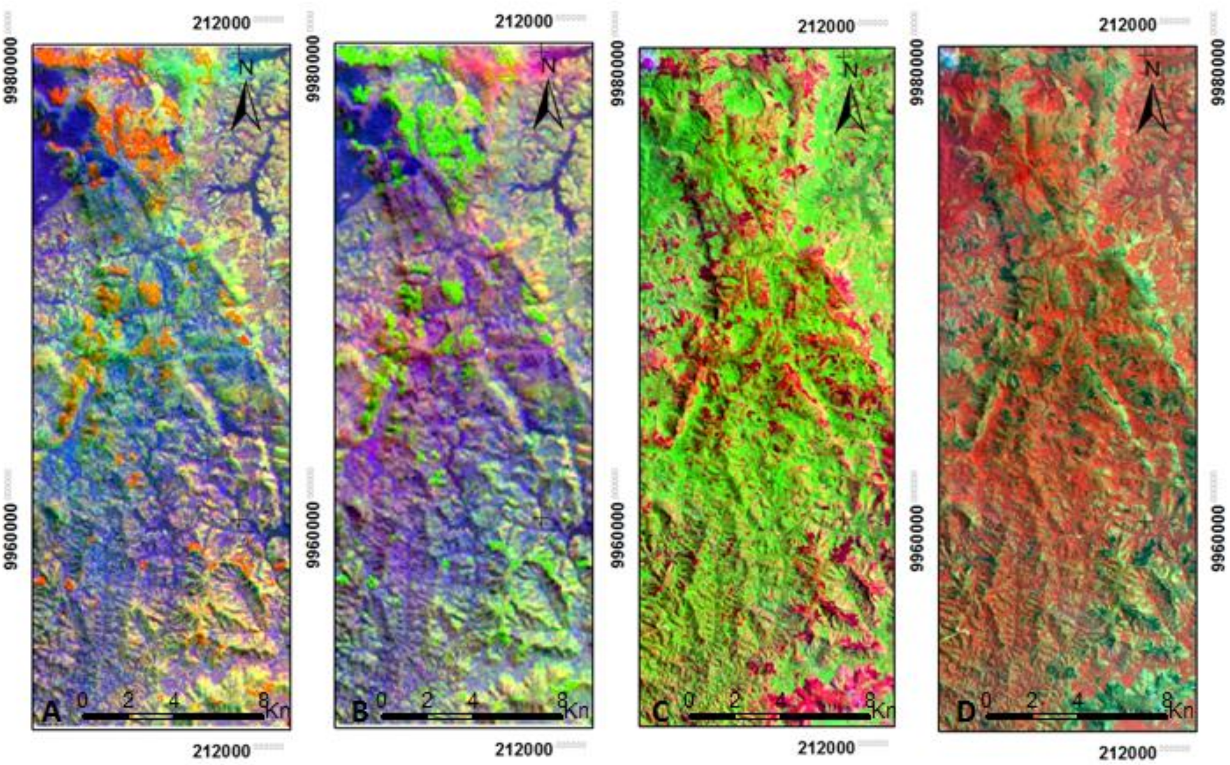

Figure 3-3:Subscence of OIF color composite in RGB order A) ASTER TIR13 VNIR2 VNIR3 B) ASTER VNIR1 TIR13 VNIR3 C) ETM742 D) ETM431

No.	ASTER (VNIR-SWIR) bands		Landsat ETM+ bands	
	Color composite (RGB)	OIF rank	Color composite (RGB)	OIF rank
1	VNIR 1, TIR 13, VNIR 3	88.9	ETM 741	25.5
2	VNIR 1, TIR 14, VNIR 3	88.67	ETM 431	18.6
3	VNIR 1, TIR 11, VNIR 3	87.55	ETM 541	17.2
4	VNIR 1, TIR 11, VNIR 3	87.05	ETM 421	15.4
5	VNIR 1, TIR 10, VNIR 3	96.34	ETM 742	12.1
6	TIR 13, VNIR 2, VNIR 3	82.71	ETM 432	11.3

Table 3-3: The first six highest OIF index ranking of ASTER and Landsat ETM+ bands

3.4. Principal component analysis

The various bands in multispectral images are highly correlated and often appear similar giving the same and redundant information. The PCA is then a technique designed to reduce such information redundancy in multispectral images. It is a statistical method that transforms a multivariate data set of intercorrelated variables into a data set consisting of new uncorrelated variables (Benomar & Fuling, 2005; Qari, 1992; Yesou et al., 1993).The first principal component accounts for as much of the variability in the data as possible and each succeeding components accounts for the remaining variability. PCA is then a widely used enhancement technique in which the information content of the different bands become compressed and confined within the first few bands. The individual Landsat ETM and ASTER bands were normalized to reduce errors encountered due to different effects like sensor quality and difference of dynamic range (Yesou et al., 1993). The PCs were calculated for the normalized 6 Landsat ETM, 9 ASTER VNIR-SWIR and 6 ASTER SWIR spectral bands. The individual PC image or any three of the resulting components were then enhanced linearly and displayed as single or composite images for further interpretation of lithology and structures. Statistics were computed for the individual images and percentages of data variations were produced.

3.4.1. PCA on ASTER data

PCA was applied to the nine ASTER VNIR-SWIR bands since they account better information in identifying rocks composed of iron, carbonate and hydroxyl minerals. From the computed statistics and percentage of data variation (Table 3-4) the first PC image showed the highest variation (79.75%) which goes decreasing and the last two PCs contribute very small variance that mostly accounts for noise. As shown in (Table 3-4), PC1 explains the highest variance (albedo) with positive loadings at each band. Lithological and structural information were extracted through visual interrelations of the PC1 image (Figure 3-4). PC2 attains most of its information from band3 and band1and this image enhanced the exposed Lubare and Ibanda quartzites having bright tone on image. Drainage patterns were observed on PC3 and PC4 images and the associated structures were interpreted. However, the color composite images of PCs were not used in interpretation due to over-emphasized color variations. Principal component analysis was also applied on the six normalized SWIR bands of ASTER data to get more information that couldn't be obtained from the VNIR-SWIR bands. The statistics was computed showing the loadings of eigenvalues and percentages of variance (Table 3-5). The first principal component has explained the highest percentage variance of all the bands (98.88%) with all positive loadings. PC2 has high loadings at band1 and band3 and the image enhanced quartzite ridges of the area. The individual images were then enhanced and displayed for further interpretations.

Eigen vector	Band1	Band2	Band3	Band4	Band5	Band6	Band7	Band8	Band9	Variance (%)
PC1	0.21	0.34	-0.03	0.34	0.39	0.38	0.38	0.39	0.36	**79.75**
PC2	0.44	0.30	0.74	0.24	-0.80	-0.10	-0.12	-0.19	-0.22	**8.77**
PC3	-0.42	-0.63	0.54	0.24	0.13	0.10	0.14	0.11	0.14	**6.77**
PC4	-0.10	-0.1	-0.35	0.76	0.10	0.11	-0.10	-0.26	-0.45	**1.9**
PC5	-0.60	0.52	0.10	0.26	-0.32	-0.20	-0.15	-0.05	0.37	**0.92**
PC6	-0.46	0.35	0.15	-0.31	0.50	0.13	0.10	0.03	-0.55	**0.65**
PC7	0.15	-0.03	-0.03	0.00	0.70	-0.21	-0.40	-0.05	0.40	**0.52**
PC8	0.10	-0.03	-0.04	0.18	0.21	-0.70	-0.21	0.63	-0.16	**0.37**
PC9	-0.02	-0.02	0.02	-0.03	-0.03	0.53	-0.80	0.32	0.00	**0.36**

Table 3-4: Eigen vector loadings of principal components for ASTER VNIR-SWIR data and their variance

Eigen vector	Band1	Band2	Band3	Band4	Band5	Band6	Variance (%)
PC1	0.13	0.13	0.15	0.12	0.13	0.96	**98.88**
PC2	0.67	0.36	0.48	0.26	0.20	-0.28	**0.68**
PC3	0.71	-0.27	-0.43	-0.29	-0.38	0.10	**0.32**
PC4	0.12	-0.21	-0.55	0.05	0.61	-0.04	**0.09**
PC5	0.06	-0.85	0.50	0.00	0.15	0.01	**0.03**
PC6	0.06	0.10	-0.01	-0.76	0.64	-0.01	**0.01**

Table 3-5: Eigen values of the principal component of ASTER SWIR data of the area.

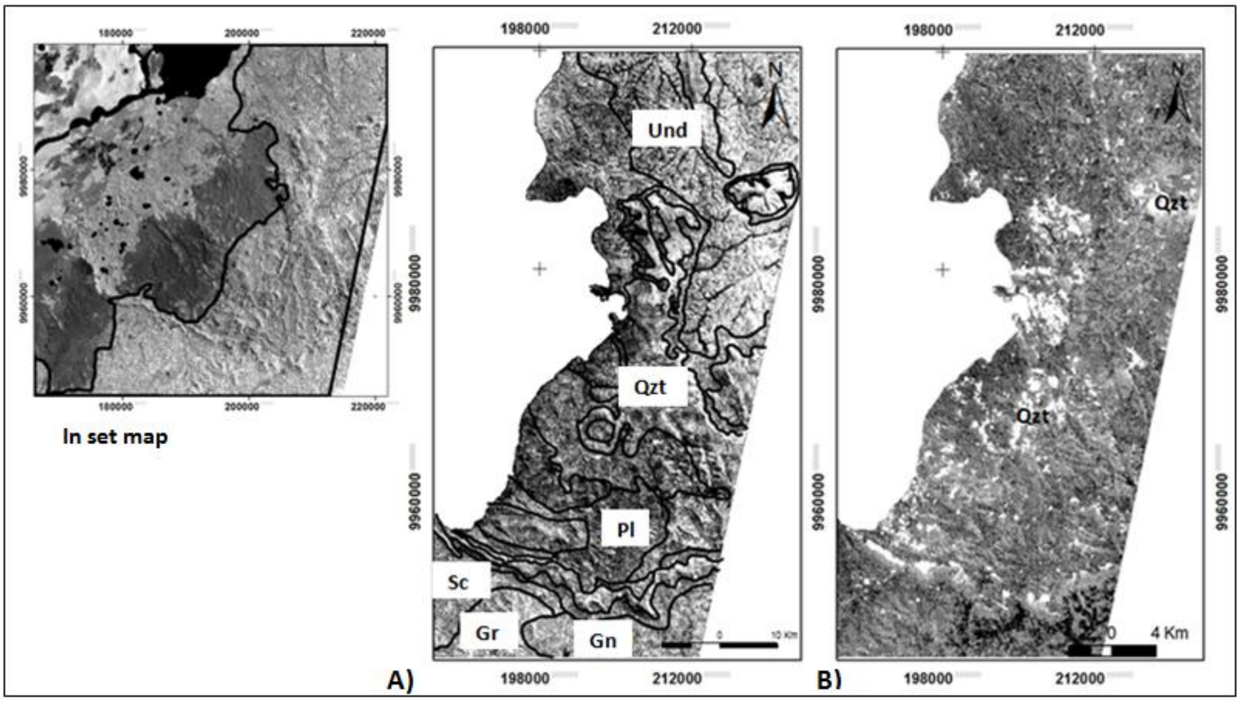

Figure 3-4: Subscens with interpreted lithologies A) ASTER VNIR-SWIR PC1 B) ASTER VNIR-SWIR PC2 Sc=schist Gr=granite Gn=gneiss Pl=pelite Qzt=quartzite Und=Undifferentiated unit

3.4.2. PCA on Landsat ETM+ data

Principal component analysis was computed for the six reflective bands of Landsat ETM image (Table 3-6). The first principal component explains the highest variance (63.34%) of all bands followed by the second (17.16%). PC1 has positive loadings at all bands with maximum information coming from band 3 and mainly used for lithological interpretation and PC3 were mostly used for interpreting lineaments of the area (Figure 3-5).

Eigen vector	Band1	Band2	Band3	Band4	Band5	Band7	Variance (%)
PC1	0.38	0.43	0.50	0.01	0.45	0.47	**63.34**
PC2	0.08	0.21	-0.13	0.91	0.14	-0.28	**17.16**
PC3	-0.72	-0.27	-0.02	0.17	0.47	-0.41	**12.02**
PC4	-0.56	0.53	0.47	-0.13	-0.15	-0.40	**2.18**
PC5	-0.01	-0.34	0.55	0.35	-0.60	0.31	**1.25**
PC6	-0.15	0.54	-0.46	0.10	-0.44	0.54	**1.06**

Table 3-6: Eigen values of principal components of Landsat ETM data and their variance

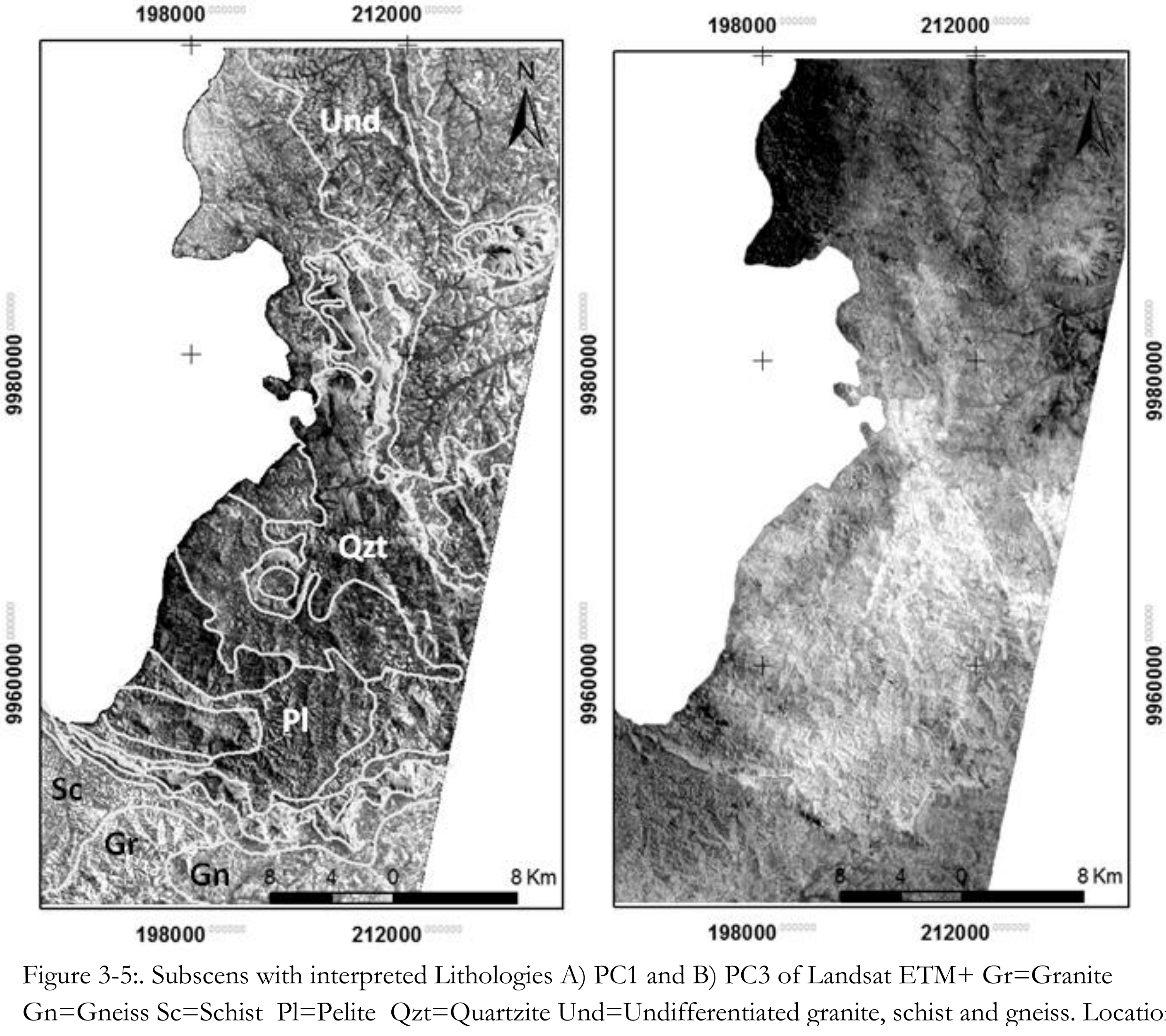

Figure 3-5:. Subscens with interpreted Lithologies A) PC1 and B) PC3 of Landsat ETM+ Gr=Granite Gn=Gneiss Sc=Schist Pl=Pelite Qzt=Quartzite Und=Undifferentiated granite, schist and gneiss. Location

3.5. Summary of multispectral processing and interpretation

The complex topographic features, less variability in reflectance of the various lithologies and vegetation cover have greatly influenced the amount of geological information that could be obtained from the enhanced composite images. Correlation coefficient, OIF and PCA techniques were applied to both ASTER and Landsat ETM+ data. Transformations of color space to IHS and decorrelation stretch were also performed on various composite images but interpretation became difficult due exaggerated colors. Consequently, the different PC combinations and band ratios couldn't be used to enhance the various rock types composed of mainly of iron, carbonates or hydroxyl minerals. However, the univariate and PCA analysis have resulted better enhanced images for photo geological interpretations. Combinations of color composite image including ASTER721, ASTER741 and ETM751 were found considerably useful for lithological and structural interpretations of the area. In addition the various single PC images including PC1 (albedo) images were used to interpret surface lineaments of the area. The multispectral interpretation of the area has discriminated some lithologies which were mapped as same unit by (Reece, 1961). For example, the previously mapped undifferentiated granite, gneiss and schist have separated in to two different units based on the absence and presence of drainages. Accordingly, a generalized discussion on geology and an interpreted lithological map (Figure 3-6) of the area were made from the analysis presented above with a comparison of previous study and field work (Table 3-7).

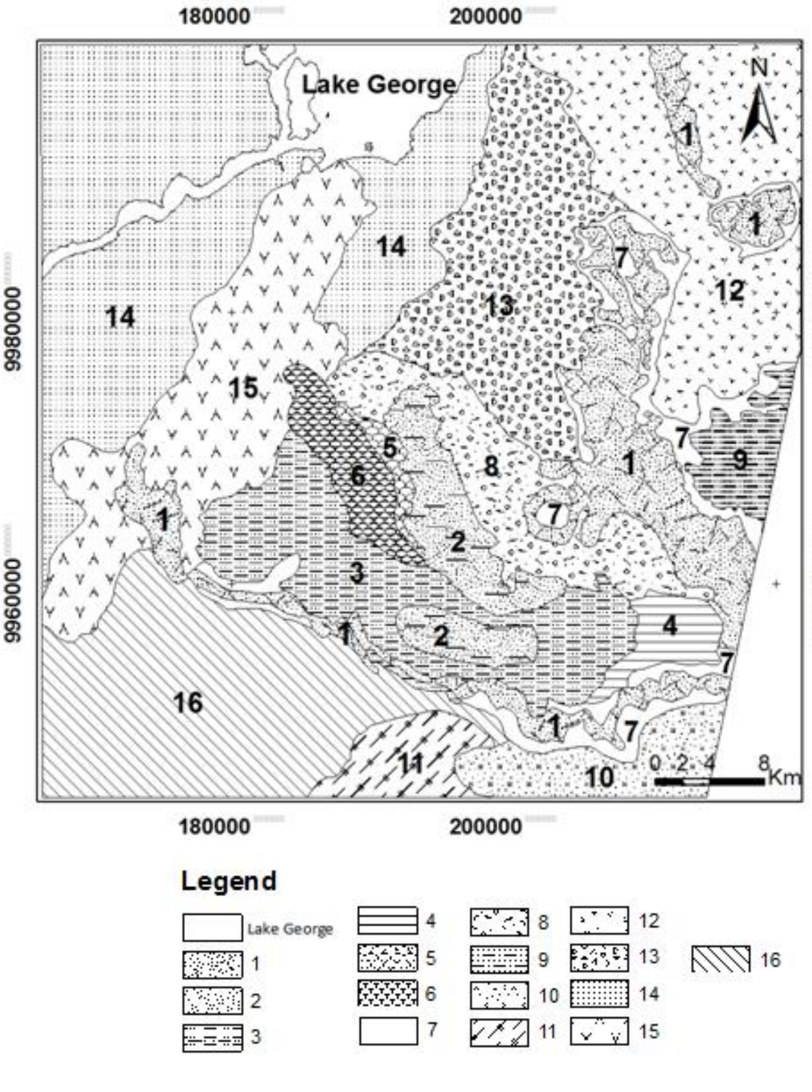

Figure 3-6: ASTER and Landsat interpretation map of Buhweju

Unit name (younger to older)	Image characteristics	Field observation	A.W.Reece,1961
Unit 15	Low relief less resistant rough texture due to volcanic depression	Whitish weathered and friable rock covering the rift, lakes are prominent and drainage are less	Tuff and conglomerate
Unit 14	Low relief, very smooth texture, less resistant and no drainage developed	Rift filling sediments including sand and conglomerate	Conglomerate, sand, silt and clay
Unit 7	Sloppy relief, smooth texture and bright image tone	Quartzitic conglomerates, steeply dipping and bounding quartzite ridges having reddish to greyish color	Conglomerates and grits
Unit 8	Low relief and subdued topography, smooth texture, less resistant with few drainage patterns	Less resistant weathered and friable pelites and politic schist	Pelite with quartzite bands
Unit 6	Low –medium relief, covered with vegetation having rough texture defining NW-SE pattern	No access due to dense protected forest	Pelite with quartzite bands
Unit 5	Low relief, covered and has smooth texture	No access due to dense protected forest	Pelite with quartzite bands
Unit 3, 4 and 9	Low-medium relief, rough texture, vegetated, developed drainages and dissected terrains	Resistant, reddish weathered color and dissected terrain	Pelite with quartzite bands
Unit 2	High relief, resistant, rough texture and drainage features	Resistant quartzite at the top, down slope covered by less resistant material	Quartzite with pelite bands dominantly psammitic
Unit 1	High relief, resistant, bright image tone	Well bedded, dipping and resistant ridges	Ibanda and Lubare quartzite
Unit 11 and 16	Low-medium relief, shattered, rough texture	Not accessed	Politic schist
Unit 12	Low-medium relief, dendritic drainage, bright image tone	Not well accessed	Undifferentiated granite, gneiss and schist
Unit 13	Low relief, no well developed drainage, less resistant rock	Dominantly schist and very weathered gray to dark color	Undifferentiated granite, gneiss and schist
Unit 10	Low relief, smooth, bright tone with less drainages	Gneissic/granitic rocks covered with alluvial and weathered exposed part	Gneiss

Table 3-7: Result of image interpretation based on image characteristics in comparison with field observation and lithologies interpreted by Reece, (1961).

4. SURFACE LINEAMENT INTERPRETATION

4.1. Introduction

Different definitions have been given since early times for the commonly used term in geology called 'Lineament'. However, most researchers have agreed that lineaments are mappable linear or curvilinear surface features which distinctly differ from adjacent patterns and presumably represent topographic expressions and subsurface phenomenon (Gupta, 1991; Masoud & Koike, 2006; O'Leary et al., 1976; Williams, 1983). Lineament extraction from multispectral imageries has been used extensively basically to determine the structural grain of a region and for various other purposes like mineral exploration. Multispectral satellite images are considered to be better tool in discriminating lineaments since they are obtained from varying wavelength intervals of the electromagnetic spectrum (Casas et al., 2000). According to (Abdullah et al., 2010; E. A. Owusu et al., 2006; Sarapirome et al., 2002; Singh & Dowerah, 2010; Soulakellis et al., 2006). Manual interpretation and automatic extraction are the two commonly used methods to extract lineaments from multispectral images. In this study visual extraction method was applied on ASTER, Landsat ETM and SRTM DEM images to discriminate lineaments of the area. Elevation data provides the topographic expressions of an area and have been applied for structural interpretation by various investigators in the past (Henderson et al., 1996; A. E. Owusu et al., 2006; Soulakellis et al., 2006). Elevation data can be represented in different forms among which the grid forms (DEMs) are preferably useful for interpreting linear geologic structures which have topographic expressions due to offset of the surface. The ability of producing different shaded relief images because of the freedom to select illumination from any angle (Henderson et al., 1996) makes DEM selectively useful over Arial photographs (Abdullah et al., 2010; E. A. Owusu et al., 2006; Sarapirome et al., 2002; Singh & Dowerah, 2010; Soulakellis et al., 2006). According to the authors, solar elevation and azimuth are important elements to examine topographically related and dependent features. DEMs could also be fused with other multispectral images to increase interpretability and obtain more information than can be derived from each of the single image alone (Soulakellis et al., 2006). The various image enhancement techniques including directional, edge and soble filters can be applied to DEM to enhance different linear structures (Henderson et al., 1996). Therefore, extraction of surface lineament, assess their general pattern and density to decipher structural information of the area, is the main aim of the chapter.

4.1.1. Multispectral Interpretation

Knowledge and experience of the interpreter plays great role in visual interpretation. Image interpretation criteria such as topographic valleys, linear ridges, scarps, troughs, systematic river offsets, vegetation patterns, rock boundaries and sudden tonal variations are used to identify lineaments. The various color composite and PC images which were produced in chapter three are also used for lineament interpretation. In such a way that the composite images of ASTER721, ASTER741, ETM541, ETM751 and stretched individual landsat ETM bands (Figure 4-1) were mainly used for lineament extraction. The albedo images represent most of the information contained in ASTER and Landsat ETM bands and were highly valuable for lineament interpretation of the area. Directional filters are useful in extracting linear features by creating artificial effects (Drury, 2001). Large and small scale features could be extracted from high pass and low pass filtered images. Edge detection or directional filters were also designed to extract linear features oriented in specific directions. The gradient-Soble filter (Table 4-1) was applied to Landsat ETM band 5 as this image gave better boundary delineation.

The final lineament map (Figure 4-2a) was then generated from successive interpretations made above. A total of about 243 lineaments were extracted from multispectral image interpretations. The azimuthal statistics (Figure 4-2b) showed that most of the extracted lineaments are NNW-SSE and NNE-SSW trending and mainly concentrated at the central part of the Buhweju complex.

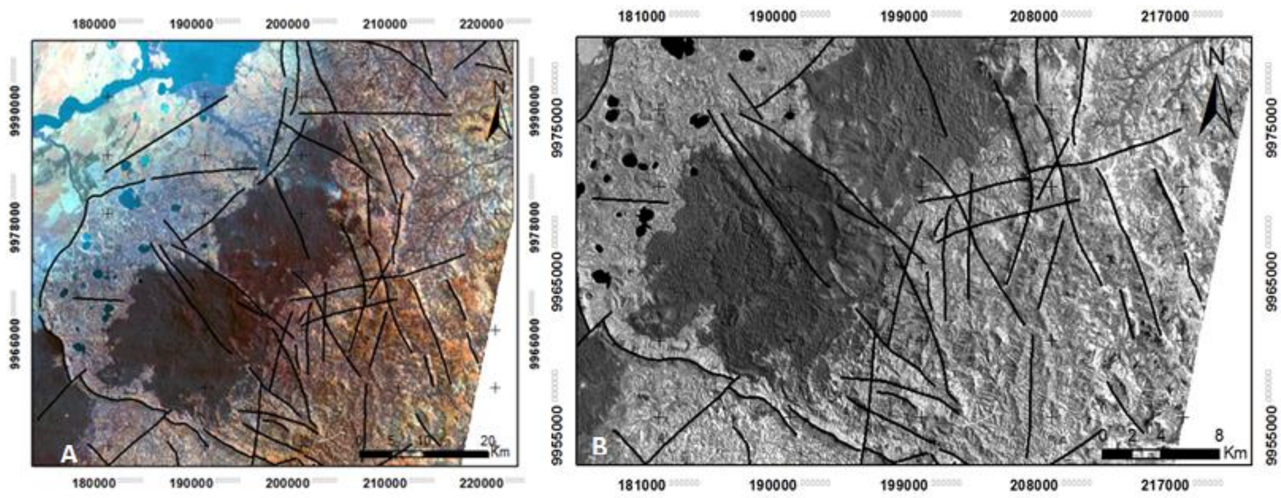

Figure 4-1: Subscenes of A) ASTER 721 in RGB order B) Landsat ETM5 overlaid by with extracted lineaments

	N-S			NE-SW			E-W			NW-SE		
	-1	0	1	-2	-1	0	-1	-2	-1	0	1	2
SOBEL	-2	0	2	-1	0	1	0	0	0	-1	0	1
	-1	0	1	0	1	2	1	2	1	-2	-1	0

Table 4-1: Soble filter in four main directions applied in this study

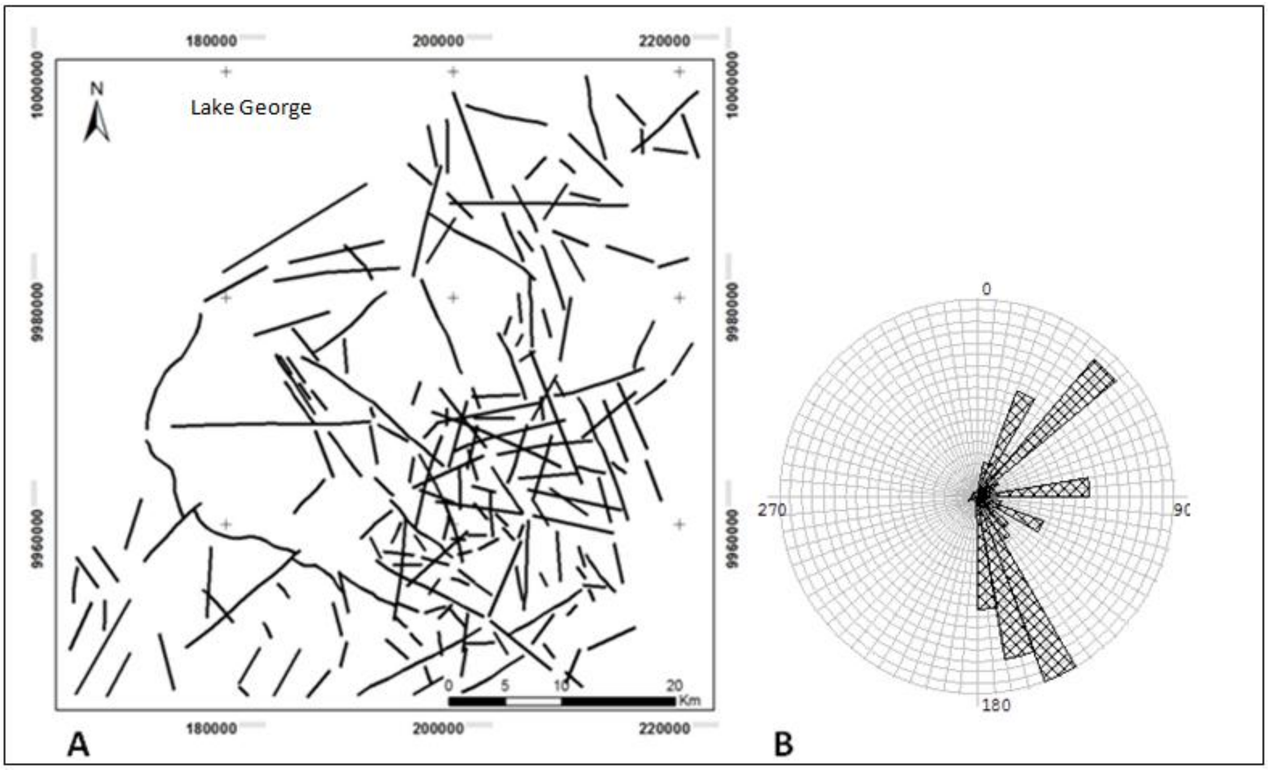

Figure 4-2: Interpreted lineament map A and Azimuthal distribution B

4.1.2. SRTM DEM interpretation

The SRTM DEM of the Buhweju area having a 33m resolution provided good topographic and structural information for use in lineament analysis. The extraction of lineaments from SRTM DEM in the Buhweju area involved three steps: (1) shaded relief images were produced, (2) shaded relief images were fused with multispectral data and (3) linear vector features were extracted from the processed images. Shaded relief images were produced (Figure 4-3) from eight different Azimuth directions namely N, NE, E, SE, S, SW, W and NW. These relief images were helpful for enhancing the size, height, and slope variations of a morphology. Different sun angles like 0^0, 15^0, 30^0 and 45^0 were tried to get more information among which 30^0 was finally selected for its better interpretability. Figure 4-3 shows the images produced by combining the different shaded relief images facing to the same direction. The shaded relief images with illumination directions N, NE, E were stacked and stretched to enhance E-W, N-S and NW-SE lineaments (Figure 4-3a). The other shaded relief image was produced by combining N, NW and W direction relief images to enhance E-W, N-S and NE-SW lineaments (Figure 4-3b.) These shaded relief composite images in general led to better interpretation of lineaments since they superimpose the information contained in various single shaded relief images.

Fused images were generated by multiplying the landsat ETM band5 with the eight shaded relief images produced before. Band5 was selected because of its better information on topography and boundary delineation as compared to other bands. From the multispectral datasets describe in (section 3.3) ETM741 color composite offered better delineation of lithologic units in comparison to lineament extraction. Good lineament interpretation however was possible when transformed to IHS and Intensity enhanced by the color shaded image (Figure 4-4).

The final interpreted lineament map (Figure 4-5a) was then produced with a total of about 248 lineaments extracted from SRTM DEM. The azmuthal distribution (Figure 4-5b) indicated that most of the lineaments are trending to NNW-SSE and NNE-SSW direction directions and distributed though out the Buhweju and Igara complexes.

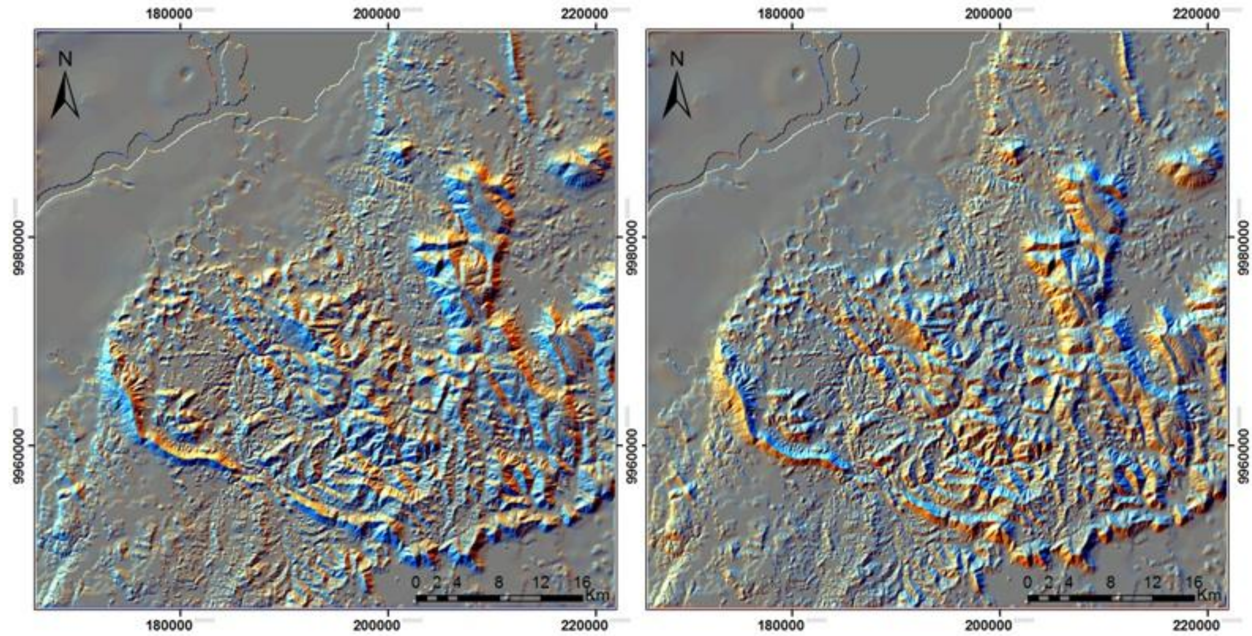

Figure 4-3: Color shaded relief images. A) Composite SRTM image with illumination directions of 45, 90, 360 B) Composite image of SRTM with an illumination directions of 270,315 and 360 degrees.

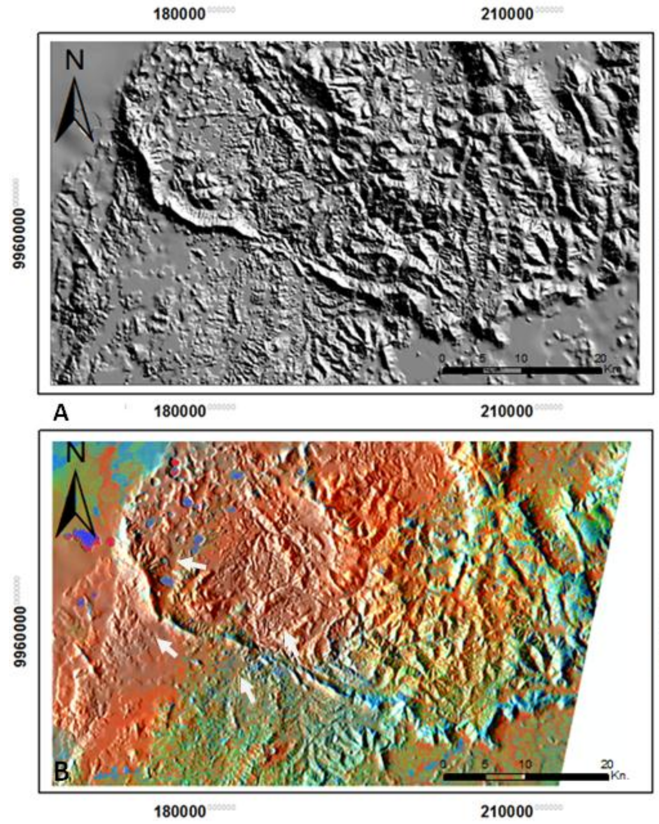

Figure 4-4 :SRTM DEM Subscens of the area A) SRTM DEM with illumination angle at 45^0 B) IHS image of Landsat ETM741 in RGB, Intensity modulated by SRTM DEM. White arrows indicate enhanced linear features trending in different directions.

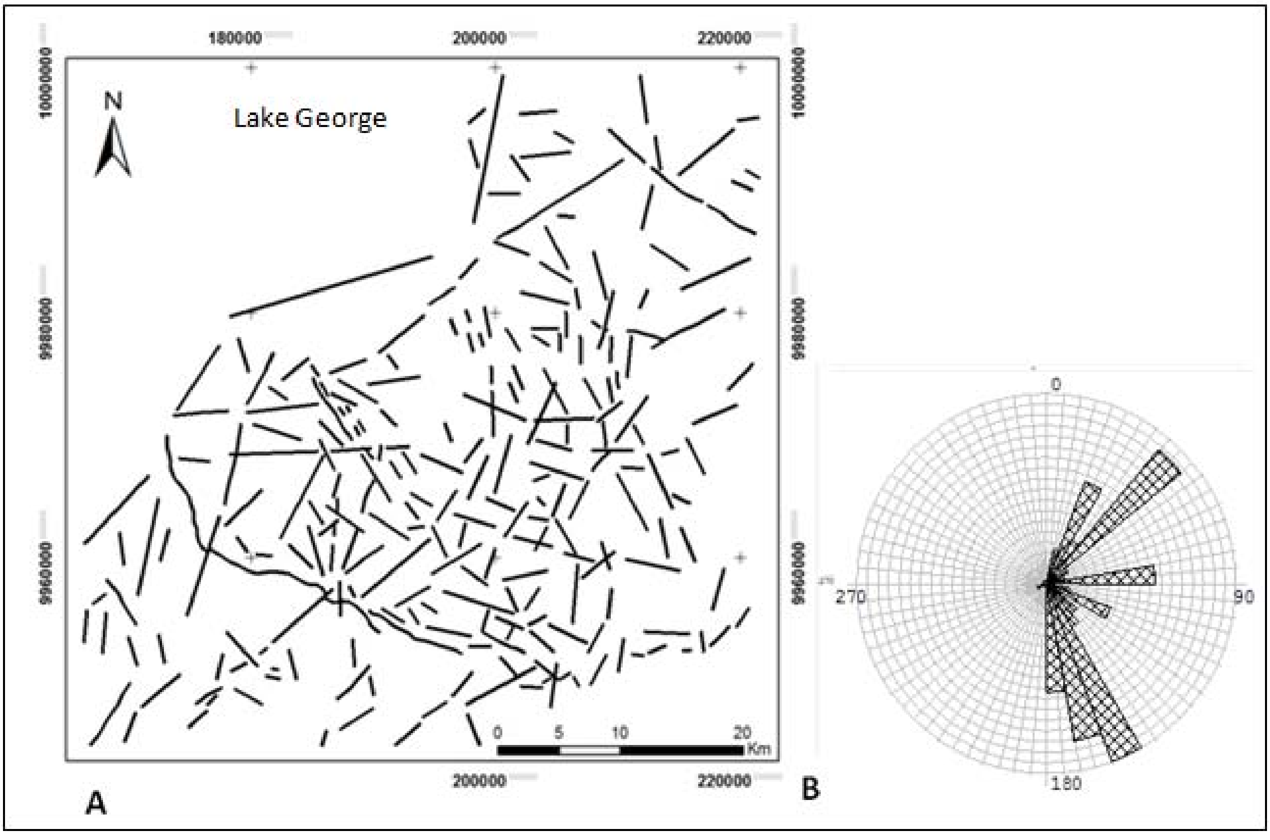

Figure 4-6: Interpreted lineament map A and Azimuthal distribution B

4.2. Summary

From the above sections it has observed that almost the same number of lineaments was extracted from both interpretations. However, there are lineaments which were identified in multispectral data but not in SRTM DEM and vice versa. Therefore, the final integrated lineament map of the area (Figure 4-7) was produced by synthesizing these preliminary interpretation maps. The following interpretations were generally made concerning the surface lineament of the area:

1. As clearly seen from the SRTM DEM, the central part of the area (Buhweju complex) has a remarkable elevation difference as compared to adjacent areas. This area is entirely covered with Precambrian Buhweju group rocks consisting of pelites and psammites intimately mixed with quartzite. The lineament interpretation has showed that the area is topographically complex, highly dissected and hence high lineament density (Figure 4-8) has observed.
2. The Lubare quartzite has showed a prominent emplacement bounding the southern part of Buhweju. This unit has also dissected by several strike slip faults of various (N-S, NNW-SSE and NE-SW directions.) throughout its length from west to east with alternating dextral and sinistral movements. The Lubare quartzite at the northern part however is dissected by lineaments with NW-SE and E-W orientations.
3. The western part of the study area partly constitutes eastern portion of the western rift valley and hence different NE-SW trending stepping normal faults are clearly observed crossing the recent rift volcanic and sediments.
4. The density lineament map was revealed that the Buhweju group rocks especially the Lubare quartzite was highly affected by high lineament concentration.
5. Two prominent lineament orientations are interpreted from the rose diagram. These are lineaments trending in about N10-50E and N0-40W both occurring mainly on the Buhweju complex and the former mainly attributed to the rift related faults.

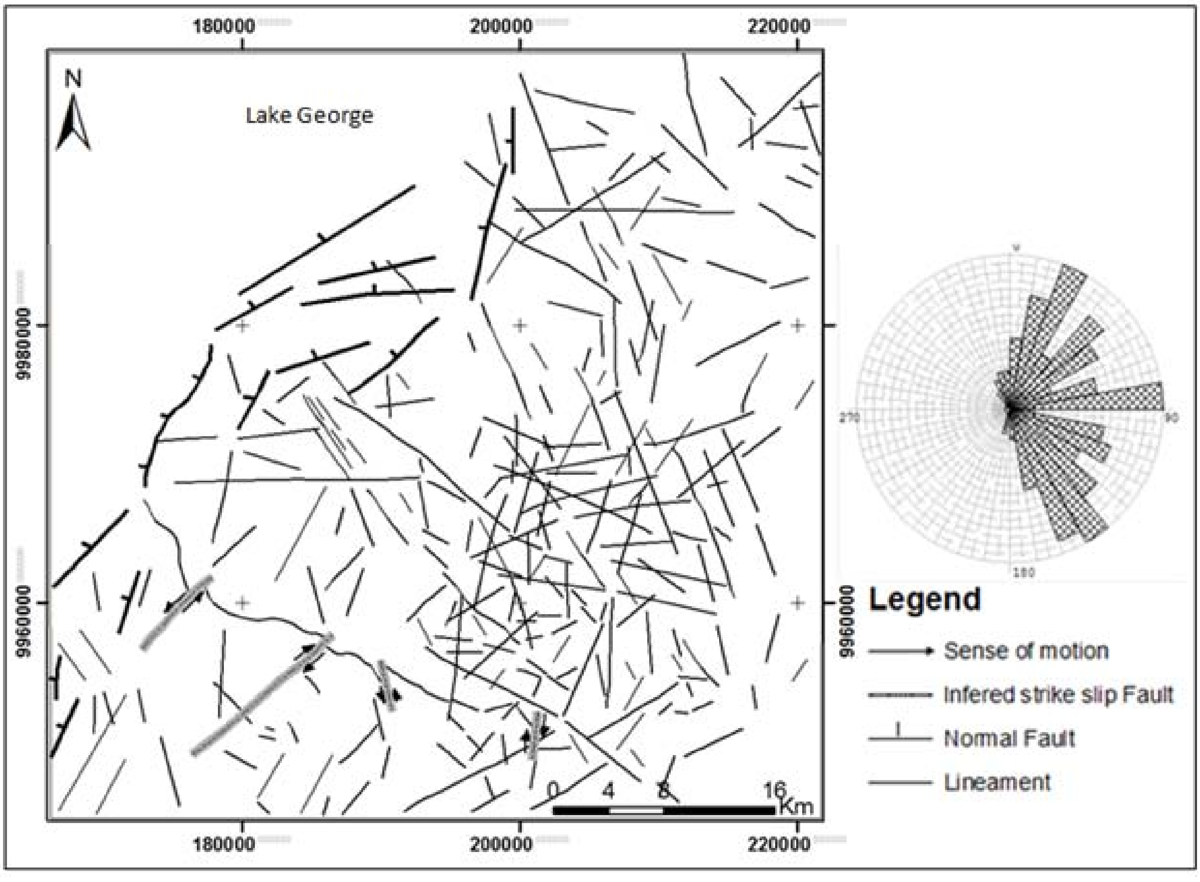

Figure 4-7: Final interpreted surface lineament map of the area

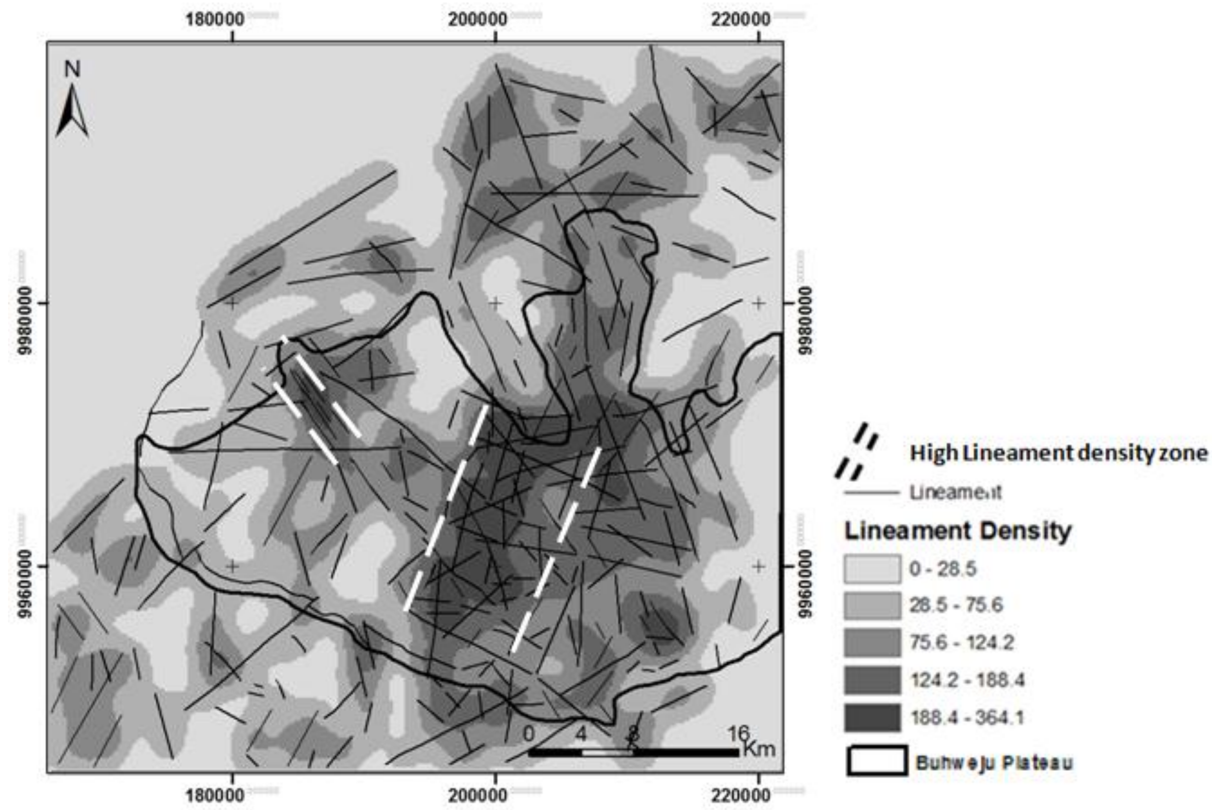

Figure 4-8: Lineament density map of the area

5. PROCESSING AND INTERPRETATION OF GAMMA RAY DATA

5.1. Introduction

Nowadays, gamma ray spectrometric data are becoming popular method for surface geological mapping and detection of alteration related to mineralization. Basically, the method measures the abundance of most common radioactive elements, Potassium, Thorium and Uranium for the top 0.30 m of the Earth's surface. Mapping the surface geology through interpretation of radioelement distribution relies on the assumption that rocks are composed of rock forming minerals containing specific amount of radioactive elements. In addition, the capability of surficial materials to retain significant and detectable compositional difference between lithologic units determines the efficiency of gamma ray for surface geology mapping (Dickson & Scott, 1997; Wilford, 2002). Various previous works have already been published on utilization of gamma ray data for regolith and surface geology mapping (Dickson & Scott, 1997; P. J. Gunn et al., 1997; Jayawardhana & Sheard, 2000; Johnson et al., 1979; Wilford, 2002; Wilford et al., 1997; ZHANG et al., 1998) and for identification of alterations related to mineralization (Jayawardhana & Sheard, 2000; Quadros et al., 2003; Ramadan et al., 2009; Shives et al., 2000).

There are several factors which affect the merit of gamma ray data for geological mapping including; vegetation cover, detectable contrast in radioelement between lithologic units, weathering and soil moisture. Despite of these controlling factors however,, gamma ray data has showed advantages over other remote sensing data set for mapping the surface lithology in vegetated and weathered areas (Perrotta et al., 2008). Gamma ray response from arid and unweathered terrain is directly related to mineralogy and geochemistry of bed rock. Hence, this good correlation usually makes interpretation less difficult. In tropical areas like Uganda, where vegetation, weathering and geomorphic processes are significant however, radiometric responses are usually a difficult combination of responses from various surface covers including fresh rock, weathered rock and transported materials (Dickson & Scott, 1997).

Weathering greatly affects the distribution and concentration of radioelement and hence understanding how radioelements behave during weathering would be crucial to make an interpretation (Wilford, 2002). The geochemical characteristics of weathered rocks are different as compared to the rocks from which they were derived. This is because the intensive weathering over a long time have leached and transported the soluble elements and have left behind the insoluble components (Butt et al., 2000). According to Dickson & Scott (1997), Gunn et al. (1997), Wilford, (2002) and Wilford et al. (1997) therefore, a general assumption could be drawn that in most rock types K concentration decreases with increasing degree of weathering (Figure 5-1a) which also works true for U and Th but in felsic rocks only. Weathering of intermediate, mafic and ultramafic rocks produce soils with relatively increased U and Th concentrations. This is because K leaches very easily due to its highly soluble nature whereas U and Th are mostly associated with resistant minerals and are scavenged by the weathering profile during weathering. The study by Wilford et al. (1997) has shown that, geomorphic activities can also play a significant role in radiometric signature. This implies that an actively eroding terrain reflects the bed rock response on radiometric data whereas stable terrains reflect regolith and weathering responses (Figure 5-1b).

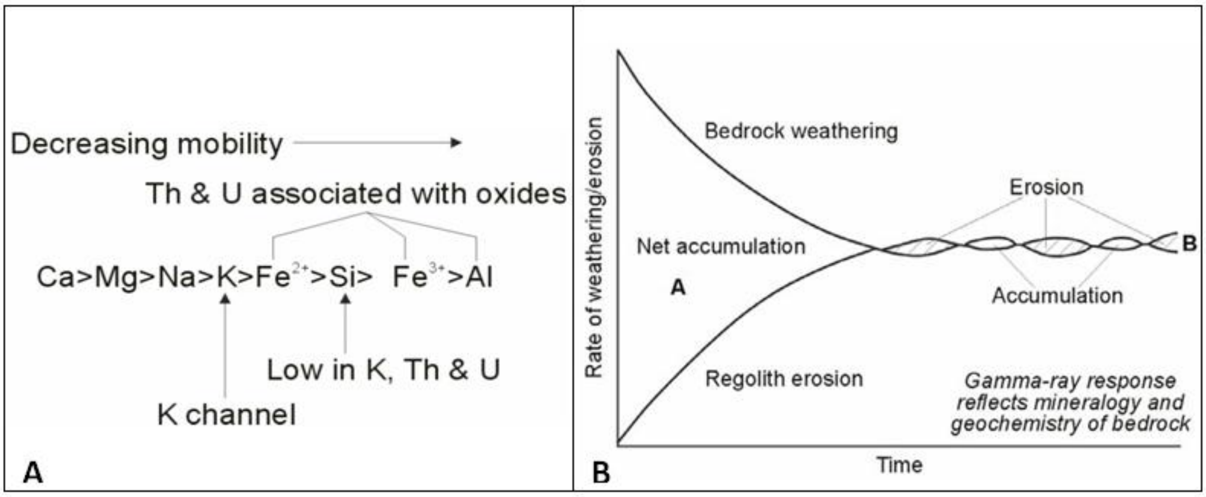

Figure 5-1: A) Element weathering and gamma ray response after (Wilford et al., 1997) B) Relationship between gamma ray response and denudation balance in landscapes(Wilford, 2002)

Many previous geological remote sensing studies have highly recommended and demonstrated that gamma ray data should be integrated with other remote sensing data for better knowledge of interpretation (Dickson & Scott, 1997; Perrotta et al., 2008; Wilford et al., 1997). The geomorphic activities and the corresponding gamma ray response will be well interpreted when integrated with topographic data (DEMs). In addition, integration of gamma ray data with satellite images of better spatial resolution have resulted better geological interpretation because the combined image enables the geochemical properties contained in gamma ray to be interpreted in terms of actual surface features (Dickson & Scott, 1997; Schetselaar et al., 2000; Schetselaar et al., 2008; Wilford et al., 1997).

5.2. Data processing

The gamma ray data didn't cover the whole of study area (Figure 1-2). The radiometric data of the area are stored in a data base (*.gdb) format in Oasis Montaj consisting of different raw and processed channels. In addition already processed K, Th, U and TC grids are provided. The processed K, Th, U and TC channels from the data base are then gridded by using bi-directional gridding method and converted into maps which show the distribution of each radioelement in the area. The grids are then further enhanced using histogram equalization to obtain better contrast in distribution of radioelement over the area. The final grid maps are projected to the same projection system with other data sets and exported to ArcMap for further analysis.
Fully processed gamma ray data can be represented in different ways including contours, profiles and grids. Because of the arising digital image processing techniques different ways of data representation have been discussed by developed (Nicolet & Edric-Krausz, 2003). As a result, representation of radiometric data in digital raster format which provide both color and spatial information has becoming popular. In this study the processed data are presented in raster grid formats as shown in (Figure 5-3).

To observe the range of concentration of each radioelement over the area and to calculate the correlation between the radioelements the following procedures were followed. First, a separate geo database was created for each element in Oasis Montaji which consists of latitude-X, longitude-Y and concentration-Z. Second these data were exported to xyz file for further statistical analysis. The approximate range of concentration of the radioelements in the area is 0.05-2.89 %, 0.1-40.5 ppm and 0.5-10 ppm for K, Th and U respectively. The correlation factor between the radioelements are also calculated and shown in the (Table 5-1) indicating that generally high correlation exists between Th and U.

	K (%)	eTh	eU
K (%)	1		
eTh	0.25	1	
eU	0.18	0.82	1

Table 5-1: Correlation between radioelements

The relation of each of the radiometric elements with topography is rather complex but generally showed that elevation is directly proportional to Th and U concentration and inversely related to K concentration. Statistical analysis was also carried out to depict the concentration of each radioelement per various lithological units of the area. The mean values of each radioelement concentrations per lithological units (Figure 5-2) suggested that it is possible to discriminate geological units based on their radiometric signature mainly of K and Th.

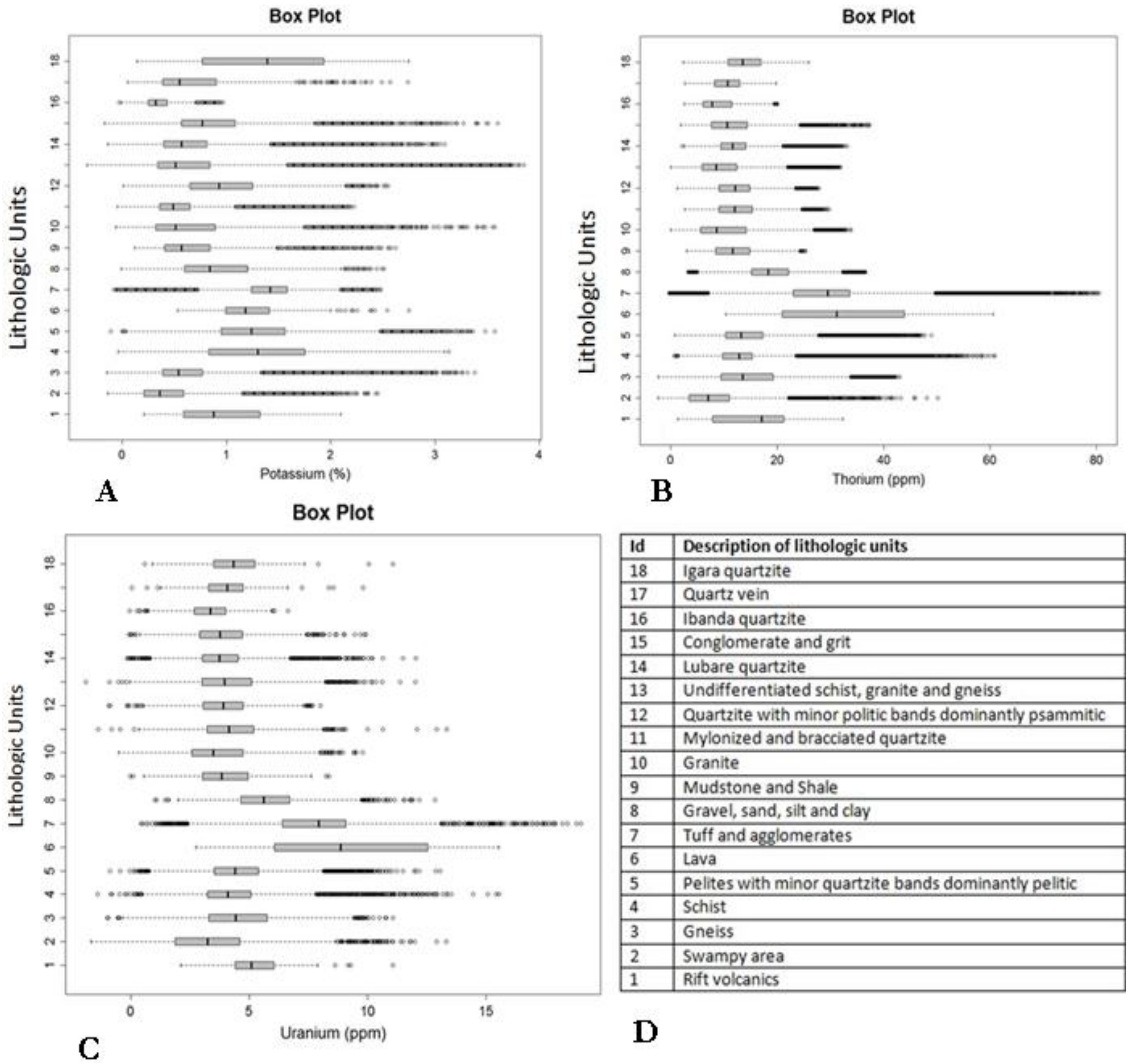

Id	Description of lithologic units
18	Igara quartzite
17	Quartz vein
16	Ibanda quartzite
15	Conglomerate and grit
14	Lubare quartzite
13	Undifferentiated schist, granite and gneiss
12	Quartzite with minor politic bands dominantly psammitic
11	Mylonized and bracciated quartzite
10	Granite
9	Mudstone and Shale
8	Gravel, sand, silt and clay
7	Tuff and agglomerates
6	Lava
5	Pelites with minor quartzite bands dominantly pelitic
4	Schist
3	Gneiss
2	Swampy area
1	Rift volcanics

Figure 5-2: Box plot showing the distribution of radioelement per litholohic units A) K-plot B) Th-plot C) U-plot D) Key to the numbers of mapped lithologic units in A, B and C

5.3. Image Enhancement and Interpretation

5.3.1. Image Enhancement

The radiometric data represented in digital raster format can be enhanced for visual inspection and can also be combined arithmetically with other data types forming color composite images and statistically analyzed for further applications. The processed gamma ray data of the Buhweju area was enhanced in various ways to increase interpretation for surface lithological mapping. The data is presented in different radiometric parameters including pseudo color single band image, color composite images and ratio images. Pseudo color single band images of K, eTh, and eU, element ratio maps and a ternary color composite image have provided good enhancements possibilities to discriminate different surface lithologies. The single band pseudo color images shows areas where a particular radioelement has relatively higher concentration which can be directly correlated with the geochemical properties of the surface lithology and regolith (Duval, 1983; Wilford et al., 1997). In addition the radiometric color composite images provide an overall pattern of radioelement distribution over the study area. Ratio images of the individual radioelement (Th/K, U/K and U/Th) have also resulted in better enhanced images (Figure 5-4) through maximizing the contrast between radioelemts and suppressing the various environmental factors such as vegetation, soil moisture and topography. Ratio image also enhances subtle features that are not apparent in the original images by deccorelating the highly correlated radioelement grids. Furthermore, K, Th and U composite images (Duval, 1983) were produced by combining for example K, K/Th and K/U in RGB representing K- composite image (Figure 5-8b). These composite images showed some enhancements for different surface lithologies and regolith.

Various integrated image enhancement techniques were also applied on the radiometric data by arithmetically combining with other types of data. The principle of mapping co-registered images on distinct perceptual attribute of human color vision using algebraic operation is the basis for digital processing methods used to generate integrated image enhancement (Schetselaar et al., 2008). The Landsat ETM band5 and band7 were merged with the radiometric grids (K, Th, and U) using HPF transform, a method proposed by Chavez et al. (1991) where both were co registered to the same 30m resolution grid cell size. The resultant enhanced image (Figure 5-5a and 5-5d) provided better interpretation possibilities by adding actual surface features (like lithological contacts and faults) to the radiometric information contained in the gamma ray data. To compute the red, green and blue channels of the color composite image, the following arithmetic expression was generally followed (Schetselaar et al., 2008):

$$red = \frac{1}{c}(a.K + b.TM\,5)$$

$$green = \frac{1}{c}(a.eTh + b.TM\,5)$$

$$blue = \frac{1}{c}(a.eU + b.TM\,5)$$

$$c = a + b$$

Where a, b and c are constants (a=1; b=2) used to weight the contrast between the landsat ETM band 5 and radioelement channels to increase or decrease the influence of one image with respect to the other. In addition, C should always be the sum of a and b to obtain values which are in the same range as the impute images.

Likewise, the radiometric data were also integrated with the STRM DEM data to add topographic information. After co registering to the same grid cell size, the SRTM DEM data was combined with the radiometric data basically by two different ways. The first approach involved the transformation of RGB radiometric composite image (ternary) into Intensity, Saturation and Hue (IHS) which is more intuitive for human color vision. Once RGB is transformed to IHS, there is a possibility to substitute the different channels by another data as required. The intensity image was substituted by the SRTM DEM and an inverse transformation of IHS image to RGB was carried as seen in the (figure 5-5b). The second approach involves pan-sharpening; the low (50m) resolutions radiometric data is fused with a high resolution (33m) STRM DEM (Figure 5-6c). In addition, the composite image (ternary) was enhanced by SRTM DEM with hill shading in different directions (Figure 5-6d) using Oasis montaj. This has resulted in a better enhanced image in comparison to the original ternary image. The IHS image obtained from the RGB ternary image was not good as such and not used for further interpretation and analysis.

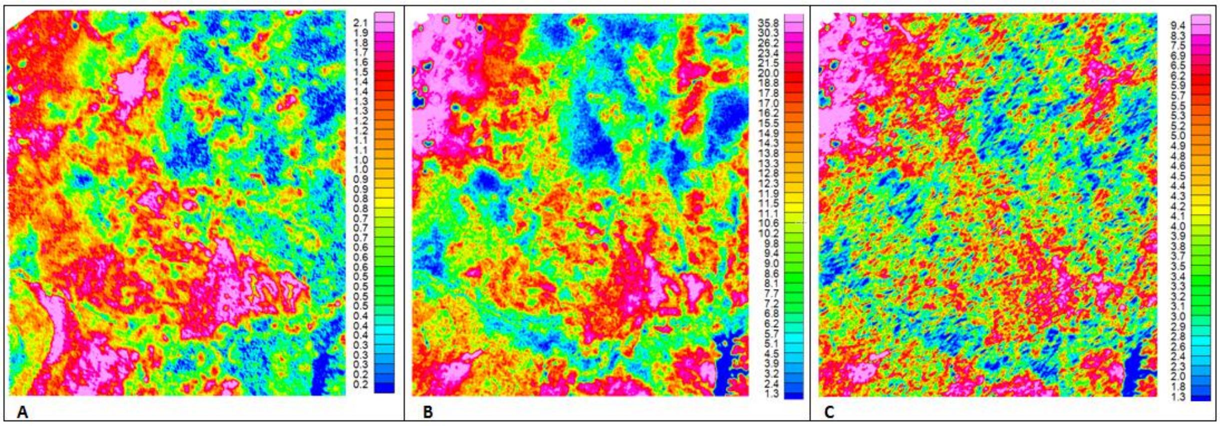

Figure 5-3: Images of individual radioelement grids A) K grid B) Th grid and C) Ugrid

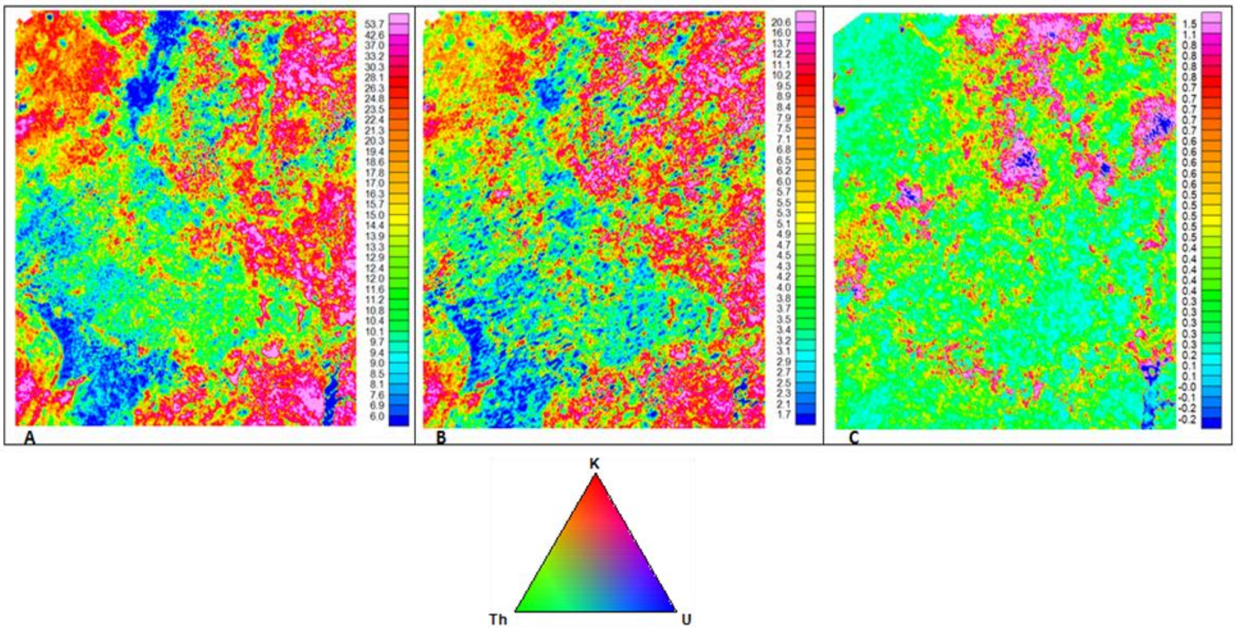

Figure 5-4: Images radioelement ratio grids A) Th/K map B) U/K map and C) U/Th map

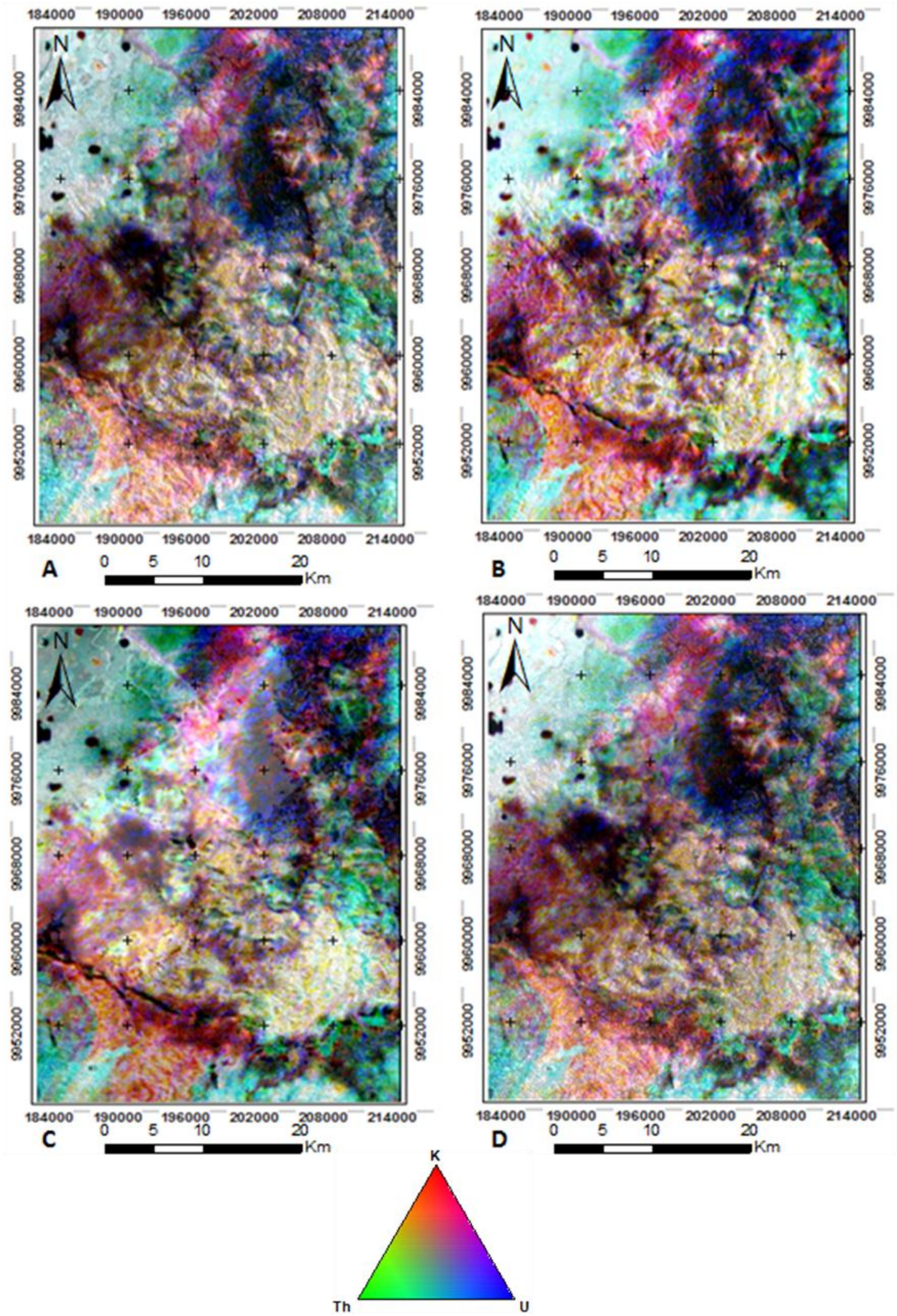

Figure 5-5: Various IHS composite images of gamma ray data, K, eTh, eU in RGB order **A**) The Intensity data is substituted by Landsat ETM5. In **B**) the Intensity is substituted by SRTM DEM in **C**) by PC1 image of ASTER VNIR-SWIR and in **D**) by Landsat ETM7

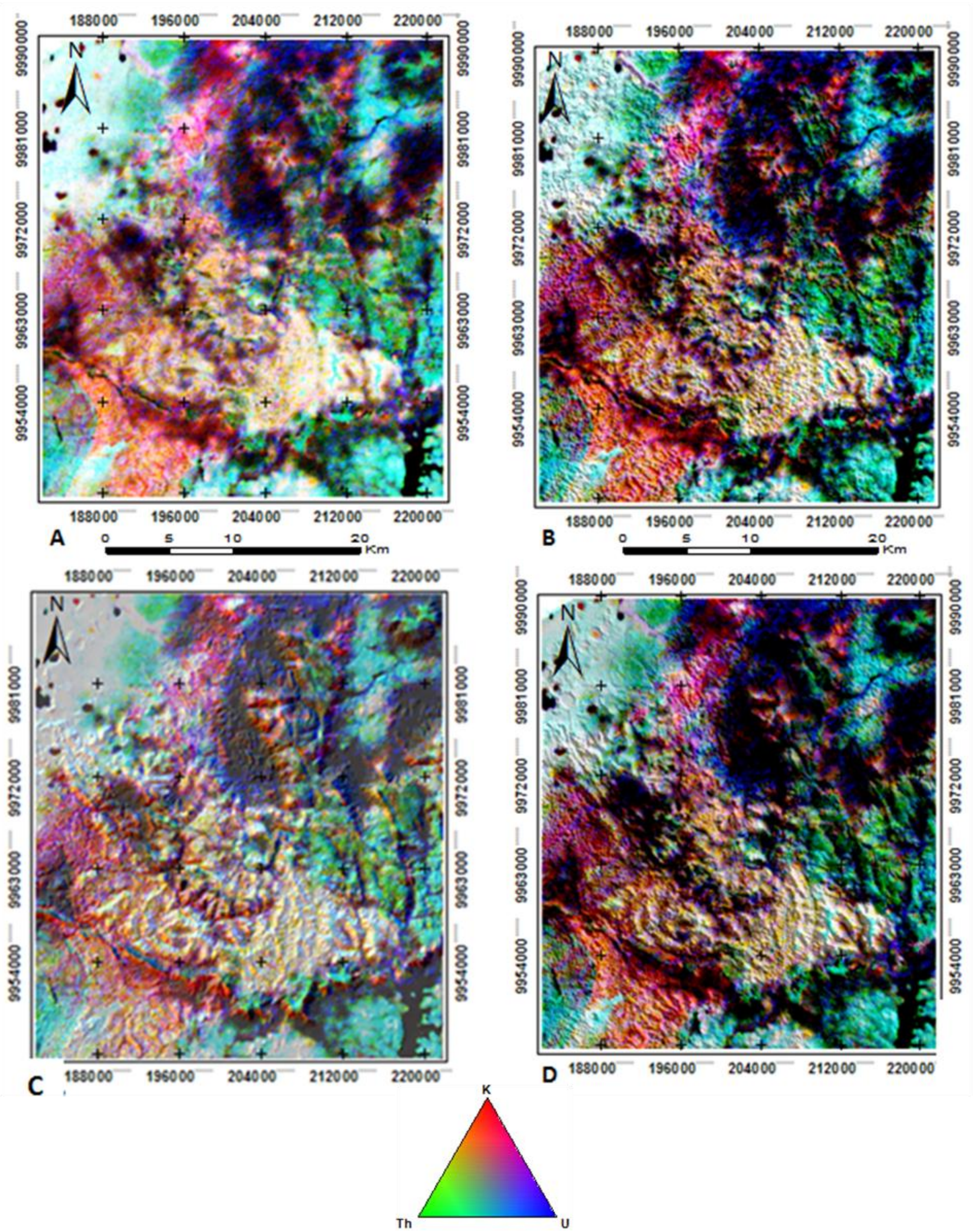

Figure 5-6: Different enhancements made on Ternary image **A**) Original ternary image KThU in RGB **B**) Ternary image modulated by shaded relief of total count **C**) Ternary image pan-sharpened by SRTM DEM **D**) Ternary image modulated by SRTM DEM with illumination from the 1st quadrant (45^0).

5.3.2. Interpretation

Qualitative photo geological interpretations were applied here similar to interpretations made in section 3 on multispectral images.. Lithological units were discriminated based on their Tonal/ color difference with blue colors representing low and red representing high concentration of a particular radioelement. The composite images including ternary one were used to display the distribution pattern of the three radioelements (K, eTh, eU) in red, green and blue respectively.

Close inspection was made on the enhanced images produced in section 5.3.1 in comparison with the previous geological map produced by (Reece, 1961). There was generally good agreement between the radiometric signature and the mapped lithologic units except mismatching of lithological boundaries. There are distinct lithologies which can easily be discerned from K and Th channel. These include: The Pleistocene tuffs and agglomerates located in the NW corner; the Precambrian units including pelitic schist in the SW; pelites with minor quartzite located in the central part and gneissic terrains in the SE part of the study area (Figure 5-7a). In addition, interesting radiometric distributions were obtained from the ratio images mainly Th/k and U/K from which Th and U enriched lithologies were clearly identified with respect to K concentration. The Precambrian lithologies covering the western part of the area (Figure 5-7b) including the undifferentiated granite, gneiss and schist, Quartzite and gneiss in the SE part have showed high concentration of Th and U while the pelitic schist, pelites (with minor quartzite) including some of the areas previously mapped (Reece, 1961) as undifferentiated unit showed low Th/K ratio value. As shown in the (Figure 5-7b) the undifferentiated granite, gneiss and schist mapped by (Reece, 1961) has showed high and low Th concentrations in the east and west of the Lubare quartzite respectively.

Interpretations were also made on the various enhanced composite images for example ternary (Figure 5-8a) and K-composite images (Figure 5-8b). Ternary image discriminate best between the different lithologic units of the area. The lubare quartzite, gneiss, pelitic schist and pelites (with minor quartzite) are clearly identified from the ternary image. The gneissic terrain at the southern part showed higher eTh and eU concentrations displaying cyan color on the image. The lubare and Ibanda quartzite are also discriminated from other lithologies by their elevated eTh concentration appearing green to bluish green on image. Pelites are clearly identified having white color which indicates higher concentration of K, eTh, and eU. This unit became reddish in color going from east to west which could be due to effect of vegetation that attenuates the penetration power of radiation from radioelements and hence decreases the concentration of eTh and eU. The boundary of this unit was clearly outlined also in K –composite image as shown in Figure 5-8b. The quartzite band dominated by psammitic units showed increased K as compared to other radioelement which could be related to the composition of psammitic units. The above interpretations made clear that the undifferentiated granite, gneiss and schist has apparently classified in to units having elevated K and eTh as shown in (Figure 5-8a and Figure 5-8b).

The fused and sharpened images (Figure 5-9a and Figure 5-9b) have confirmed most of the above interpretations extracted from the radiometric data. The intensity enhanced IHS image (Figure 5-9b) has provided clearer and sharp lithology contact and drainages with their radiometric information. The image also showed the effect of vegetation and topography on radioelement distribution of the area which suppressed the concentration of mainly eTh and eU. Lithological and other structural features are apparent and easily identified on the ternary image pan-sharpened by SRTM DEM. This image also revealed the distribution of radioelement with topography of Buhweju.

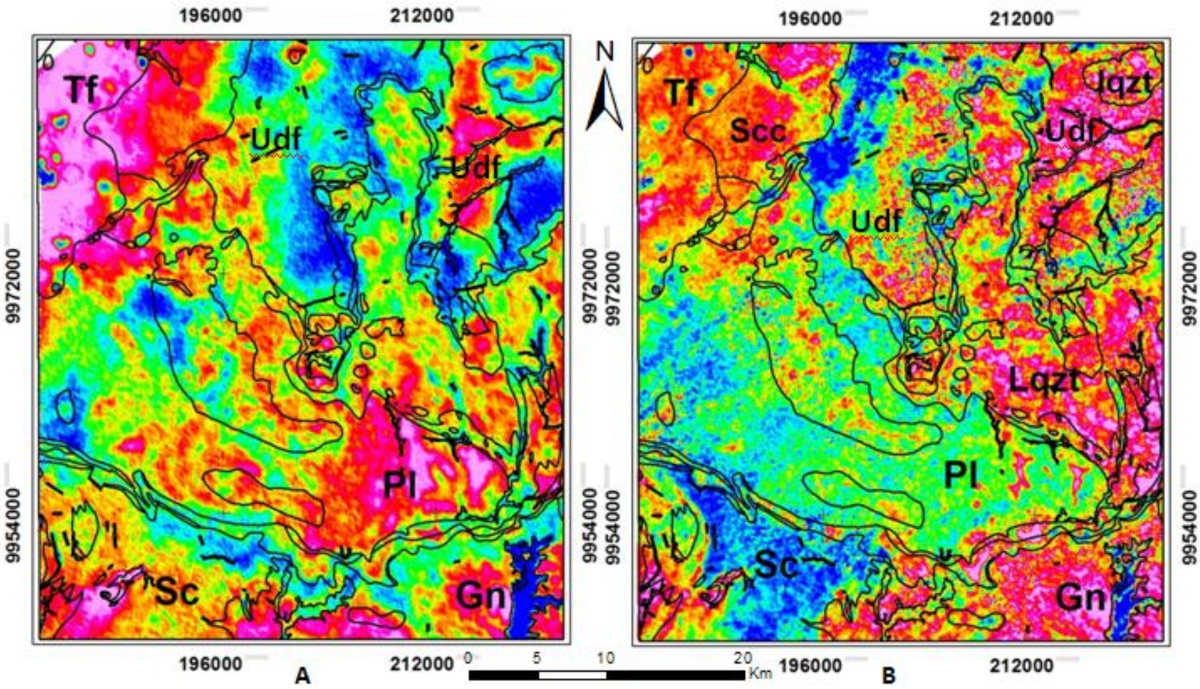

Figure 5-7: Previously mapped lithology overlaid on **A**) Th map and **B**) Th/K map Pl=Pelite with minor quartzite Gn= Gneiss Sc=Schist SCC=Sand, silt and clay Lqzt=Lubare quartzite Tf= Tuff and agglomerates Udf= Undifferentiated granite, gneiss and schist. Black lines represent lithologic boundaries by (Reece, 1961)

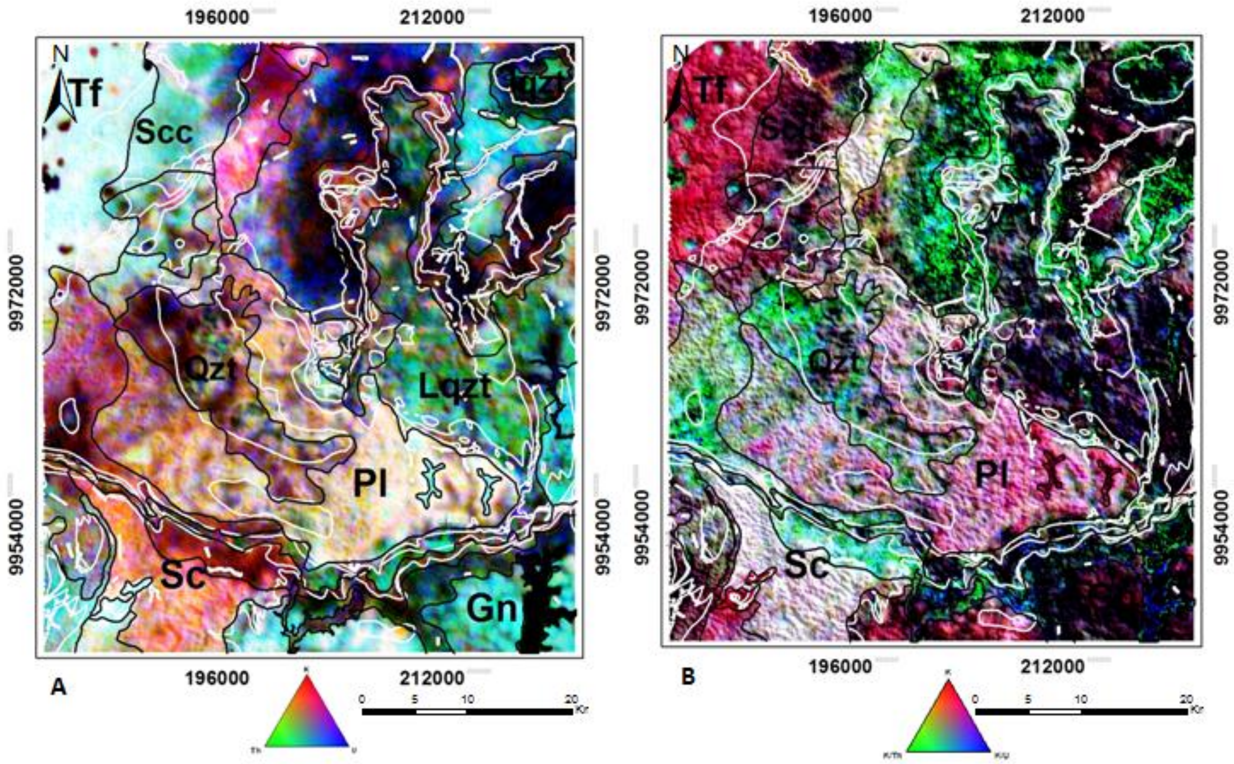

Figure 5-8: Lithological interpretations on gamma ray data **A**) Ternary Image **B**) K-composite image. White lines indicate previously mapped lithology boundaries by (Reece, 1961) and Black line represent interpreted lithology boundary. Gn=Gniess Sc=Schist Pl=Pelite with minor quartzite Lqzt=Lubare quartzite Scc= Silt,clay sand Tf=Tuff and agglomerates

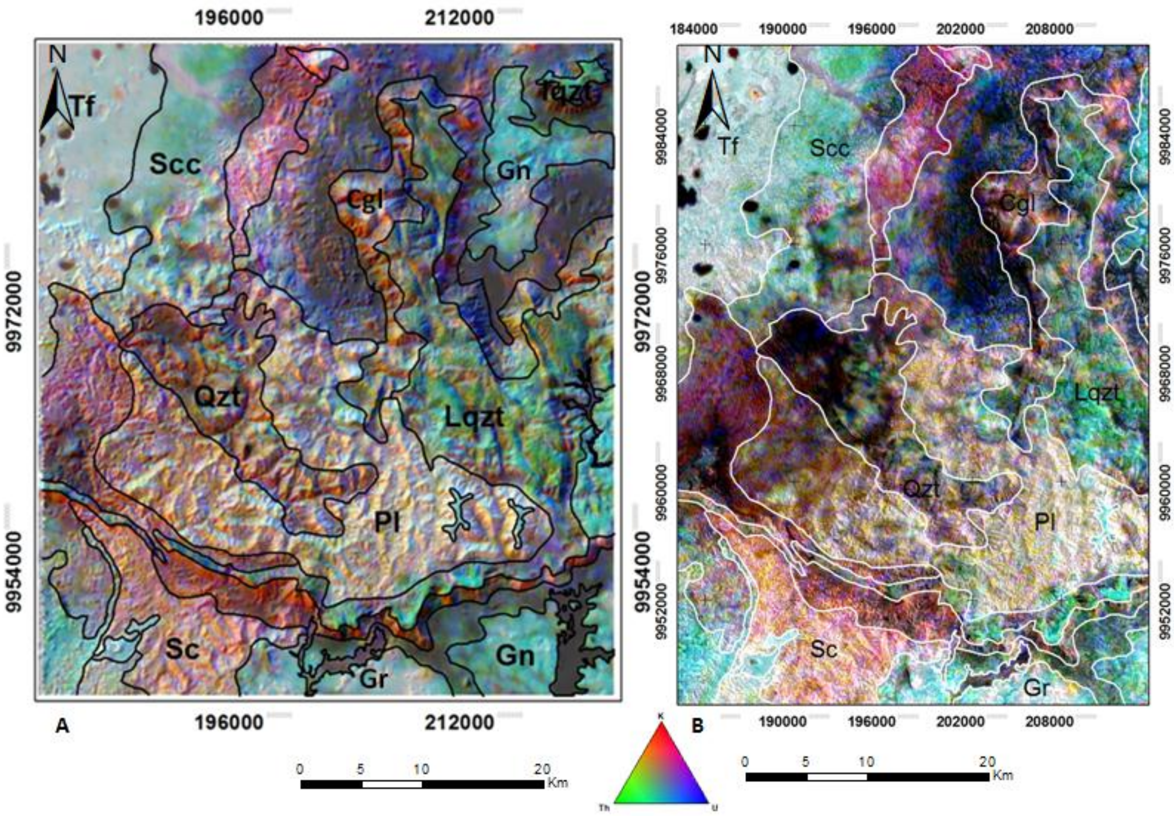

Figure 5-9:Interpreted lithologic units from radiometric data **A**) Ternary image pan sharpened by SRTM DEM **B**) IHS Composite image, Intensity enhanced by Landsat ETM5. Black and white lines represent interpreted lithology boundaries. Pl=Pelite Gn=Gniess Sc=Schist Lqzt=Lubare qaurtzite Qzt=Quartzite with minor pelite dominantly psammitic Scc= Sand,cilt,clay Tf=Tuff and agglomerates Gr=Granite Cgl=Conglomerates and grits

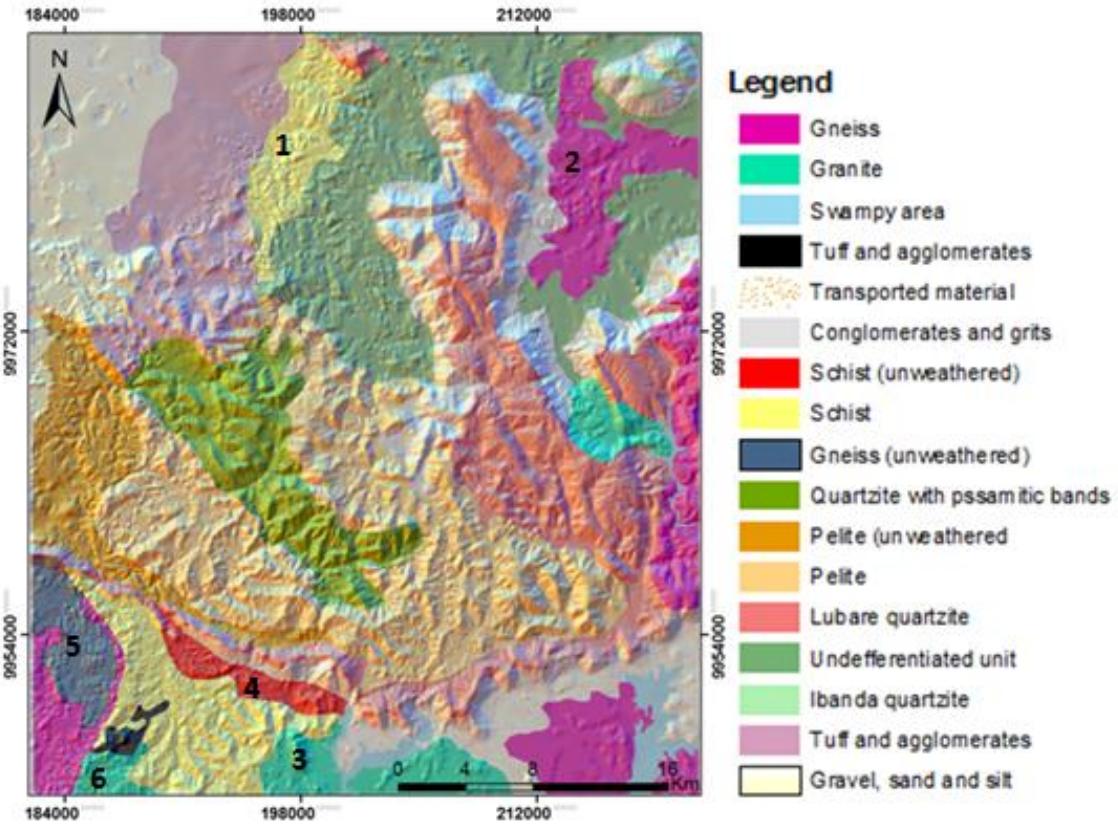

Figure 5-10: Interpreted lithological map. Numbers indicate the newly identified units

5.4. Summary of Radiometric data interpretation

Several image enhancement techniques were applied including single radioelement maps, ratio maps, image fusions and pan-sharpening of radioelement with multispectral and SRTM DEM data sets. Most of these enhancements have increased the interpretability of the radiometric data especially of the pan-sharpened and IHS transformed images.
Radiometric data generally found better in delineating and discriminating the different lithological units of the area. Most of the previously mapped lithological units (Reece, 1961) are in good agreement with the prevailing radioelement maps. The radiometric data interpretation revealed new lithologies which were not identified by Reece, (1961). These are schist and gneiss, identified from the previously mapped undifferentiated unit located in the northern part of the area, granite identified from the gneissic terrain in the SE of the area. The gneiss and pelitic schist in the SW have also showed variation in concentration of K which might be due to variation in degree of weathering throughout the unit. However, the names given for the newly identified units are entirely depending on their previous name by Reece, (1961). Finally, lithologies identified from analysis and interpretation of radiometric data is presented in the map (Figure 5-10) and their radiometric correlation is shown in (Appendix-2). The radiometric correlation for the newly identified units has only presented here in the table below.

New Interpreted units	Description and Radiometric signature
Schist -1	Compositionally rich in muscovite and biotite mica. Quartz is also common. Previously mapped as undifferentiated granite, gneiss and schist. Radiometric signature showed elevated K/Th value and very low Th/K ratio value. It appears dominantly red on enhanced ternary maps.
Schist -4	Compositionally the same with schist (1) and also mapped as schist by (Reece, 1961). An increased K concentration is observed on most radiometric images. It appears green in K composite images implying an increased K/Th ratio value.
Gneiss -2 and 5	Mainly composed of quartz and feldspar with occasional muscovite and mapped as undifferentiated granite, gneiss and schist by (Reece, 1961). Gneiss (2) has showed the same signature with other gneissic terrains in the SW corner (Figure 5-10) which appeared cyan due to enrichments in eTh and eU. Whereas in gneiss (5) depletion in Th and U was observed probably due to less weathering condition towards south.
Granite -3 and 6	Compositionally composed of quartz and feldspar with occasional muscovite. Granite (3) appeared dominantly white in ternary image due to higher concentration of radioelement. Granite (6) has mapped before as schist by (Reece,1961)

Table 5-2: Radiometric correlation of the newly identified units

6. PROCESSING AND INTERPRETATION OF AEROMAGNETIC DATA

6.1. Introduction

Aeromagnetic data has played a prominent role in earth science through revealing subsurface information. Aeromagnetic maps generally show the variation in the magnetic field of the earth and hence reflect the distribution of magnetic minerals in the Earth's crust. Mapping the variation of the crustal field, mainly due to susceptibility of crustal rocks, has greatly assisted in geological mapping and mineral prospecting specially in areas with limited outcrop (Allek & Hamoudi, 2008; Chernicoff et al., 2002; Ghazala, 1993; Jaques et al., 1997; Porwal et al., 2006; Schetselaar & Ryan, 2009). A publication by Grant, (1985) relate magnetic minerals with geology and mineralization. Areas where igneous and metamorphic rocks predominate generally show complex magnetic variations. Meanwhile in sedimentary regions, magnetic variations are small mainly reflecting basement lithology (Jaques et al., 1997). In areas like Buhweju, it is a challenge to fully establish the inter-relationship between lithology and structure due to complex tectonic history and several surficial factors as described in chapter 5. As a result, integrated interpretation approach was followed believing that subsurface activities could fully and /or partly manifested on the surface and so the relationship could be established. The aim of this chapter therefore is to process and interpret the aeromagnetic data acquired over the Buhweju area and perform a qualitative investigation of regional and local litho magnetic domains and subsurface structural setting of the area.

6.2. Data processing and Interpretation

6.2.1. Data processing

The aeromagnetic data didn't cover the whole of the study area (Figure 1-2) and the data was provided both in grid and data base format (*gdb) that contains different information layers including IGRF removed TMI and processed derivatives. Further processing related to image enhancement was performed by using OASIS Montaj data processing and analysis software. Wavelength, relative amplitudes, geometry and directions are basic characteristics of magnetic anomalies reflecting the respective orientation of magnetic sources, lateral extent and relative magnetic susceptibility (Porwal et al., 2006). Magnetic maps are most often dominated by large amplitude shallow depth anomalies which obscure subtle and deep seated anomalies (Alsaud, 2008). In the last few years, a number of methods have been proposed to normalize the signatures of the magnetic images in order to amplify subtle variations relative to stronger and large amplitude anomalies. Some of the normalized derivatives applied for this study include: reduced to pole of Total Magnetic Intensity (TMI), vertical derivative, analytical signal, tilt derivative and horizontal gradient. The basic principle behind each method and the resultant magnetic images are discussed in more detail in later section.

Even though various researches and publications were made using aeromagnetic data, interpretation methodologies applied to aeromagnetic data are still ambiguous and largely based on individual approaches and experience. In this study qualitative interpretation of aeromagnetic data was carried out, by which geological information was inferred by visual inspection on images. Some of the previous works on interpreting aeromagnetic data consulted in this study include those of (Alsaud, 2008; Jaques et al., 1997; Porwal et al., 2006; Schetselaar & Ryan, 2009).

Analysis of the aeromagnetic data involves close observation at the various layers of information achieved from the original data profiles. These include analytical signal (AS), reduced to pole (RTP) of total magnetic intensity (TMI), tilt derivative, vertical derivatives and horizontal gradient. Magnetic anomalies usually have complex shape due to the variation of Earth's magnetic field at point of measurement. The basic approach used to resolve this complex anomaly shape is reduction of the total magnetic field to the pole. RTP positions the anomaly directly above the source and hence makes interpretation easier. For this reason, other layers of information are derived from the RTP of total magnetic intensity (TMI) grid. The enhanced RTP image of the area (Figure 6-1a) showed the magnetic field amplitude of about 110.4nT indicating the variation of the magnetic intensity due to either lithological or topographical changes. Analytical signal was calculated for the area (Figure 6-1b**)** which positions the anomaly at the centre of the causative body by combining both vertical and horizontal derivatives. Analytical signal is considered better enhancement technique since dipolar effects are absent and even for small bodies the peaks merge resulting an anomaly cantered above the causative body (Alsaud, 2008). It is also observed that the vertical derivative applied to the analytical signal has sharpened up and positioned the anomaly more exactly than the original AS image. The tilt derivative (Figure 6-1c) applied to the RTP data has also provided better information by positioning the anomalies above the causative body like RTP and analytical signal. Horizontal gradient image was calculated from the RTP and upward continuations were performed at various depths to depict deep seated anomalies and magnetic contacts. Upward continued to 1km was selected for further interpretation as shown in (Figure 6-1d). The tilt derivative accentuates short wave length anomalies and was found to be effective in allowing anomalies to be traced along their strike (Alsaud, 2008). Both first and second vertical derivative images (Figure 6-2) were found better for delineation of shallow surface magnetic structures. Various angles of illuminations were applied on AS, RTP and tilt derivatives to produce shaded relief images which emphasized different sets of structures. In addition, several ratio and composite images (e.g. RTP/AS, RTP/VD1, and VD1/AS) were used to constrain interpretations.

6.2.2. Interpretation

6.2.2.1. Interpretation of litho-magnetic domains

The first step considered during the interpretation of crustal domains from aeromagnetic data is to understand the characteristics of magnetic anomalies such as: direction, relative amplitude and wave length (Porwal et al., 2006). With the help of the RTP image therefore, three different litho magnetic domains which constitute areas of the same magnetic signature as shown in the (Figure 6-1a) were defined**.** These interpreted litho magnetic domains show good correlation and are complementary to the regional stratigraphic units previously studied by (Reece, 1961). The Precambrian basement rocks of Igara group occupying the southern and eastern part of Buhweju is characterized by regional magnetic high with high amplitude and relatively shorter wavelength and hence grouped as Domain I. The Precambrian sedimentary rocks occupying the central and northern part of the area show lower magnetic anomalies with smoother, broader and longer wave length indicating deeper basement and then grouped as Domain II. Domain III occupied both Precambrian sediment and Pleistocene rocks generally with very low magnetic response which might be due thick rift sediment and westward deepening of the Precambrian sediments of the Buhweju group. The RTP image generally showed deep source magnetic anomalies by attenuating near surface anomalies as compared to other data layers.

Analytical signal has clearly showed both deep and shallow source magnetic anomaly areas (Figure 6-1b). In addition analysis of analytical signal revealed the existence of various bounding bodies (anomaly peaks) along which their contact was drawn along the strike. Anomalies with high magnitude, closely spaced and shorter wave length were also observed at the south covered by pelitic schist and gneissic terrain, NE corner covered by undifferentiated gneiss and granite and NW corner covered by Pleistocene volcanic and sediments. Furthermore, two prominent dykes with NNW trend were interpreted from the analytical signal. In tilt derivative most of the lithological units were underlain by closely spaced, sharp and short wavelength near surface anomalies. Lithological contact between pelite and the underlying schist and gneissic terrain was observed due to change in nature of magnetic anomalies (Figure 6-1c). In addition anomalies in the area were easily traced along their strike. The horizontal gradient (HG) image of the area has showed the dominant magnetic nature and orientation of magnetic anomaly beneath Buhweju area. This image has amplified mainly of deep seated anomalies and hence anomalies underneath the

Precambrian basement, pelite and psamitic rocks were dominantly observed together with their dominant orientation (Figure 6-1d). Finally, high magnetic zones were extracted from interpretations made on the above layers as presented in the figure 6.3b.

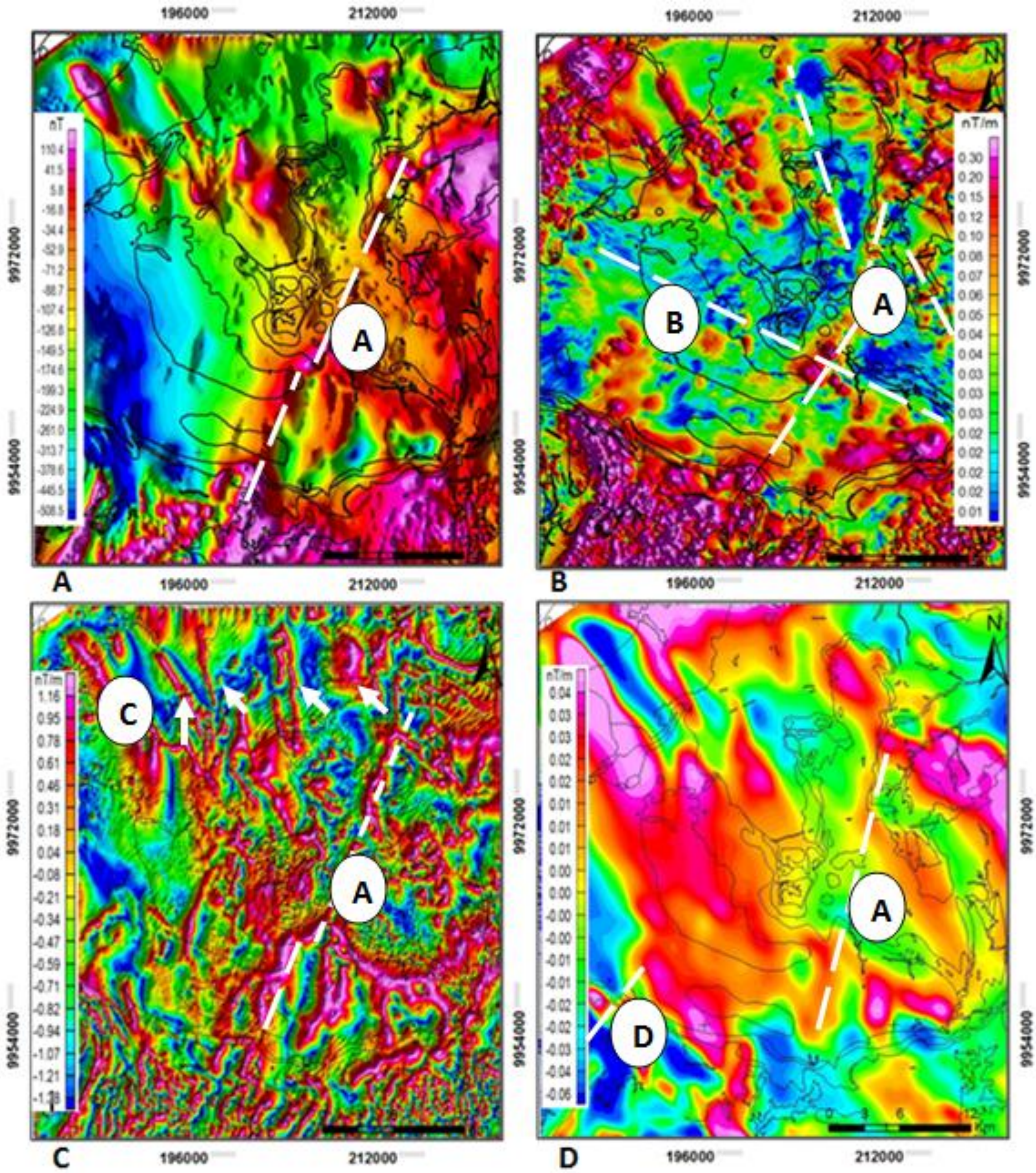

Figure 6-1: Enhanced Aeromagnetic images of the area A) Reduced to the pole (RTP) of TMI B) Analytical signal B) C) Tilt Derivative D) Horizontal gradient upward continued to 1km Black lines: Lithology boundaries Letters indicate identified magnetic faults. For detail see text.

Directions of anomalies mainly depend on orientation of magnetic sources which in turn could be tectonically controlled. Analytical signal, upward continued horizontal gradients and tilt derivative were found particularly valuable in amplifying orientations of magnetic anomalies. These anomaly orientations were then extracted and analysed separately (Figure 6-3) to decipher the tectonic grain of the area. Accordingly statistical analysis was carried out to determine the azimuthal distribution and result showed that the major magnetic anomalies are mostly trending in two prominent directions. These are N0-40 W and N0-50E as shown in the figure 6-3b.

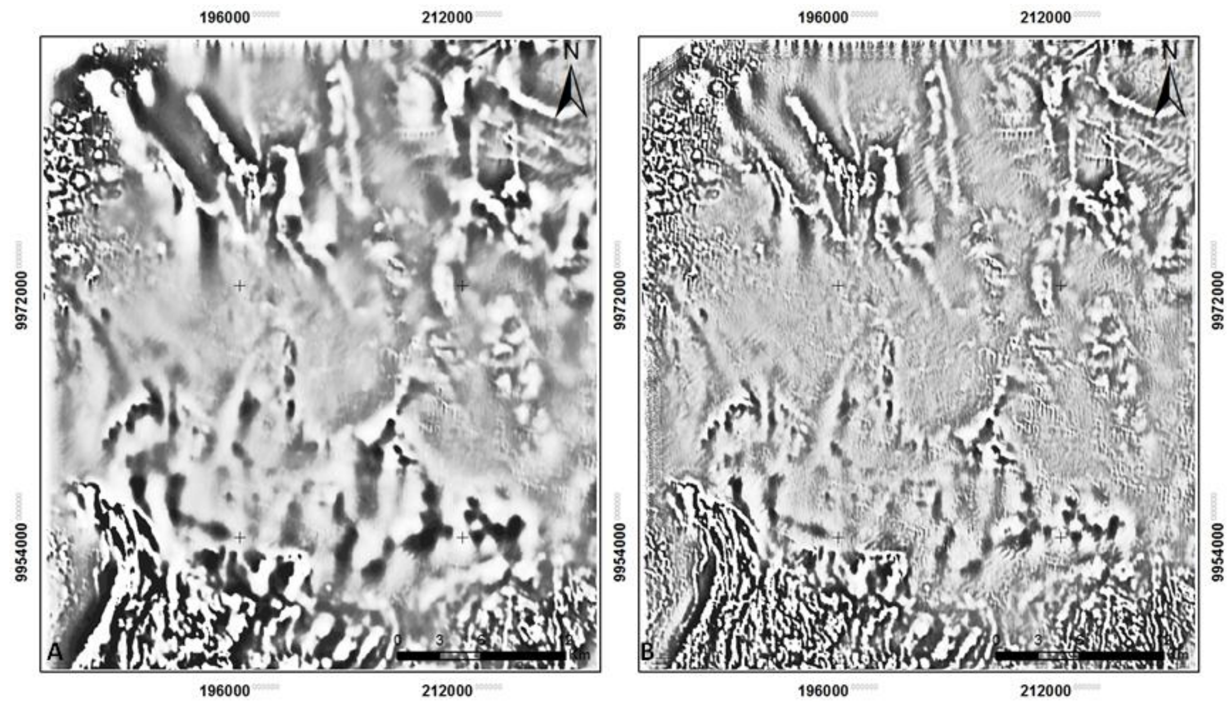

Figure 6-2: Vertical derivative images calculated from RTP A) First vertical derivative B) Second vertical derivative

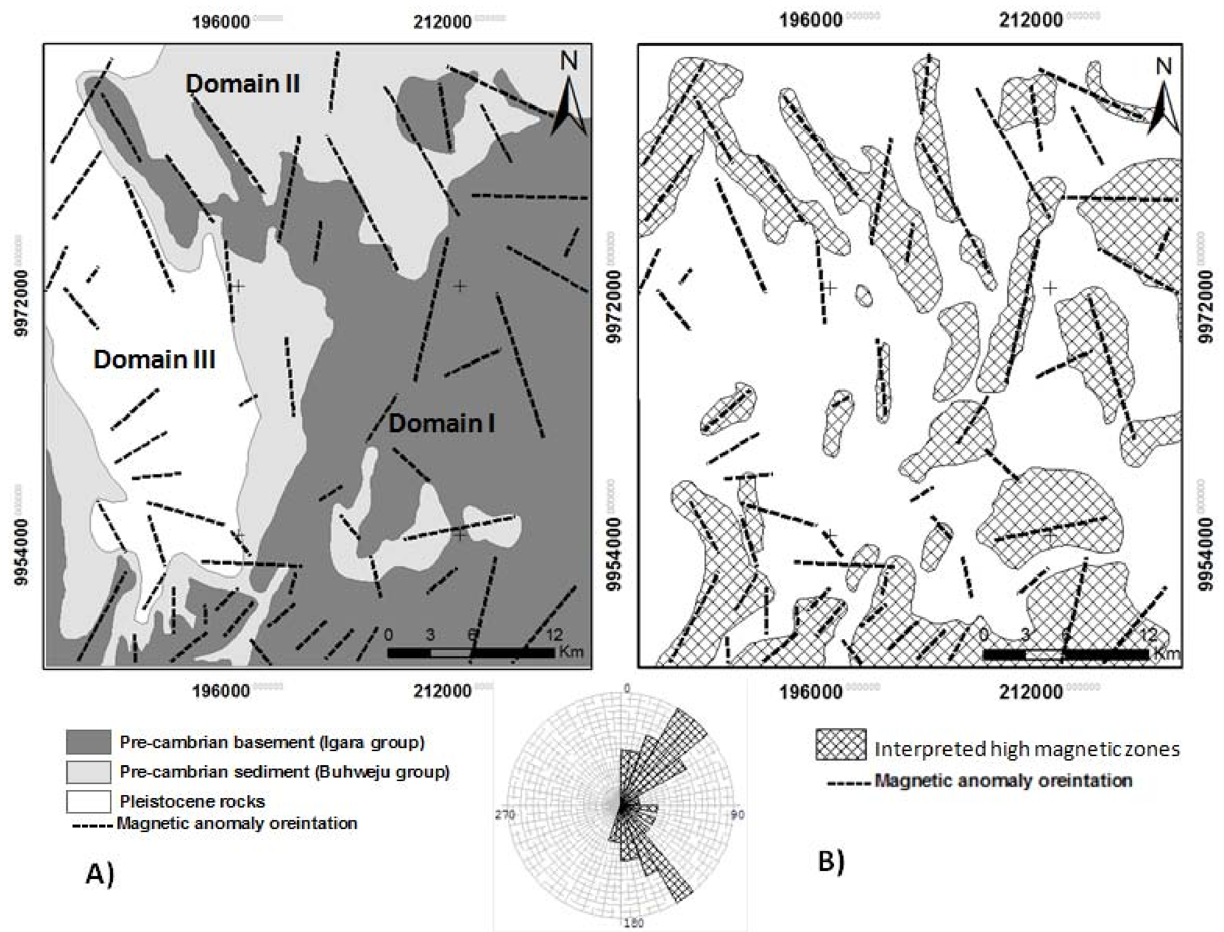

Figure 6-3: A) Regional litho-magnetic domains interpreted from RTP. B) High magnetic anomaly zones. Rose diagram shows the azimuthal distribution of orientation of magnetic

6.2.2.2. Interpretation of Magnetic lineaments

An overview by Gay, (1972) and Gunn et al. (1997) on the various criteria used for identifying magnetic lineaments is used in this study. Some of these criterions which were used in this study are: offset of apparently similar magnetic units, abrupt change in linear gradient, linear narrow magnetic highs and lows. Lineament interpretations were carried on the various layers of enhanced images among which large number of lineaments were identified from shaded relief of Tilt derivative image. Magnetic faults mainly due to offset of similar magnetic gradients were identified from tilt, RTP and upward continued Horizontal gradient (HD) images. A very prominent fault with high magnetic signature was identified from all the data layers as shown in letter in (Figure 6-1). Very discernible magndeitc lineaments were identified from different illumination directions applied in tilt derivative image (Figure 6-1c). Likewise other magnetic lineaments were extracted through close inspection of various layers of enhanced images. In the southern part of the area where schist and granitic gneiss predominate, short wavelength curvilinear magnetic anomalies are evident on tilt and first vertical derivative images. These magnetic anomalies are digitized and generally define rock foliation patterns. The structural framework of the area as interpreted from the magnetic data (Figure 6-1 and 6-2) is shown in the (Figure 6-4). Three main groups of lineaments were identified from this analysis based on their azimuthal frequency. Group of lineaments trending N0-60E form the most conspicuous in terms of lineament frequency and corresponds to Pleistocene rift structures. Most of these magnetic lineaments were seemed affect the Buhweju group rocks and found less dominant in the Precambrian basement rocks. The other dominant group of magnetic lineament have a trend of N0-60W which underneath most of the lithological units of the area. The dominant orientation of magnetic anomaly of the area (section 6.2.2.1) appears to be consistent with such trending structures. In addition these structures could conduit different subsurface dykes found in the area. The N60-120E trend magnetic lineaments were also common in terms of both frequency and length. These lineaments have mainly affected the undifferentiated units found in the northern part of the area as also shown in the lineament density map (Figure 6-5). The lineament density map has also revealed high lineament concentration in the central part of Lubare quartzite.

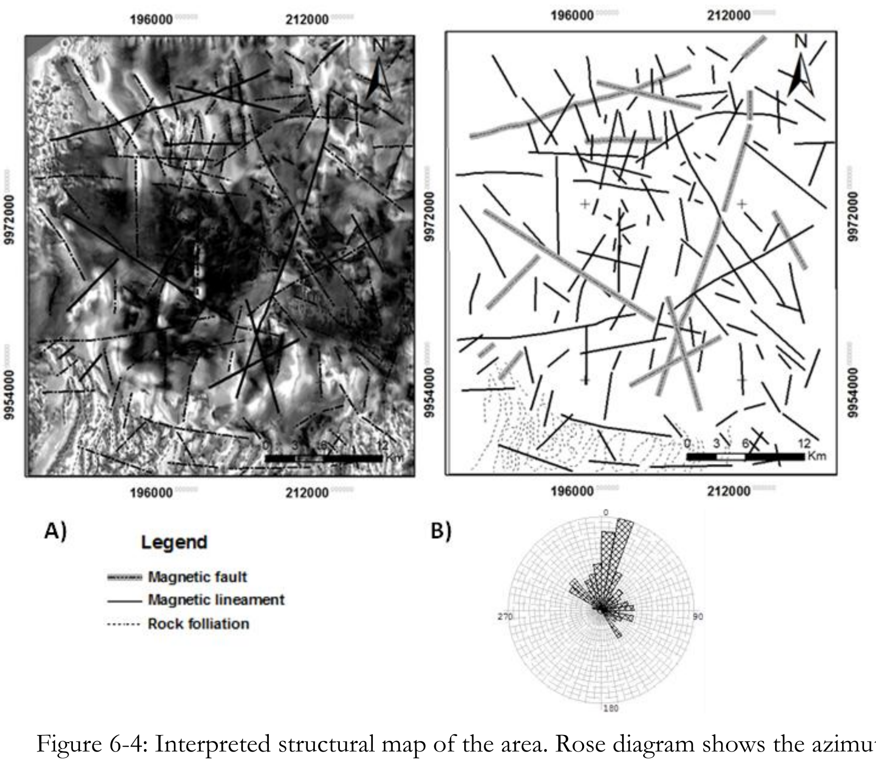

Figure 6-4: Interpreted structural map of the area. Rose diagram shows the azimuthal distribution of the magnetic lineaments.

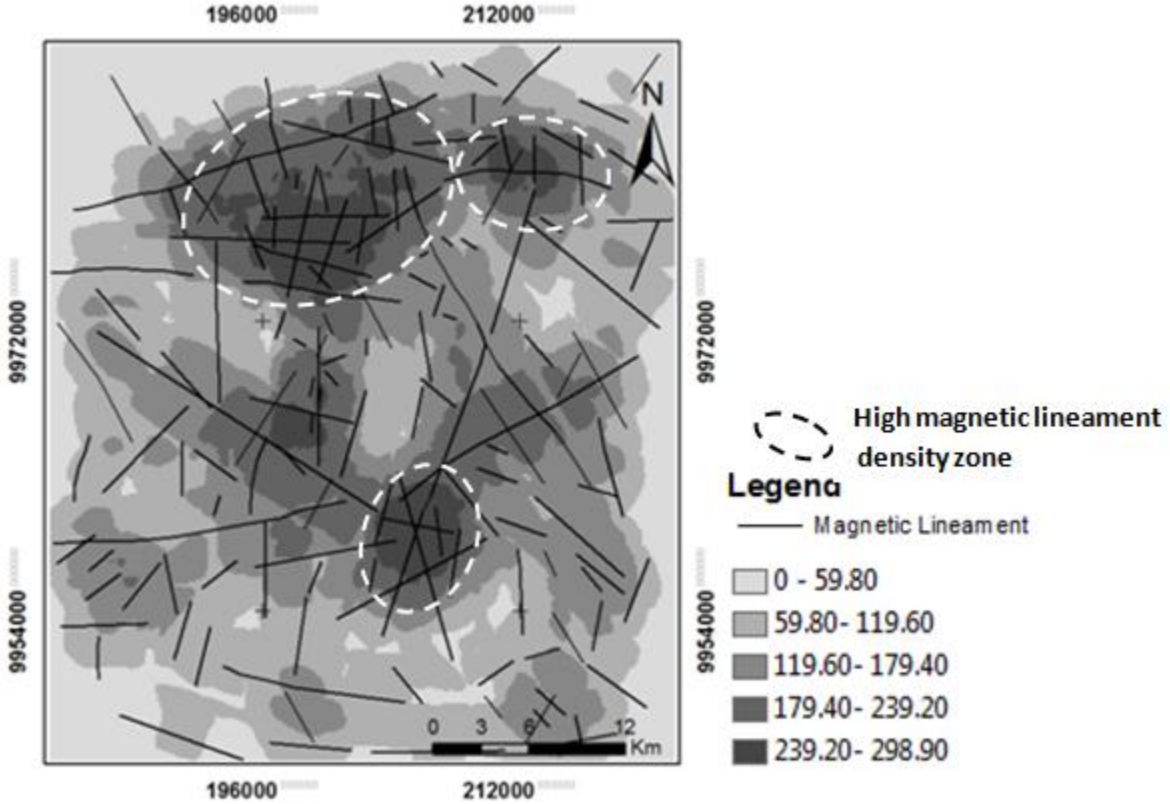

Figure 6-5: Magnetic lineament density map

6.3. Summary on aeromagnetic data interpretation

The interpretation made on the aeromagnetic data of the area has resulted in extraction of valuable information regarding lithology and tectonics of the Buhweju area. The presence of relatively good outcrops of the Precambrian Igara group rocks placed at eastern and southern part could be the reason for shallow depth anomalies observed on RTP image. The central part of the area which is mainly covered by Precambrian sedimentary rocks of the Buhweju group, revealed deeper source magnetic anomalies as compared to other groups. The orientations of possible magnetic highs (section 6.3.2.1) revealed the prevailing structural pattern of the area and are in good agreement with the orientation of the various identified magnetic lineaments. Prominent magnetic faults mainly due to offset of apparently similar magnetic domains are interpreted in addition to other magnetic lineaments identified in the area. It is observed that these fault patterns act as a conduit for emplacement of both rounded and elongated high magnetic intrusions at shallower and deeper sources. Particularly, the NNE trending fault persists throughout the area highly affecting pelites and psammitic bands and dominantly underlain by high magnetic bodies. Generally, three prominent structural patterns were discussed from the orientation analysis made for all magnetic lineaments extracted from the area. These are: N-NNW, ESE-WNW and N-NNE structural patterns in which the first two patterns could be interpreted in relation with the Precambrian orogenic folds and shear zones whereas the third pattern corresponds to the western rift valley.

7. DATA INTEGRATION AND GEOLOGICAL MAP COMPILATION

7.1. Introduction

This chapter deals with compilation of various interpretations of geological features acquired from different single and integrated images to create a modified geological map of Buhweju area. Compilation involves the synthesis of results obtained from the analysis, integration and interpretation of different geo-data sets. The different data sets used in this study are: aeromagnetic data, radiometric data, multispectral data (Landsat ETM+ and ASTER) and SRTM DEM data. The final interpreted units and lineaments of the area are based on synthesis of interpretations of lithology boundaries and lineaments obtained from (1) RGB images of ASTER and Landsat ETM data and principal component images (chapter 3 and 4). (2) Single band, ratio and composite images including ternary derived from radiometric K, eTh, eU and its fused images with Landsat Band 5 and SRTM DEM (chapter 5). (3) Various derived images from aeromagnetic data especially of RTP of total magnetic intensity (TMI), analytical signal, tilt derivative, 1st and 2nd order vertical derivatives and horizontal gradient image (chapter 6). The interpretations were mainly guided by lithological units from the published geological map by Reece, (1961) and field data.

7.2. Lithological boundaries

Different lithological units are identified from the previous published geological map. The boundaries of these lithological units could also be recognized from the various enhanced images but with different boundary shapes. This implies that there exist good agreement between the published map and interpretations acquired from different remote sensing data used in the study. However, there are lithological units which have not been identified before but identified and mapped in this study. The different interpretations are then combined to compile a modified geological map of Buhweju. During compilation analyzing the geological significance and accuracy of different images together with field knowledge of the area were considered to resolve the conflict between polygons resulted from interpretation of different data sets. This will be discussed in more detail for each interpreted boundary in latter sections. Geological maps are used for recognition of lithologies and hence the names of lithologies as used in the map of (Reece, 1961) are adopted. The relative age of lithologies is adopted from the previous maps and discussed in section 2. Here the discussion on major lithological units is presented with more emphasis given to the newly identified units. The improved geological map is shown in (Figure 7-4) with a classification accuracy of 56.34% (Appendix 3)

7.2.1. Undifferentiated gneiss, granite and schist

Reece (1961) has mapped this unit in the northern part of Buhweju covering relatively of large area (Figure 7-1a). The present study has resolved the unit in to separate lithological units even though some remained undifferentiated between gneiss, granite, schist and amphibolites. The radiometric signature of these units seemed to be affected showing a noisy uranium concentration due to the presence of topographically elevated Lubare quartzite in between (Figure 7-1b). Lithological units are better interpreted using gamma ray data (figure 7-1c). Multispectral data distinguish between these units based on their drainage nature. The undifferentiated between gneiss and granite has showed prominent drainage patterns whereas the other unit has devoid of such external drainage. Relatively large and deeper anomalies underneath the undifferentiated gneiss and granite whereas smaller and shallow seated anomalies characterized the undifferentiated schist and amphibolites. In this study two undifferentiated units were mapped across the Lubare quartzite namely: undifferentiated schist and amphibole and undifferentiated gneiss and granite (Figure 7-1d). Further explanation about the multispectral and radiometric signatures of the unit is provided in (Table 3-7) and (Appendix 2) respectively.

7.2.2. Pelitic Schist

Previously this unit has been mapped distinctly in the south and with intimate mixture of granite and gneiss in the north and east. Field investigation revealed that the unit is compositionally rich in mica with gradation in quartz. Radiometric data was found valuable in discriminating the unit from other lithological units due to its elevated K concentration (Figure 7-1b) and very low Th/K ratio. On the basis of similarity of this radiometric signature and in contrast to the previous geological map this unit was also identified in the northern part which has been previously mapped as undifferentiated granite, gneiss and schist (Figure 7-1d). The pelitic schist in the south has showed sharp enrichment of K towards its north which might be due to variation in weathering and hence this study has mapped the unit separately. In the south the pelitic schist has showed distinctive magnetic signature revealing short wavelength curvilinear anomalies which defined folded rock foliation. The newly identified unit in the north however was characterized by the emplacement of both deep and shallow seated high magnetic rounded bodies. Detail explanation on radiometric signature of units is presented in (section 5.3.2).

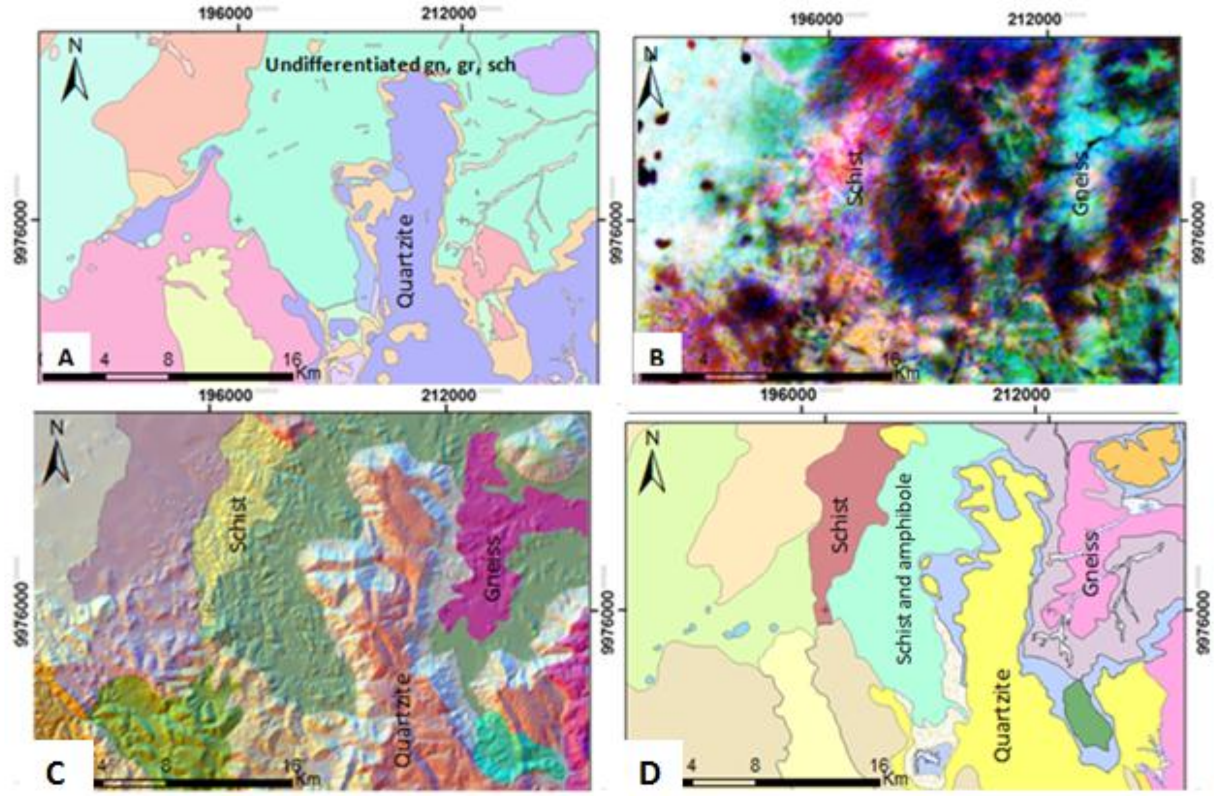

Figure 7-1: Subscens showing interpreted lithological units A) Old geological map by Reece, 1961 B) Ternary image C) Improved geological map by this study D) Interpreted lithological units from gamma ray data interpretation

7.2.3. Gneiss

The unit has been previously mapped in the SE and SW corners of Buhweju (Figure 7-2a). The previous work by Reece, (1961) has indicated the intimate association of gneiss with granite and minor pegmatite. It was difficult to characterize this unit in the field due to prolong intense weathering of the area but compositionally mainly made of quartz and feldspar with minor muscovite. However, radiometric data was found valuable in discriminating the gneissic terrains of the area through revealing higher concentration of eTh and eU which appeared cyan color on ternary image (Figure 7-1b and 7-2b). In contrast to the previous geological map more gneissic units were identified in the eastern and northern part of the area on the basis of similarity of radiometric signature. For example the area under the Ibanda quartzite (Figure 7-1b) has showed distinctive radiometric similarity with the already mapped gneissic terrains found in the SE and SW corners of the area. In addition, this study has identified the variation of K concentration throughout gneiss mapped at the SW corner (Table 5-2). This might be due to the variation in degree of weathering within this gneissic terrain. The aeromagnetic data has indicated that this unit has underlain by both shallow and deep seated high magnetic signatures (Figure 7-2c).

7.2.4. Granite

Reece, (1961) has mapped small units of granite in the south and east of Buhweju (Figure 7-2a). He has also noted that the unit has found intimately mixed with gneiss, pegmatite and aplites. However field data has showed relatively wider area covered by granite than mapped before especially in the southern part of the area. The intimate mixture of the unit with gneiss has also proved by very close similarity in radiometric signature. However, close inspection on radiometric composite ternary image has depicted the presence of granitic signature (Figure 7-2b). Aeromagnetic data didn't exhibit considerable variation beneath pelitic schist, gneiss and granite units exposed in the southern part of Buhweju (Figure 7-2c). Therefore, a wider area was identified as granite in the southern part which has been previously mapped as gneiss (Figure 7-2d).

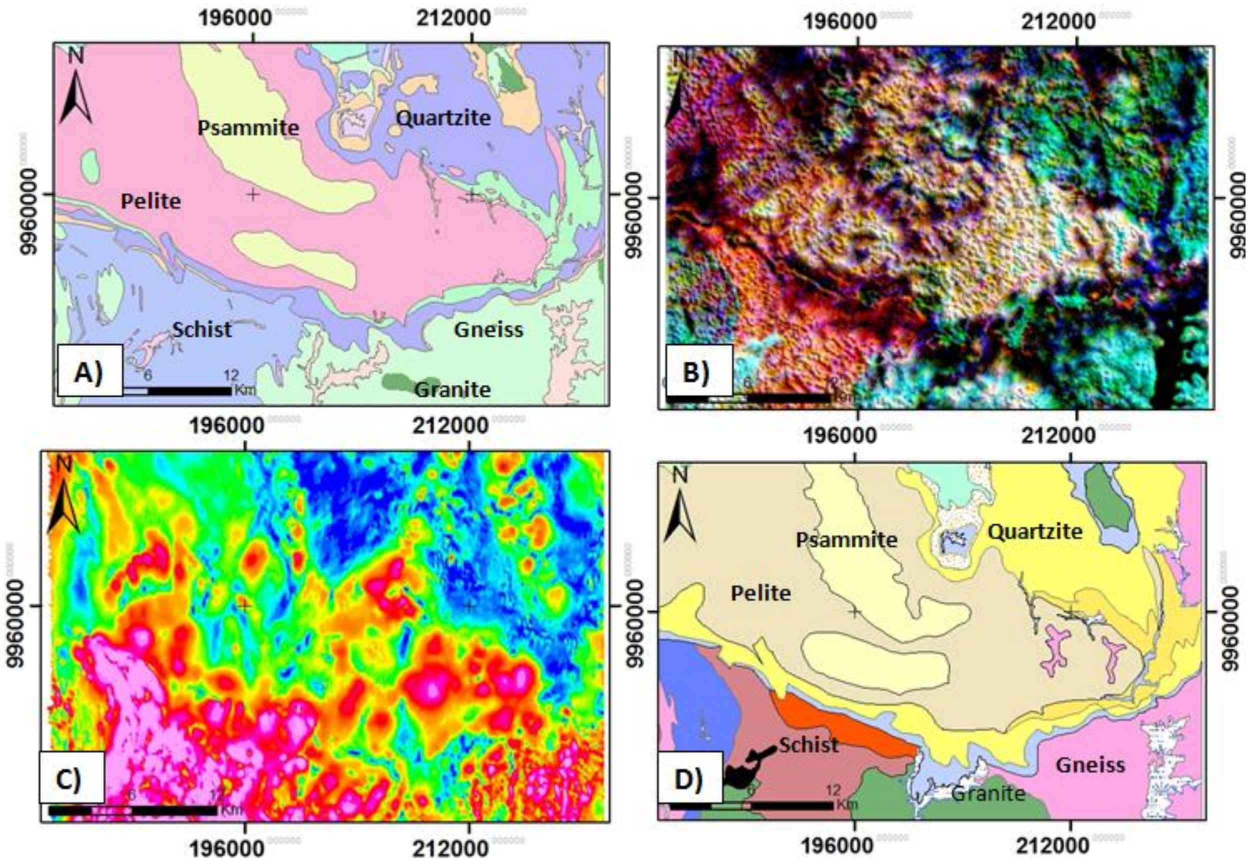

Figure 7-2: Subscenes showing interpreted lithological units A) Old geological map by Reece, 1961 B) Ternary image C) Analytical signal image D) improved geological map by this study

7.2.5. Quartzite

Two different quartzite types have been mapped by Reece, (1961): the Lubare quartzite and the Ibanda quartzite (Figure 7-1a). The relationship between Lubare quartzite, gneiss and schist has not yet been established. Previous study and field data indicated that both units were compositionally dominated by pure quartz with minor feldspars and muscovite. Two conspicuous characters were observed at both quartzite units: elevated topography and bounded by conglomerates and grits. This uplifting of stratigraphicaly lower unit to its present position might be tectonically controlled. Both units have indicated similar radiometric signature with elevated eTh concentration and hence appear greenish on ternary image (Figure 7-1b and 7-2b). Generally low aeromagnetic signature was depicted underneath quartzite unit.

7.2.6. Pelite and psammites

These units have covered large area of the Buhweju group rocks covered by dense protected forests and intimately mixed with quartzite. The boundary of these units was identified in most of the data sets used in this study. Generally elevated K, eTh and eU concentrations have been observed in pelite (Figure 7-2b). The presence of dense vegetation cover to the west would be the plausible reason for the gradual decrease in concentration of radioelement towards west. The quartzite bands (dominated by psammitic units) on the other hand showed relatively less concentration of radioelement and seemed to be affected by the topographic effect (Figure 7-2b). Two distinguishable units were depicted from visual interpretations vegetation texture and pattern applied on color composite, PCA and single bands of multispectral data (section 3.5). Broad, smooth and long wavelength magnetic anomaly was exhibited underneath these lithological units which proved the presence of deep seated basement (Figure 7-2c). The eastern part of these units has prominently intruded by a sub surface dyke with NNE trend. In addition, the boundary of pelite (with minor quartzite) has marked by elongated high magnetic signature. The quartzite (dominated by psammites) on the other hand has specifically underlain by shallow seated rounded magnetic anomalies.

7.2.7. Pleistocene units

These units have comprised of agglomerates, tuff, silt, clay and sand mapped covering extensive area in west of Buhweju. Multispectral data could help to differentiate tuff and agglomerates due to their rough texture on images. Radiometric data was rather found valuable tool in discriminating these units in to two broad units. The tuff and agglomerates are characterised by elevated concentrations of K, eTh and eU and hence appeared white on ternary image. The clay, silt and sand unit on the other hand showed elevated in eTh and eU but less in K concentration. Both units have underlain by deep seated prominent dykes of NNW trend. In addition, shallow surface high magnetic anomalies were observed on tuff and agglomerates obviously due to the presence of shallow seated rift volcanic rocks.

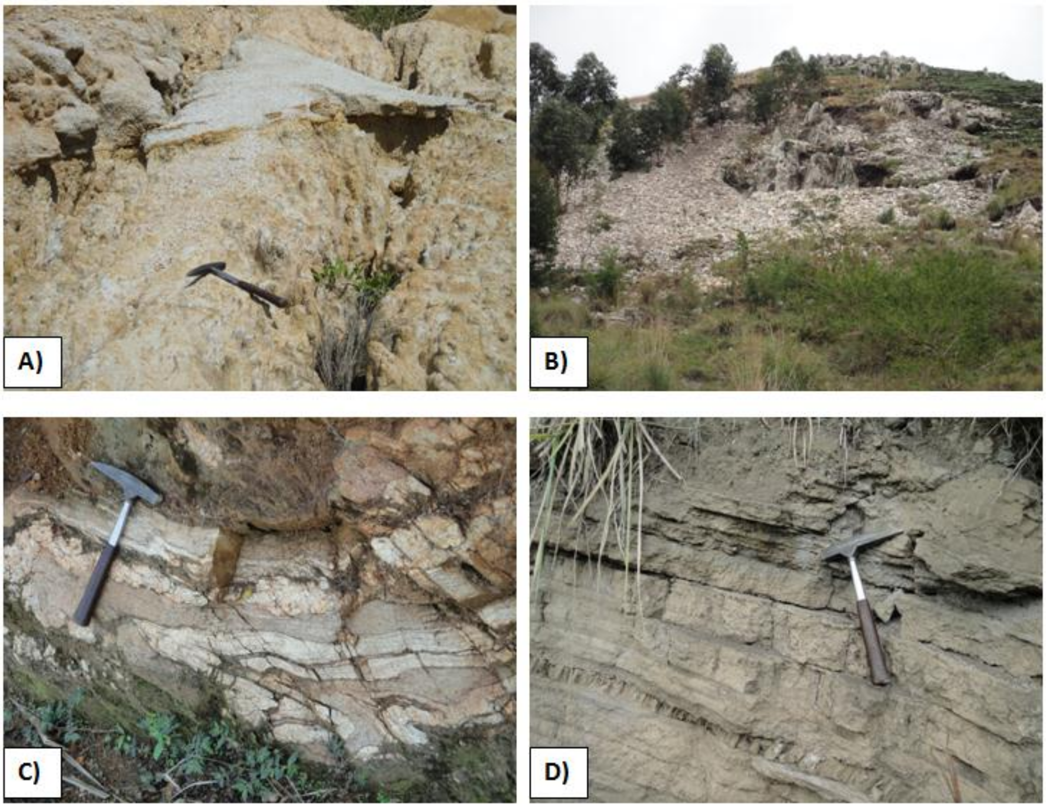

Figure 7-3: Field photos of different rocks A) Weathered granite B) Lubare quartzite C) Gneiss D) Folded tuff

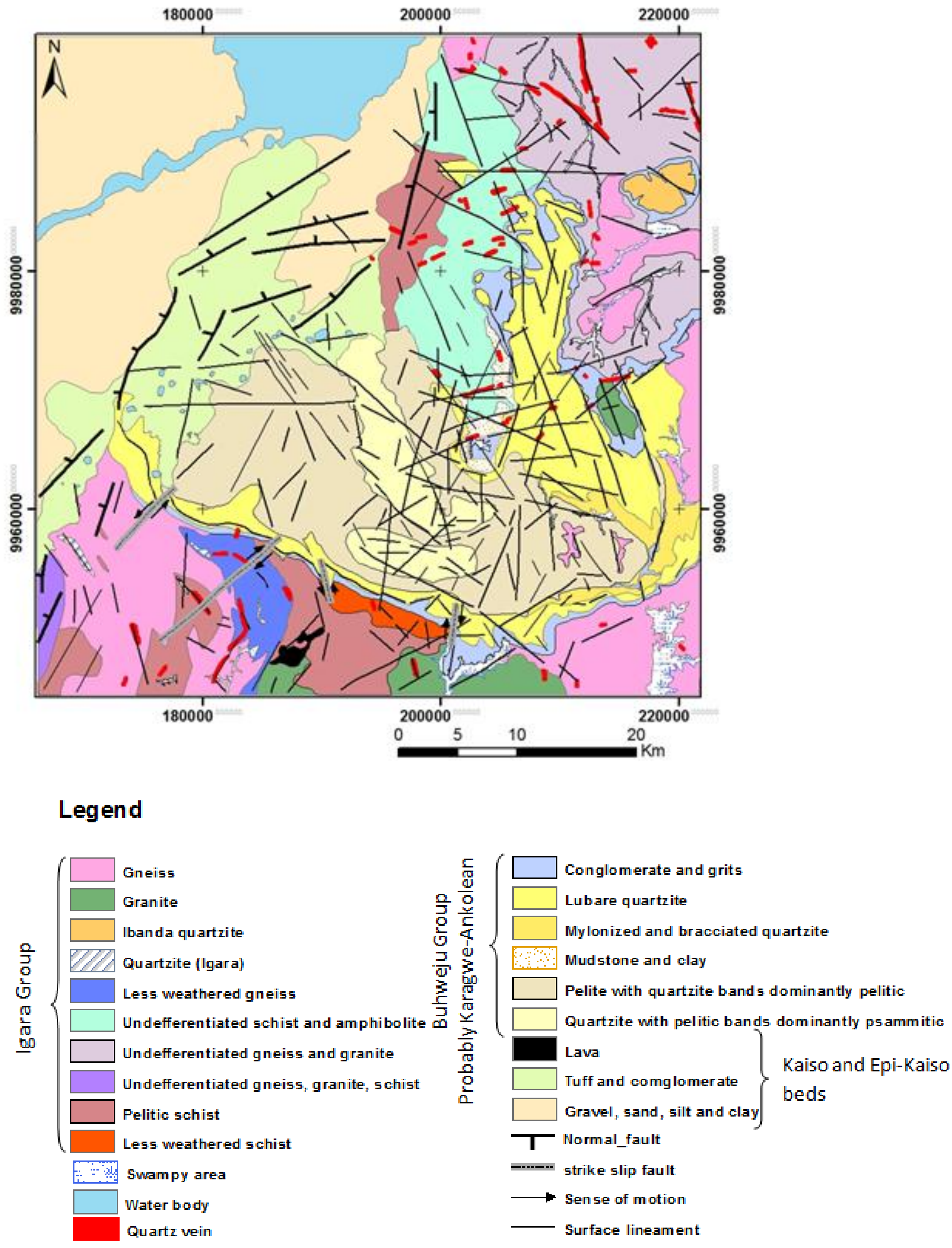

Figure 7-4: Improved geological map of Buhweju

7.3. Compiled Lineament Interpretation

Detail surface and subsurface lineament interpretations and analysis have been carried out on multispectral data, SRTM DEM data and aeromagnetic data (chapter 4 and chapter 6). The surface lineament density analysis (Figure 4-7) has depicted that the Buhweju group rocks (pelites, Psammites and Lubare quartzite) were affected by high lineament density along a narrow zone. It has also observed that this high density lineament continued further to the north following a narrow zone trending NNE and underlain by subsurface fault with high magnetic anomaly. The density analysis applied on subsurface magnetic lineaments (Figure 6-5) revealed high lineament concentration affecting the northern undifferentiated schist and amphibole including the newly identified pelitic schist. The Buhweju group rocks were also influenced by the subsurface magnetic lineament however the correlation between surface and subsurface lineament was generally considered weak. The orientation analysis has proved the existence of three tectonic patterns namely: NNW-SSE, ESE-WNW and NNE-SSW. These tectonic patterns were found consistent with the regional tectonic grain. The first two patterns are consistent with the regional Aswa shear zone (Shackleton, 1976) and the refolding event of both Igara and Buhweju Group rocks (Reece, 1961) respectively. Lineaments and faults trending NNE-SSW were considered to be coherent with the general trend of the western rift valley (Riad & El Etr, 1985). The orientation analysis applied on the quartz veins has resulted two prominent directions: N50-80E and N20-50W. The Lubare quartzite in the southern part is affected by sinistral movements as depicted from the multispectral, DEM SRTM and horizontal gradient images. The interpreted lineament map of Buhweju is shown in figure 7-5.

7.4. Mineralization

The regional and local aspect of mineralization in Buhweju area was discussed in detail (chapter 2). Post Kibaran orogeny events have been considered the prime cause for most of Kibaran mineralization. Generally two episodes of mineralization have been recognized: mineralization related to post orogenic rifting and mineralization related to post orogenic metamorphism (Pohl, 1994). The majority of gold occurrence in Buhweju has been from alluvial deposits but reef gold associated with sulphide veins has also been found (Reece, 1961; Wayland, 1934). The aim of this section is therefore to assess the control on gold mineralization in Buhweju area by synthesizing field data, mineral occurrence data, and interpreted lithological and structural data. The field surveyed gold mine areas and the provided gold occurrences data (Appendix 1) are used primarily for this purpose. Field data and lithological interpretations (Figure 7-6a) have revealed that Lubare quartzite and mudstone are the dominant country rocks hosting gold occurrences of the Buhweju plateau. Gold occurrences found below the plateau were hosted by different bedrocks including schist, gneiss, granites and amphibolites. In the surveyed mine areas, for example Kitaka mine suphides which occur in quartz veins have provided gold and found disseminated throughout the host rock (Figure 7-6b). As shown in (Figure 7-6c) most of the alluvial gold mines are located in low land stream courses covered by vegetation.

Spatial association has observed between surface lineament density and gold mine areas where the high lineament density and NNE tending narrow zone was observed hosting most of the gold mine areas. As shown in (Figure 7-7a) most of the gold mine occurrences are densely clustered in two areas. These clustered gold occurrence areas have showed difference in lithologies and subsurface magnetic signature. The gold occurrences at Kitaka mine are hosted by schist (Figure 7-7b) and underlain by low magnetic material (Figure 7-7c). On the other hand the gold occurrences at Katonga swamp are hosted by Lubare quartzite and mudstone (Figure 7-7b) and underlain by relatively high magnetic material (Figure 7-7c). There is also an association observed between the gold occurrences and quartz veins as shown in the figure 7-7d.

Currently exploration works are being in progress at different gold fields found in Tanzania, Uganda and Democratic Republic Congo (DRC). Two major strucutural corridors (gold trends) have been already identified by Magnus and Banro exploration companies (Corporation, 2006; Magnus, 2003). The

Twangiza trend (Figure 7-8a) is a north easterly interpreted structural corridor which controlled different gold deposits in Congo. The Geita trend (Figure 7-8a) is a north west trending interpreted lineament that control major gold trends in Tanzania. These structural corridors have showed consistency with the major regional trends like Aswan shear zone and the western rift valley. These trends are continued further to the north affecting different areas in SW of Uganda including Buhweju (Figure 7-8a).

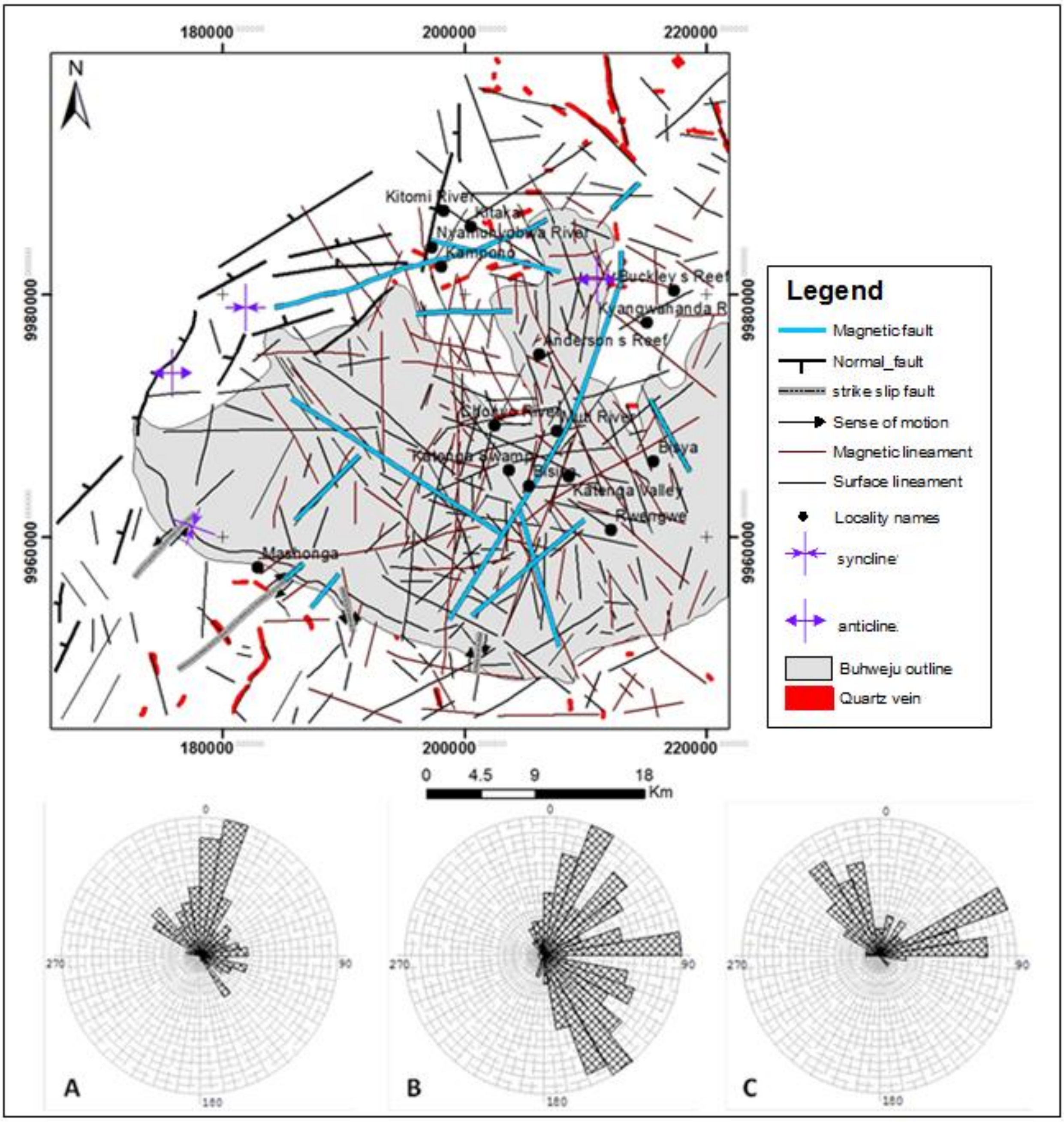

Figure 7-5: Lineament map of Buhweju

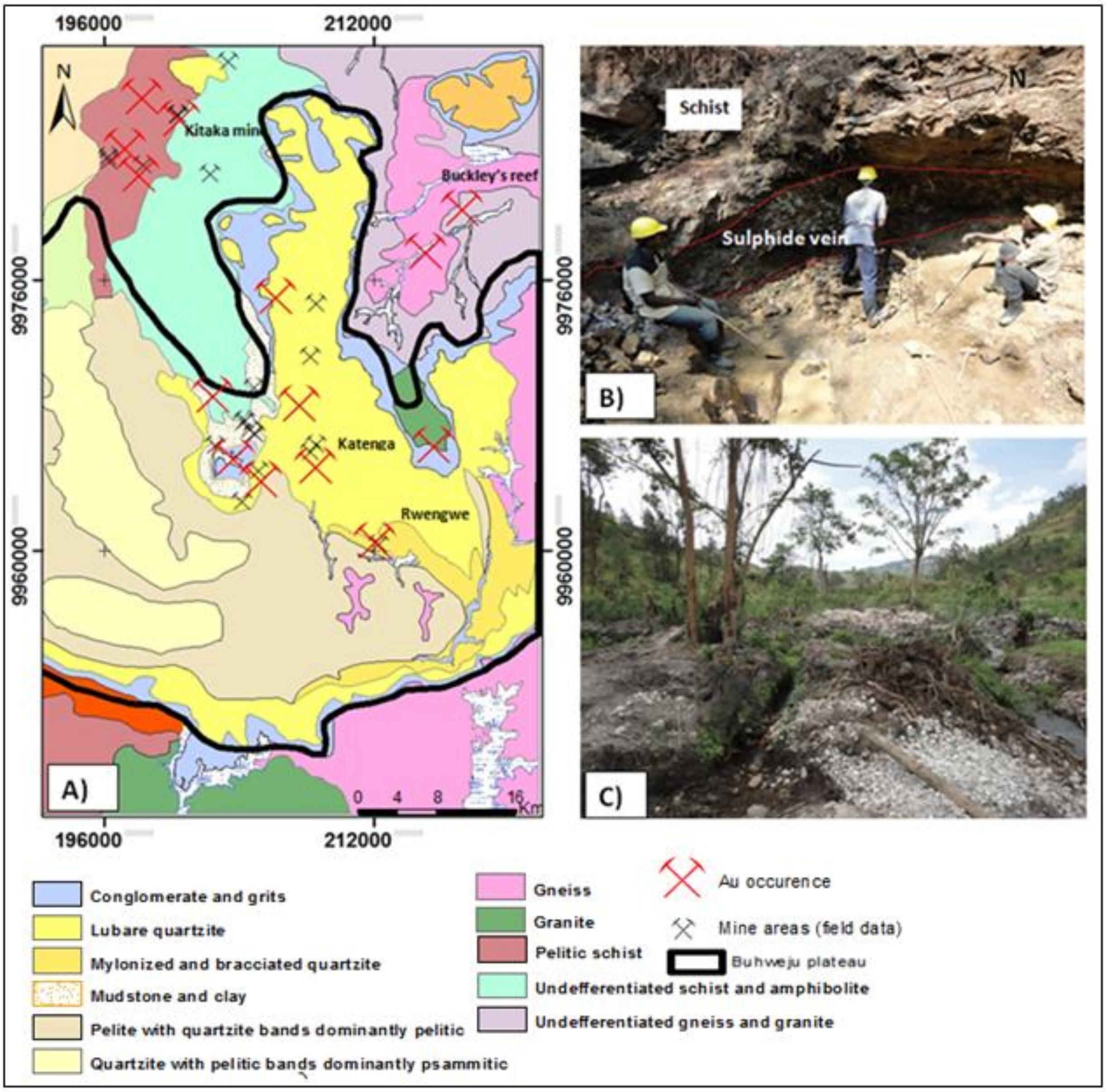

Figure 7-6: Field data and lithological interpretation on mineralization. **A)** Interpreted lithological units and gold occurrence areas. Schist and Mudstone are the common lithologies which hosted most of the gold fields in Buhweju. **B)** Field photo from Kitaka mine. Sulphide vein found disseminated throughout the schist (host rock) **C**) Field photo showing typical morphology of alluvia deposit in Buhweju. Always located downstream and covered with vegetation.

In Buhweju, three common structural orientations were clearly recognized. Two of the orientations have showed consistency with the trend of the Twangiza and Geita structural corridors. In the study area different magnetic faults were interpreted (Figure 7-5) among which the most prominent fault zone identified trends in NNE-SSE direction which could be the extension of the Twangiza structural corridor. This fault is characterized by high lineament density (Figure 7-7a) and high subsurface magnetic anomaly. In addition most of the gold occurrences in the study area are spatially controlled by this fault (Figure 7-9a). The NNW-SSE trending structure in Buhweju could also be interpreted in terms of the Gieta trend and the regional Aswan shear zone. The high lineament density zone and densely clustered gold occurrences at Katonga might be due to the intersection of these oppositely trending structures. Generally two trends could be recognized (Figure 7-9b) from the distribution of gold occurrences of the area that could be related with the locally identified structures as well as the regional structural trends.

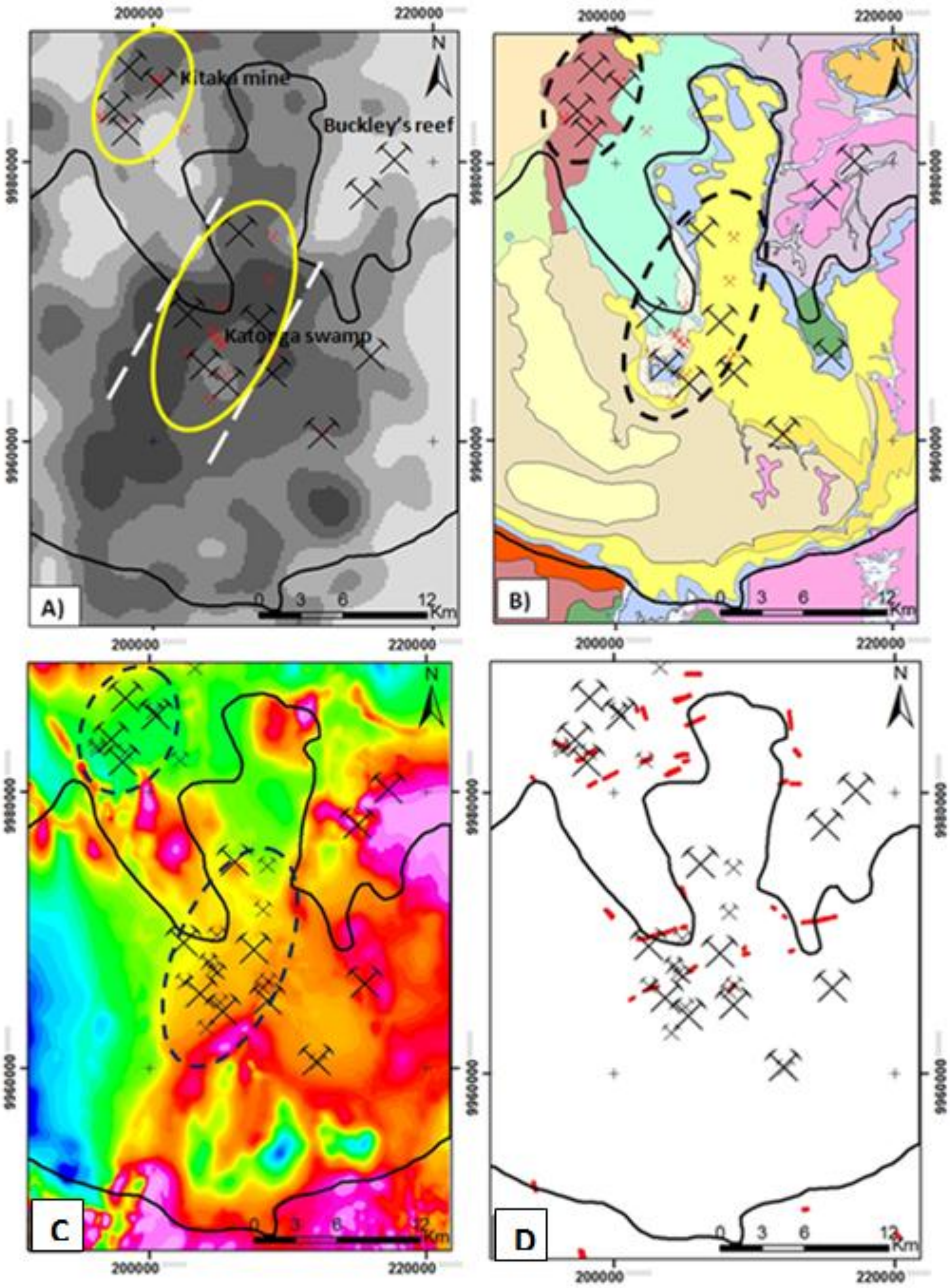

Figure 7-7: Distribution of gold occurrence areas. A) The relationship between lineament density and gold occurrences. Circles indicate the two clustered areas of gold occurrences and their density pattern. B) Lithology and mineral occurrence association. C) Subsurface magnetic signature beneath mineral occurrence areas. D) Quartz veins and gold occurrences. Explanation is given in detail in the text.

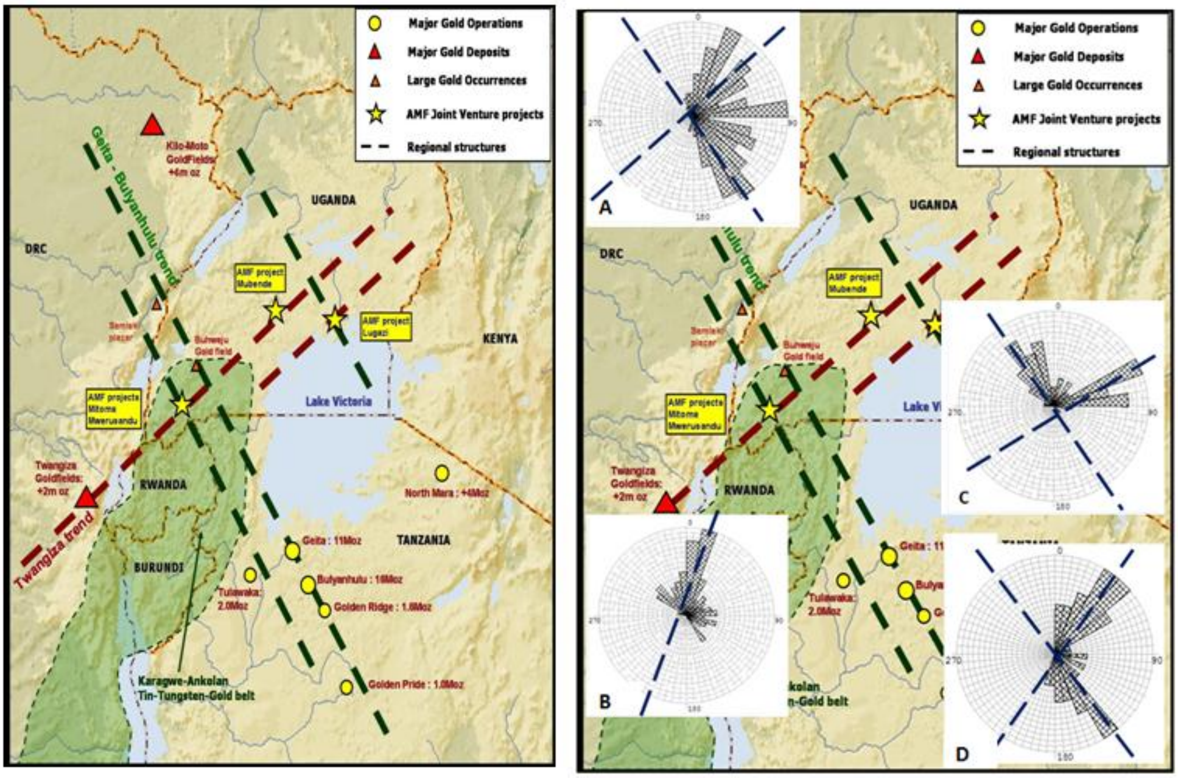

Figure 7-8: The Twangiza and Gieta trends A) The gold occurrences in Congo and Tanzania controlled by the Twangiza and Gieta gold trends (source: (Corporation, 2006; Magnus, 2003) B) The relationship established between the gold trends and orientations of lineaments interpreted in the area. (a) Shows rose diagrams for surface lineaments (b) for sub surface lineaments (c) for quartz veins (d) trends of high magnetic anomaly bodies

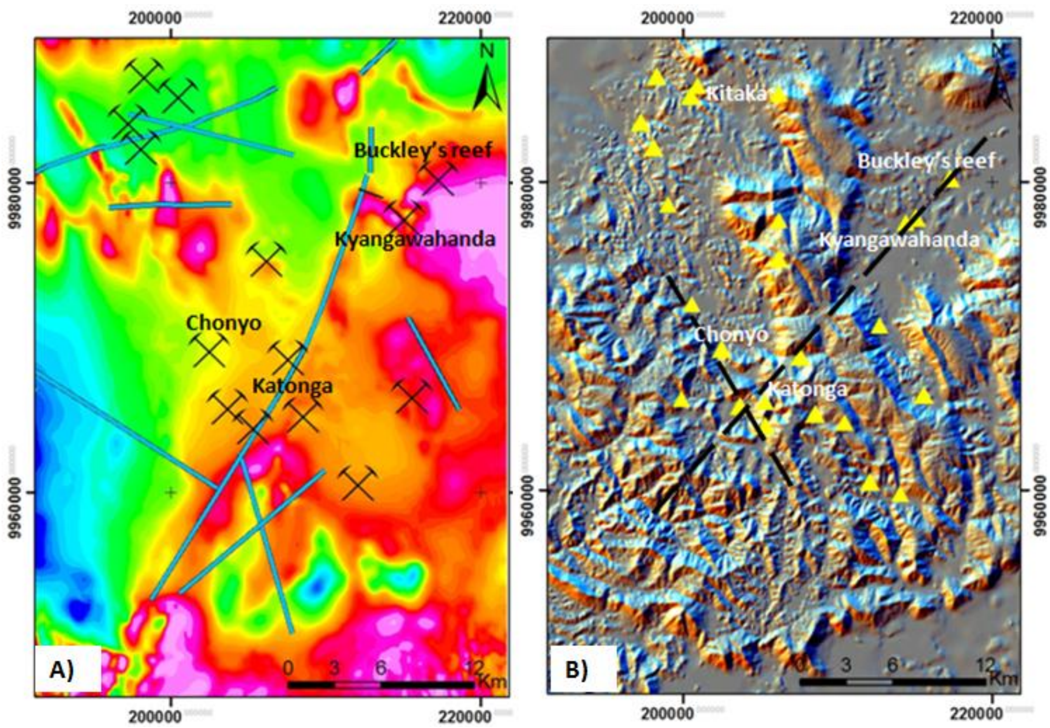

Figure 7-9: Structural corridors A) the spatial association of gold occurrences with interpreted magnetic faults B) General alignment of gold occurrences in the area which showed consistency with the interpreted lineament orientation as well as the Twangiza and Geita trends

8. CONCLUSION AND RECOMMENDATIONS

8.1. Conclusion

The primary objective of the research was to use various remotely sensed data and apply the GIS technique to assess the inter-relationship between lithology and structure and to qualitatively assess its control on the Buhweju gold field. In this research the general outputs achieved are: 1) the improved geological map of Buhweju 2) interpreted structural/lineament map of Buhweju 3) qualitative interpretations on control of mineralization of Buhweju gold field. The general conclusions of the study are presented here more focussed towards providing relevant responses for the major questions of the study.
The qualitative interpretation conducted on relationship between lithologies and structure in Buhweju has showed remarkable result. Most of the gold occurrences in the study area were not found scattered and dispersed rather localized in a preferred orientations and preferred host rock. Two major clusters of gold occurrences were identified in Buhweju gold field. The cluster found at Kitka was characterised by low subsurface magnetic anomaly and high subsurface lineament density. Whereas the gold occurrences found at Katonga are hosted by mudstone and lubare quartzite and underlain by high magnetic anomaly. Major structures were interpreted with respect to the regional structural corridors which have controlled the distribution of gold occurrences in the area. Particularly the NNE-SSW, NNW-SSE trending structures and their intersection have determined the localization of the most of the Buhweju gold occurrences.

Even though it was difficult to quantify how useful information was provided by each data set, in this study all the available data sets have provided useful information. Particularly the gamma ray data has found to be an invaluable aid, which together with modern enhancement and integration techniques have assisted in the visualization and discrimination of lithological units of the area. Among the various image enhancement techniques image fusion and pan-sharpening of the radiometric composite image with multispectral data and SRTM DEM have resulted better lithological differentiation in the area. On the basis of similar radiometric signature different Precambrian basement lithologies including schist, gneiss and granite could be identified and mapped which were not mapped before. The SRTM DEM of the area has revealed topographic and structural information of the complex Buhweju plateau. Useful information was also depicted from aeromagnetic data about the distribution of sub surface magnetic domains.

Subsequent extractions of both surface and subsurface lineaments were carried on multispectral, SRTM DEM and aeromagnetic data. The orientation analysis has revealed three dominant lineament orientations which determine the tectonic grain of the area, NNW-SSE, ESE-WNW and NNE-SSW. These orientations were found consistent with the two major regional tectonic trends. The NNE-SSW has considered a major tectonic grain of the area related to the western rift valley while the NNW-SSE seemed attributed to the regional Aswan shear zone. Non-orientation density analysis applied on the individual surface and subsurface lineaments has indicated that the Buhweju group rocks were highly affected by surface lineamnents whereas the Precambrian basement rocks were affected mainly by subsurface lineaments. Generally the density patterns of surface and subsurface lineaments are weakly correlated.

8.2. Recommendations

Various enhancements applied in this study resulted better images for visual interpretation of structures and lithological units. However, two main factors are identified which greatly hinder the interpretability of remote sensing data especially multispectral and gamma ray. These are topographic effect and vegetation cover. More than half of Buhweju is covered by two dense forests protected by forestry department of Uganda. Moreover, Buhweju plateau is considered to be the highest land in west of Uganda. These factors have seriously affected the information content of both multispectral and gamma ray data. This study has made an effort to suppress the effect of vegetation even though the effect was still significant. Therefore, this study highly recommend for the next studies to be conducted on Buhweju based on remote sensing tools to seriously consider the effect of vegetation. Similarly the topography effect on gamma ray data is significant by affecting the distribution of radioelement around the Buhweju plateau for which this data should be exclusively corrected for topographic effects of Buhweju.

This study has better defined the tectonic setting of Buhweju area through integrated analysis of surface and subsurface data. Hence similar approaches are recommended to other areas of SW Uganda. The source of gold mineralization in Buhweju is still not fully known but this study has at least identified subsurface high magnetic zones, magnetic faults and surface lineaments which could contribute an input pertaining to search for source of mineralization. Therefore, detail geochemical investigation and high resolution geophysical data interpretation are recommended for further understanding of the source of mineralization in Buhweju gold field. New lithological boundaries are identified from multispectral data interpretation but have not incorporated in the final map due to inaccessibility of the area but recommended that they need to be verified.

LIST OF REFERENCES

Abdullah, A., Akhir, M. J., & Abdullah, I. (2010). Automatic Mapping of Lineaments Using Shaded Relief Images Derived from Digital Elevation Model (DEMs) in the Maran – Sungi Lembing Area, Malaysia. *15*, 949-956.

Allek, K., & Hamoudi, M. (2008). Regional-scale aeromagnetic survey of the south-west of Algeria: A tool for area selection for diamond exploration. *Journal of African Earth Sciences, 50*, 67–78.

Alsaud, M. M. (2008). Structural mapping from high resolution aeromagnetic data in west central Arabian Shield, Saudi Arabia using normalized derivatives. *1*, 129-136.

Baker, B. H. (1971). Explanatory note on the structure of the southern part of the African Rift System *Tectonics of Africa 6* 543-548

Benomar, T., & Fuling, B. (2005). Improved geological mapping using landsat-5 TM data in Weixi area, Yunnan province China. *Geo-Spatial Information Science, 8*(2), 110-114.

Black, R. (I967). Chronique Mines. *364*, 225.

Buchwaldt, R., Toulkeridis, T., Todt, W., & Ucakuwun, E. K. (2008). Crustal age domains in the Kibaran belt of SW-Uganda:Combined zircon geochronology and Sm-Nd isotopic investigation
African Earth Sciences, 51, 4-20.

Butt, C. R. M., Lintern, M. J., & Anand, R. (2000). Evolution of regolith and landscapes in deeply weathered terrain- Implication for geochemical exploration. *Ore Geology Reviews, 16*(3-4), 168-183.

Cahen, L., Snelling, N. J., Delhal, J., & Vail, J. R. (1984). The geochronology and evolution of Africa. .

Casas, A. M., Cortes, A. L., Maestro, A., Soriano, M. A., Riaguas, A., & Bernal, J. (2000). A program for lineament length and density analysis. *Computers and Geosciences 26*, 1011-1022.

Chavez, P. S., Sides, S. C., & Anderson, J. A. (1991). Comparison of three different methods to merge multi-resolution and multi-spectral data: LANDSAT TM and SPOT Panchromatic. *Photogrammetic Engineering and Remote Sensing, 57*, 295–303.

Chavez, S. P., Sides, C. S., & Anderson, A. J. (1991). Comparison of 3 different methods to merge multiresolution and multispectral data-Landsat TM and Spot Panchromatic. *Photogrammetric Engineering and remote sensing, 57*, 295-303.

Chernicoff, C. J., Richards, J. P., & Zappettini, E. O. (2002). Crustal lineament control on magmatism and mineralization in northwestern Argentina: geological, geophysical, and remote sensing evidence. *Ore Geology Reviews, 21*(3-4), 127-155.

Cobme, A. D. (1932). *The geology of Southwest Ankole and adjucent territories with special reference to tin deposit*.

Corporation, B. (2006, 04/02). 2006 Exploration Program. Retrieved 13/02, 2011, from http://www.banro.com/s/Twangiza.asp?ReportID=307246&_Title=2006-Exploration-Program

Crippen, E. R., & Blom, G. R. (2001). Unveiling the Lithology of Vegetated Terrains in Remotely Sensed Imagery. *Photogrammetric Engineering & Remote Sensing, 67*, 935-943.

Dickson, B. L., & Scott, K. M. (1997). Interpretation of aerial gamma ray surveys-adding the geochemical factors. *Journal of Australian geology and geophysics, 17(2)*, 187-200.

Drury, S. A. (2001). *Image interpretation in geology*: Nelson Thornes Blackwell Science.

Duval, J. S. (1983). Composite color images of aerial gamma-ray spectrometric data. *Geophysics, 48*(6), 722-735.

Elliot, G. F. S., & Gregory, J. W. (1895). The geology of Mount Ruwenzori and some adjoining regions of equatorial Africa. . *51*, 669–680.

Gabert, G. (1990). Lithostratigraphic and tectonic setting of gold mineralization in the Archean cratons of Tanzania and Uganda, East Africa. *Precambrian Research, 46*(1-2), 59-69.

Gad, S., & Kusky, T. (2007). ASTER spectral ratioing for lithological mapping in the Arabian-Nubian shield, the Neoproterozoic Wadi Kid area, Sinai, Egypt. *Gondwana Research, 11*(3), 326-335.

Gay, S. P. (1972). Fundamental characterstics of aeromagnetic lineaments:thier geological significances and their gnificance to geology. Salt Lake City, Utah.

Ghazala, H. H. (1993). Geological and structural interpretation of airborne surveys and its significance for mineralization, South Eastern Desert, Egypt. *Journal of African Earth Sciences (and the Middle East), 16*(3), 273-285.

Gillespie, A., Kahle, A., & Walker, E. R. (1987). Color enhancement of highly correlated images. II. Channel ratio and chromaticity transformation techniques. *Remote Sensing of Environment, 22*, 343-365.

Grant, F. S. (1985). Aeromagnetics, geology and ore environments. Magnetite in igneous, sedimentary and metamorphic rocks : An overview. *Geoexploration, 23*, 303-333.
Grant, N. K. (1967). Nature. *215*, 609.
Grant, N. K. (1969). Bulletin of Geological Society. *80*, 45.
Groves, D. I., Goldfarb, R. J., Gebre-Mariam, M., Hagemann, S. G., & and Robert, F. (1998). Orogenic gold deposits: A proposed classification in the context of their crustal distribution and relationship to other gold deposit types. *Ore Geology Reviews, 13*, 7-27.
Gunn, P. J., Maidment, D., & Milligan, P. R. (1997). Interpreting aeromagnetic data in areas of limited outcrop. *17*(2), 175-185.
Gunn, P. J., Minty, B. R. S., & Milligan, P. R. (1997). The Airborne Gamma-Ray Spectrometric Response Over Arid Australian Terranes. *Radiometric Methods and Remote Sensing, 96*, 733-740.
Gupta, R. P. (1991). *Remote Sensing Geology* Berlin: Heidelberg: Springer-Verlag.
Harris, J. F. (1961). Summary of the geology of Tanganyika. *Economic geology, 1*.
Henderson, B. D., Ferrill, A. D., & Clarke, C. K. (1996). Mapping geological falukts using image processing techniques applied to hill-shaded digital elevation models. 240-245.
Hepworth, J. V., & Macdonald, R. (1966). Orogenic belts of the northern Uganda basement.*, 210*, 726–727.
Ikingura, J. R., Reynolds, P. H., Watkinson, D. H., & Bell, K. (1992). 40Ar/39Ar dating of micas from granites of NE Kibaran Belt (Karagwe-Ankolean), NW Tanzania. *Journal of African Earth Sciences (and the Middle East), 15*(3-4), 501-511.
Jaques, A. L., Wellman, P., Whitaker, A., & Wyborn, D. (1997). High resolution geophysics in modern geological mapping. *17*(2), 159-173.
Jayawardhana, M. P., & Sheard, N. S. (2000). The use of airborne gamma-ray spectrometry- A case study from the Mount Isa Inlier, Northwest Queensland, Australia. *Geophysics, 65*, 1993-2000.
Johnson, S. S., Gathright, M., T., & Henika, S. W. (1979). Gamma-ray Specrtometry and Geologic mapping. *Remote Sensing of Environment, 25*, 17-24.
Khan, S. D., & Glenn, N. F. (2006). New strike-slip faults and litho-units mapped in Chitral (N. Pakistan) using field and ASTER data yield regionally significant results. *International Journal of Remote Sensing, 27*(20), 4495 - 4512.
Klerkx, J., Liegeois, J. P., Lavreau, J., & Claessens, W. (1987). Crustal evolution of the northern Kibaran Belt, eastern and central Africa. 217- 233.
Leggo, P. J. (1974). A geochronological study of the basement complex of Uganda.*, 130*, 263–277.
Link, K., Koehn, D., Barth, M., Tiberindwa, J., Barifaijo, E., Aanyu, K., et al. (2010). Continuous cratonic crust between the Congo and Tanzania blocks in western Uganda. *International Journal of Earth Sciences*, 1-15.
MacDonald, R. (1966). Uganda Geology, Scale 1:1,500,000.- Department of Geological Survey Mines; Entebbe.
Magnus. (2003, 12/2009). Uganda Projects. Retrieved 13/02, 2011, from http://www.magnusresources.com/africa_uganda_projects.htm
Masoud, A., & Koike, K. (2006). Tectonic architecture through Landsat-7 ETM+/SRTM DEM- derived lineaments and relationship to the hydrogeologic setting in Siwa region, NW Egypt. *Journal of African Earth Sciences 45*, 467-477.
Muwanga, A., Schumann, A., & Biryabarema, M. (2001). Landslides in Uganda, Documentation of a Natural Hazard.*, 136*, 111-115.
Nicolet, J. P., & Edric-Krausz, G. (2003). *Guidelines for radioelement mapping using gamma ray spectrometry data*. Vienna, Austria: IAEA.
O'Leary, D. W., Friedman, J. D., & Pohn, H. A. (1976). Lineament, linear, lineation: Some proposed new standards for old terms. *Geological Society America Bulletin, 87*, 1463-1469.
Owusu, A. E., Woldai, T., Carranza, M. J. E., & Hale, M. (2006). Analysis and Integration of Landsat ETM and SRTM Data for Geological Mapping of the Kibi Area in Ghana. 330-338.
Owusu, E. A., Woldai, T., Carranza, E. J. M., & Hale, M. (2006). Analysis and Integration of Landsat ETM and SRTM Data for Geological Mapping of the Kibi Area in Ghana.
Perrotta, M. M., Almeidab, R. I. T., Andrade, F. B. J., Souza Filhoc, R. C., Rizzotto, J. G., & Santosb, M. G. M. (2008). Remote Sensing Geobotany and Airborne Gamma-ray data Applied to Geological Mapping within Terra Firme Brazilian Amazone Forest: A Comparative study in the Guapore Valley (Mato Grosso State, Brazil). *Remote Sensing and Spatial Information Sciences*
275-1280.

Pohl, W. (1994). Metallogeny of the northeastern Kibaran belt, Cental Africa-Recent Perspectives. *Ore Geology Reviews, 9*, 105-130.

Porwal, A., Carranza, E. J. M., & Hale, M. (2006). Tectonostratigraphy and base-metal mineralization controls, Aravalli province (western India): New interpretations from geophysical data analysis. *Ore Geology Reviews, 29*(3-4), 287-306.

Qaid, M. A., & Basavarajappa, T. H. (2008). Application of Optimum Index Factor Technique to Landsat-7 Data for Geological Mapping of North East of Hajjah, Yemen. *1* 84-91.

Qari, M. Y. H. T. (1992). Improving geological mapping in the Arabian Shield using Landsat Thematic Mapper imagery—Jabal Duhayyah area. *International Journal of Remote Sensing, 13*(15), 2765 - 2772.

Quadros, P. F. T., Koppe, C. J., Strieder, J. A., & Costa, L. C. F. (2003). Gamma-Ray Data Processing and Integration for Lode-Au Deposits Exploration. *Natural Resources Research 12*, 57-65.

Radulescu, J. (1982). Mineralization in the Karagwe-Ankolean system of East African/Burundi: In the development potential of precambrian mineral deposits. 217-225.

Ramadan, M. T., El Mongy, A. S., & El Dein, S. S. (2009). Exploration for Uranium and Thorium Mineralizations at Wadi Um Laseifa Area, Central Eastern Desert, Egypt: Using Remote Sensing Technique. *Australian Journal of Basic and Applied Sciences, 3*(2), 689-697

Reece, A. W. (1961). *Explanation of the Geology of sheet 76 (Buhwezu).*

Riad, S., & El Etr, H. A. (1985). Bouguer Anomalies and Lithosphere-Crustal Thickness in Uganda *Journal of Geodynamics, 3*, 169-186.

Rowan, L. C., & Mars, J. C. (2003). Lithologic mapping in the Mountain Pass, California area using Advanced Spaceborne Thermal Emission and Reflection Radiometer (ASTER) data. *Remote Sensing of Environment, 84*(3), 350-366.

Rumvegeri, B. T. (1991). Tectonic significance of Kibaran structures in Central and Eastern Africa. *Journal of African Earth Sciences (and the Middle East), 13*(2), 267-276.

Saggerson, E. P., & Turner, L. M. (1972). 24th International Geological Congress *1*, 153.

Saraf, A. K., Mishra, P., Mitra, S., Sarma, B., & Mukhopadhyay, D. K. (2002). Remote sensing and GIS technologies for improvements in geological structures interpretation and mapping. *International Journal of Remote Sensing, 23*(13), 2527 - 2536.

Sarapirome, S., Surinkum, A., & Saksutthipong, P. (2002). Application of DEM Data to Geological Interpretation: Thong Pha Phum Area, Thailand.

Schetselaar, E. M., Chung, C. J. F., & Kim, E. (2000). Integration of Landsat TM, Gamma-Ray, Magnetic, and Field Data to Discriminate Lithological Units in VegetatedGranite-Gneiss Terrain. *Remote Sensing of Environment, 71*(1), 89-105.

Schetselaar, E. M., & Ryan, J. J. (2009). Remote predictive mapping of the Boothia mainland area, Nunavut, Canada: an iterative approache using landsat ETM, aeromagnetic and geological field data. *Canadian Journal of Remote Sensing, 35*, S72-S94.

Schetselaar, E. M., Tiainen, M., & Woldai, T. (2008). Integrated geological interpretation of remotely sensed data to support geological mapping in Mozambique. *48*, 35-63.

Shackleton, R. M. (1976). Pan-African Structures. *280*, 491-497.

Shives, R. B. K., Charbonneau, B. W., & Ford, K. L. (2000). The detection of potassic alteration by gamma-ray spectrometry-Recognition of alteration related to mineralization. *65(6)*, 2001-2011.

Singh, B., & Dowerah, J. (2010). ASTER DEM Based Studies for Geological Investigation around Singhbhum Shear Zone (SSZ) in Jharkhand, India. *Journal of Geographic Information System, 2*, 11-14.

Soulakellis, A. N., Novak, D. I., Zouros, N., Lowman, P., & Yates, J. (2006). Fusing Landsat-5/TM Imagery and Shaded Relief Maps in Tectonic and Geomorphic Mapping: Lesvos Island, Greece. *Photogrammetric Engineering & Remote Sensing, 72,*, 693–700.

Tack, L., Duchesne, J. C., Lirgois, J. P., & Deblond, A. (1994). Two successive mantle-derived A-type granitoids in Burundi: Kibaran late-orogenic extensional collapse and lateral shear along the edge of the Tanzanian craton.

Tanner. (1970). The Ruwenzori Fold Belt of East Africa. *14*, 3–7.

Tsige, L. (2006). Metamorphism and gold mineralization of the Kenticha–Katawicha area: Adola belt, southern Ethiopia. *Journal of African Earth Sciences, 45* 16–32.

Wayland, E. J. (1934). *crystalline gold and the possibilities of auriferous lodes in the vicincity of the Muti stream, in Kenya-Uganda minerals exploration*.

Wickert, L. M., & Budkewitsch, P. (2004). ASTER - a geological mapping tool for Canada's North. Case Study: The Belcher Islands, Hudson Bay, Nunavut, Canada. *2* 1300 - 1303

Wilford, J. R. (2002). Airborne Gamma-ray Spectrometry. *Geophysical and Remote Sensing Methods for Regolith Exploration*, 46-52.

Wilford, J. R., Bierwirth, P. N., & Craig, M. A. (1997). Application of airborne gamma-ray spectrometry in soil/regolith mapping and applied geomorphology. *17(2)*, 201-216.

Williams, R. S. (1983). Manual of Remote Sensing *American Society of Photogrammetry*, 1667-1951.

Won-In, K., & Charusiri, P. (2003). Enhancement of thematic mapper satellite images for geological mapping of the Cho Dien area, Northern Vietnam. *International Journal of Applied Earth Observation and Geoinformation, 4*, 183–193.

Yesou, H., Besnus, Y., & Rolet, J. (1993). Extraction of spectral information from Landsat-TM data and merge with spot panchromatic imagery- Acontribution to the study of geological structures. *photogrammetry and remote sensing, 48*, 23-36.

ZHANG, Y., XIONG, S., & CHEN, T. (1998). Application of Airborne Gamma-ray Spectrometry to Geoscience in China. *Applied Geophysics, 49*(2), 139-146.

Appendix 1
Field collected lithological and structural data

ID	X	Y	Z	Litho-unit	strike_dip	dip dire/amount	mine	structutre
1	216758	9981046	1442	schist			mine	
2	211492	9978918	1524	micacious schist	40w/20	220/20		
3	211252	9979763	1589	Fe rich quarzite				
4	211107	9980183	1618	quarzitic conglomerate				
5	211101	9980147	1626	conglomerate	10E/40	290/40		
6	211076	9980198	1625	folded coglomerate				Anticline
7	210598	9980288	1686	bedded sandstone				
8	209923	9976519	1865	quarzite				vein
9	209272	9968854	1865	quarzite				qtz vein
10	208588	9966327	1848	quarzite			gold mine	vein
11	208226	9965874	1848	quarzite			mine	vein
12	205130	9964770	1792	quarzite			mine	
13	202269	9963759	1639	granitic gniess				
14	201356	9965460	1608	pellite	70w/20	250/20		vein
15	200377	9985882	1152	dolerite	N70E		mine	qtz vein
16	200344	9985831	1182	dolerite			kitaka	
17	203148	9988118	1375	mica schist	080/90	350/90		
18	203508	9988969	1334	amphibolite				
19	204237	9987834	1381	schist				
20	204342	9986184	1322	gniess	158/60	68/60		
21	204242	9986223	1306	mica schist				
22	204242	9986576	1312	gniess				
23	198261	9989403	1057	gniess				
24	194642	9988410	987	gravel, sand cilt				
25	192263	99888028	955	gravel, sand cilt				
26	190907	9985451	984	gravel, sand cilt				
27	192463	9980082	1112	amphibolite	030/44	120/44		
28	190203	997852	1068	conglomerate				
29	190609	9978263	1138	quarzite	044/50	134/50		
30	187216	9978479	1106	tuff				
31	182042	9977883	1069	tuff				syncline
32	177598	9977190	1075	tuff				
33	176005	9972510	1248	tuff				anticline
34	177576	9967524	1357	tuff				
35	176367	9963119	1484	quarzite				
36	176393	9961286	1568	quarzite	170/40	080/40		
37	176630	9961047	1593	schist+quarzite	164/36	74/36		
38	176573	9961085	1587	quarzite	070/20	160/20		syncline
39	181416	9956287	1408	gniess	040/58	130/58	mine	
40	182084	9956592	1401	schist			mine	

41	182785	9957714	1424	schist			mine	
42	182831	9957757	1427	schist			mine	vein
43	183032	9958246	1461	schist				vein
44	195495	9986150	994	quarzite				
45	196251	9985397	1007	quarzite				
46	196037	9984917	927	quarzite+schist				
47	197203	9984437	1048	quarzite+schist				
48	197343	9983817	1097	quarzite				
49	197544	9983717	1125	biotite schist				
50	197589	9983660	1137	biotite schist				
51	202263	9982348	1378	schist			mine	vein
52	198312	9982877	1244	schist			mine	vein
53	196182	9983524	985	amphibolite	198/40	108/40		
54	196242	9983381	977	granite			mine	vein
55	196174	9983303	981	granite				
56	196274	9983118	964	granite			mine	
57	204180	9981516	1394	granite				vein
58	205899	9985230	1510	schist	90/76			vein
59	205746	9985342	1471	schist				
60	207298	9988723	1405	schist	N30E			
61	205383	9986749	1449	schist				
62	205050	9982709	1448	schist				
63	207783	9942882	1471	granite	100/70	010/70		vein
64	209107	9944694	1536	granite				
65	208803	9946156	1572	granite				vein
66	208902	9948392	1581	quarzite				
67	215842	9953441	1525	schist				
68	214810	9954058	1493	swampy area				
69	214188	9954679	1505	conglomerate				
70	213735	9956183	1525	schist				
71	213884	9957293	1558	schist				
72	213223	9958826	1547	conglomerate				
73	214314	9960017	1588	quarzite				
74	211815	9960615	1592	schist				
75	210826	9960248	1672	schist				
76	209003	9959668	1723	schist				
77	212274	9960417	1572	schist			mine	
78	215649	9958750	1639	schist				
79	216437	9957996	1723	schist				
80	216741	9957333	1597	schist				

81	217244	9957004	1523	quarzite				
82	218011	9957958	1515	quarzite_schist	070/15	250/15		
83	218713	9961414	1581	schist	070/15	250/15		
84	219113	9962032	1712	quarzite_schist				
85	216542	9966598	1717	schist				
86	214698	9968093	1679	schist				
87	243827	9968710	1636	schsit_conglomerate				
88	213934	9968834	1569	quarzite				
89	213855	9969903	1498	schist				
90	213258	9971941	1461	pelite_schist				
91	214035	9972556	1460	schist_qazri_pellite				
92	214420	9975926	1449	conglomerate				
93	203341	9989024	1291	amphibolite	N90E		mine	
94	204107	9988413	1385	mica schist	104/30	194/30		
95	204221	9987858	1391	schist				
96	204730	9987205	1377	schist				
97	205138	9986922	1422	schst				vein
98	205410	9986708	1444	schist				
99	205464	9985965	1439	schist_conglomerate				
100	205430	9985598	1406	schist				
101	205524	9985467	1413	quarzite				
102	205616	9985283	1425	quarzite				
103	205716	9984699	1417	quarzite_schist				
104	204583	9983009	1415	quarzite				
105	205063	9982762	1444	quarzite_schist				
106	205586	9981421	1482	quarzite_schist				
107	206392	9981116	1488	quarzite				
108	266737	9880846	1487	quarzite				
109	206727	9980393	1557	quarzite				
110	208064	9978961	1572	quarzite				
111	209563	9978285	1603	quarzite				
112	209120	9979652	1705	quarzite				
113	209686	9979575	1802	quarzite				
114	210011	9977230	1810	quarzite	020/40	110/40		
115	209404	9975487	1936	quarzite	008/50	98/40		
116	208576	9974669	1976	quarzite	088/20	178/20	mine	
117	209052	99773101	1860	quarzite				
118	208236	9971516	1765	schist			mine	
119	206717	9971748	1681	quarzite	020/35	290/35		
120	205839	9972855	1498	quarzite	010/40	100/40		

121	205335	9970873	1467	schist				
122	205391	9969870	1444	clay				
123	204908	9969678	1407	clay_quarzite_cement			mine_cement	
124	204848	9969677	1392	quarzite				
125	204528	9968734	1474	quarzite_mudstone				
126	204570	9967809	1495	conglomerate				
127	204359	9967757	1495	mudstone	N50E		mine	
128	204627	9967211	1514	quarzite			mine	
129	204893	9966970	1534	quarzite	N30W		mine	
130	204966	9966961	1538	quazite			mine	
131	204257	9967653	1501	quazrzite	N20W		mine	
132	202754	9967313	1528	slate	170/10	260/10		
133	202571	9966278	1517	schist?/			mine	
134	204168	9962951	1699	quarzite			mine	
135	204616	9961614	1734	schist				
136	206155	9958798	1736	schist				
137	205291	9957320	1843	schist				
138	203342	9955232	1928	schist				
139	201398	9954714	1945	schist				
140	201479	9952202	1785	quarzite				
141	179462	9960225	1400	schist				
142	179536	9959894	1490	schist_quarzite				
143	180965	9959756	1413	schist				
144	182472	9960197	1385	schist				
145	182614	9960354	1364	schist				

Appendix 2

Description and Radiometric signatures of the major lithological units of Buhweju

Units/Formations	Descriptions	Radiometric signature
Banyaruguru and other volcanic	Tuff and agglomerates with occasional lava. Compositionally mainly of micacoues materials	The unit has elevated Th and U concentration relative to K and clearly evident at each radioelement, ratio and composite images
Kaiso and Epi-Kaiso beds	Entirely composed of gravel, sand, silt and clay	It has the same signature with Tuffs but more depleted in K and enriched in Th. It is easily
Munyoni Quartzite	Quartzite with minor pelite dominantly psammitic	Almost seen at every radiometric composite images clearly with high K and hence appear reddish on ternary image.
Lubare Quartzite	Very prominent Long and narrow quartzite ridge mainly composed of quartz muscovite and disseminated	Radiometric signature showed enrichment in eTh as compared to others and cleary seen on the fused and sharpened ternary images with Landsat
Isingiro conglomerates	Lenses of conglomerates surrounding the Lubare quartzite. Compositionally pebbles and grains of quartz in a quartz muscovite matrix	Alternating eTh and K elevations were seen on ternary images underlying the lubare quartzite which is also influences by topography
Granite and gneiss	Mainly composed of quartz and feldspar with occasional muscovite and highly weathered	It is characterized by having higher concentration of eTh and eU appearing cyan on ternary images. The distinction between granite and gneiss by using their radiometric signature is difficult due to weathering but discriminated with the aid of field
Pelite and Pelitic schist	Compositionally rich in muscovite and biotite mica. quartz is also common	Pelites showed elevated K, eTh and eU due to its intimate mixing with quartzite. Hence appearing white on ternary and clearly seen on other composite images. Pelitic schist relatively showed
Ibanda Quartzite	Isolated quarzitic ridge	It has the same radiometric signature with Lubare quartzite showing elevated eTh

Appendix 3

Confusion matrix accuracy report

CLASSIFICATION ACCURACY ASSESSMENT REPORT

Image File : c:/birr/geol_traning.img
User Name : Engdawork
Date : Sat Feb 19 00:10:17 2011

ERROR MATRIX

Reference Data

Classified Data	Unclassifi	Pelite	Gravel, sa	Tuff
Unclassified	0	0	0	0
Pelite	0	5	0	0
Gravel, sand an	0	0	5	1
Tuff	0	0	0	5
Conglomerates a	0	0	0	0
Quartzite with	0	0	0	0
Lunare quartzit	0	1	0	0
Granite	0	0	0	0
Schist	0	0	0	0
Gneiss	0	0	0	0
Schist and amph	0	0	0	0
Mudstone and cl	0	0	0	0
Column Total	0	6	5	6

Reference Data

Classified Data	Conglomera	Quartzite	Lunare qua	Granite
Unclassified	0	0	0	0
Pelite	3	0	1	0
Gravel, sand an	0	0	1	0
Tuff	0	0	0	0
Conglomerates a	8	0	2	0
Quartzite with	0	0	0	0
Lunare quartzit	0	0	25	0
Granite	0	0	0	5
Schist	0	0	0	0
Gneiss	1	0	10	0
Schist and amph	1	0	3	1
Mudstone and cl	0	0	0	0
Column Total	13	0	42	6

Classified Data	Schist	Gneiss	Schist and	Mudstone a
		Reference Data		
Unclassified	0	0	0	0
Pelite	4	0	0	0
Gravel, sand an	0	0	0	0
Tuff	0	0	0	0
Conglomerates a	2	0	1	0
Quartzite with	1	0	0	0
Lunare quartzit	1	0	0	0
Granite	0	0	0	0
Schist	15	0	0	0
Gneiss	2	6	0	0
Schist and amph	13	1	5	0
Mudstone and cl	1	0	0	1
Column Total	39	7	6	1

----- End of Error Matrix -----

ACCURACY TOTALS

Class Name	Reference Totals	Classified Totals	Number Correct	Producers Accuracy	Users Accuracy
Unclassified	0	0	0	---	---
Pelite	6	13	5	83.33%	38.46%
Gravel, sand an	5	7	5	100.00%	71.43%
Tuff	6	5	5	83.33%	100.00%
Conglomerates a	13	13	8	61.54%	61.54%
Quartzite with	0	1	0	---	---
Lunare quartzit	42	28	25	59.52%	89.29%
Granite	6	5	5	83.33%	100.00%
Schist	39	15	15	38.46%	100.00%
Gneiss	7	28	6	85.71%	21.43%
Schist and amph	6	25	5	83.33%	20.00%
Mudstone and cl	1	2	1	100.00%	50.00%
Totals	131	142	80		

Overall Classification Accuracy = 56.34%

----- End of Accuracy Totals -----

KAPPA (K^) STATISTICS

Overall Kappa Statistics = 0.5030

Conditional Kappa for each Category.

Class Name	Kappa
Unclassified	0.0000
Pelite	0.3575
Gravel, sand and silt	0.7039
Tuff	1.0000
Conglomerates and grits	0.5766
Quartzite with dominantly psammitic	0.0000
Lunare quartzite	0.8479
Granite	1.0000
Schist	1.0000
Gneiss	0.1735
Schist and amphibolite	0.1647
Mudstone and clay	0.4965

----- End of Kappa Statistics -----